國立臺灣大學工學院化學工程學系

博士論文

Department of Chemical Engineering
College of Engineering

National Taiwan University

Doctoral Dissertation

# 濃乳液的機械特性及基於石墨烯的奈米通道中的異常滲吸動力學

# Mechanical Characteristics of Concentrated Emulsions and Abnormal Wicking Dynamics in Graphene-based Nanochannels

張心瑀

Hsin-Yu Chang

指導教授：諶玉真 博士

Advisor: Yu-Jane Sheng, Ph.D.

中華民國 113 年 9 月

September 2024

doi:10.6342/NTU202404382

# 致謝

時光飛逝，五年的研究生涯彷彿一瞬間。在這段時間裡，我從不會寫程式的菜鳥學妹，成長為一位資深學姊。儘管仍有許多需要加強的地方，但與碩一時相比，我的研究能力、待人處事以及抗壓能力都有顯著提升。首先，感謝我的指導教授，諶玉真老師和曹恆光老師。諶老師耐心教導，給予鼓勵和資源，讓我能自由探索研究方向；曹老師的聰明才智讓我大開眼界，他不遺餘力地指導我，帶領我撰寫論文，使我的邏輯思維大幅提升。

剛進實驗室時，我充滿緊張和不安，幸運的是，有許多學長姐幫助我，包括罡慶、宇庭、婉茹、延齡、祥詰、英碩、相程、品瑢、冠宇、斯瑋。他們耐心指導，幫我打下模擬研究的基礎，還教會我許多電腦技能。我也很感謝他們在忙碌的研究中，還能抽空陪我吃飯、玩樂。同時，我也要感謝我的同學們，昱浩、亭雅、昱銘、譽蓉、柏豪、汶真。我們經常一起討論研究、吃飯、聊天、出去玩，在研究中互相督促、一起努力。在這兩年裡，非常開心能和他們共同成長。

我的第一屆學弟妹們，昕緯、宜庭、明璋、悅綺、彥智、心柔，感謝他們讓我第一次當學姊，也願意讓我教導他們研究。雖然碩二時我忙於自己的研究，較少與他們同樂，但我很珍惜這段相處的時光。第二屆的學弟妹們，皓鈞、峻崴、文哲、書瑜、冠臨、千又、庭瑜，這時我已經懂得如何在研究和生活之間找到平衡，感謝他們在研究繁忙時，還被我逼著出去玩。

第三屆的學弟妹們，法樵、家瑜、筱喻、瑞民、淳筠、致融、雅雯、斯楷、習鈞，謝謝他們陪我玩遍各地，每週的夜市行、每月的出遊，他們總是義不容辭。特別感謝法樵，總是滿足我的無理要求，從未發過脾氣，真的好喜歡他。第四屆的學弟妹們，詩晏、佳燁、宇翔、欣蓓、宜諍，是我維持學姊威嚴最短的一屆，很感謝他們常盡興陪我聊天、喝酒，真遺憾沒能陪著他們畢業。

這五年裡，雖然研究有辛苦，但快樂的時光更多。我很幸運遇見這麼多人，與大家一起旅遊、烤肉、慶祝生日...，這些都將成為美好的回憶。

doi:10.6342/NTU202404382

# 中文摘要

本論文分為四個部分。第一部分探討了液滴大小如何影響壓縮乳液的填充微結構和熱性質。在準備熱力學亞穩乳液時，液滴聚合是一個常見現象，使得研究單分散壓縮乳液在實驗或模擬中變得困難。在固定體積分數下，乳液的性質隨著液滴大小而變化，但相關研究有限。本研究使用耗散粒子動力學在無需事先了解微結構或液滴間的相互作用下，探索高濃度單分散液滴乳液的特性。研究結果顯示，形成堵塞結構的臨界體積分率約為 0.65。隨著體積分率的增加，平均配位數也增加，可以用一個簡單的尺度關係式描述。另外，我們亦系統性地研究體積分率、液滴直徑和界面張力對內能和熱容的影響。發現隨著體積分率和界面張力的增加，以及液滴直徑的減小，內能和熱容都會增長。尺度分析表明，模擬結果十分符合我們推導的尺度關係式的預測。

第二部分研究了含有奈米尺寸液滴的濃縮乳液之固態彈性行為，包括楊氏模數和體積模數。由於其固態般的行為，高體積分率的濃縮乳液在食品、化妝品、塗料和製藥等各個行業中有著廣泛的應用。然而，由於液滴的聚合和熱力學不穩定性，研究單分散濃縮乳液的機械性質是具有挑戰性的。我們採用一種介觀模擬方法來探索這些性質，並且無需事先得知乳液的微結構。我們研究了體積分率($\phi$)、液滴直徑(D)和界面張力($\sigma$)對楊氏模數(E)和體積模數(K)的影響。當$\phi < \phi_c$，楊氏模數不存在，而體積模數隨著$\phi$的增加而增加。當$\phi > \phi_c$，隨著$\phi$和$\sigma$的增加，兩者都會增加，特別是當液滴直徑減小時會更為明顯。我們的模擬結果顯示楊氏模數(E)和體積模數(K)能以兩式 $E \sim \phi^{0.13}(\phi-\phi_c)^{1.55}(\sigma/D)$ 和 $K \sim \phi^{1.06}(\phi-\phi_c)^{0.15}(\sigma/D)$表示。此外，對於軟材料，彈性模數和體積模數的關係滿足 $E=3K(1-2\nu)$，其中泊松比($\nu$)非常接近 0.5，但隨著$\phi$的增加仍然略有下降。

第三部分探討了在石墨烯奈米通道中全潤濕的乙醇之異常滲吸動力學。研究利用分子動力學探索了乙醇（全潤濕）在石墨烯片上的散擴行為，以及在石墨烯奈

doi:10.6342/NTU202404382

米通道中的滲吸過程。在散擴動力學中，存在兩個區段：初始由慣性主導的散擴和之後的黏性散擴，其指數高於坦納定律。全潤濕液體在滲吸動力學中表現出與部分潤濕液體不同的行為。前驅膜和主流隨著它們的長度與時間的平方根成比例地前進，前驅膜的比例常數與通道寬度無關，但主流的比例常數隨著通道變寬而減小。另外，前者的比例常數值較主流的值大。前驅膜的厚度和小於通道寬度的弧面曲率直徑都隨著通道變寬而增加。在非常狹窄的奈米通道中，前驅膜會融入主流，呈現出異常快速的滲吸行為。

第四部分研究了石墨烯奈米通道中通過前驅膜增厚來增強毛細流。由於前驅膜的存在，全潤濕液體在奈米毛細管中表現出與部分潤濕液體不同的滲吸動力學。我們使用分子動力學研究了在石墨烯片上全潤濕液體（異丙醇和二甲基甲酰胺）的潤濕行為以及在石墨烯的奈米通道中的滲吸動力學。自發散擴動力學遵循兩個冪律，其長期行為符合坦納定律。奈米通道中的滲吸偏離了沃什伯恩方程式，呈現出一個獨特的雙階段模式，其轉折點與液體類型相關但與通道寬度無關。在第一階段時，前驅膜的前進速率不隨通道寬度改變而變化。在前驅膜達到通道末端後，第二階段即開始，前驅膜重新變厚。此增厚程序，減少了膜的弧面曲率，因此增加毛細驅動力，加速了第二階段的毛細流，所以第二階段的滲吸速率明顯超過第一階段。

**關鍵字**：單分散濃縮乳液； 尺寸依賴性； 熱性能和機械性能； 奈米毛細管流；石墨烯奈米通道； 完全潤濕； 前驅薄膜。

# Abstract

This thesis comprises four parts. The first part explores the effect of droplet size on the packing microstructures and thermal properties of compressed emulsions. In preparing thermodynamically metastable emulsions, droplet coalescence is a common issue, making it challenging to study monodisperse compressed emulsions either experimentally or through simulations. Properties of emulsions vary with droplet size at a specified volume fraction, but relevant studies are limited. Here, dissipative particle dynamics simulations are used to explore highly concentrated emulsions of monodisperse droplets without prior knowledge of microstructure or inter-droplet interactions. The critical packing leading to the onset of the jammed structure is identified at a volume fraction around 0.65. The mean coordination number rises with increasing volume fraction and can be described by a scaling relation. The effects of volume fraction, droplet diameter, and interfacial tension on internal energy and heat capacity are systematically studied, showing growth with increased volume fraction and interfacial tension, and decreased droplet diameter. Dimensional analysis shows that all data points can be well represented by the scaling relations derived in this study.

The second part studies the solid-like elastic behavior, including Young's and bulk moduli, of nanosized concentrated emulsions. Concentrated emulsions with high volume fractions find applications in various industries like food, cosmetics, coatings, and pharmaceuticals due to their solid-like behavior. However, studying the mechanical properties of monodisperse concentrated emulsions is challenging due to droplet coalescence and thermodynamic instability. A mesoscopic simulation method is used to explore these properties without prior microstructure knowledge. The effects of volume fraction ($\phi$),

droplet diameter (D), and interfacial tension ($\sigma$) on Young's modulus (E) and bulk modulus (K) are investigated. Young's modulus is absent for $\phi < \phi_c$, while the bulk modulus increases with $\phi$. For $\phi > \phi_c$, both moduli grow with $\phi$ and $\sigma$, especially as D decreases. Our simulation results are represented by $E \sim \phi^{0.13}(\phi - \phi_c)^{1.55}(\sigma/D)$ and $K \sim \phi^{1.06}(\phi - \phi_c)^{0.15}(\sigma/D)$. Furthermore, the relationship for soft materials $E=3K(1-2\nu)$ is satisfied. The Poisson's ratio ($\nu$) is very close to 0.5 but still decreases slightly with increasing $\phi$.

The third part investigates the abnormal wicking dynamics of total wetting ethanol in graphene nanochannels. The study explores ethanol's (total wetting) spreading behavior on graphene sheets and the imbibition process in graphene nanochannels using Molecular Dynamics. In spreading dynamics, two regimes are identified: initial spreading dominated by inertia and viscous spreading with an exponent higher than Tanner's law. Total wetting liquid exhibits distinct behavior from partial wetting liquid in imbibition dynamics. The precursor film and main flow advance with their lengths proportional to the square root of time, but the constant for the precursor film, independent of channel widths, is greater than that of the main flow, which decreases with wider channels. Both the precursor film thickness and meniscus curvature diameter, smaller than the channel width, increase with wider channels. Very narrow nanoslits show surprisingly rapid imbibition behavior, with the precursor film blending into the main flow.

The fourth part examines the enhancement of capillary flow via precursor film thickening in graphene nanochannels. Total wetting liquids exhibit different wicking dynamics in nanocapillaries compared to partial wetting liquids due to the precursor film. We investigate total wetting liquids (isopropyl alcohol and dimethylformamide) on graphene sheets and imbibition dynamics in graphene-based nanoslits using molecular dynamics.

Spontaneous spreading dynamics follow two power laws, with long-term behavior conforming to Tanner’s law. Imbibition in nanoslits deviates from Washburn’s equation, showing a unique two-stage pattern with a turning point related to the liquid type, independent of channel width. The imbibition rate in the second stage exceeds the first. The precursor film's advancing rate remains constant irrespective of the channel width in the first stage. After the precursor film reaches the channel's end, the second stage begins, and the film re-thickens, reducing meniscus curvature and enhancing capillary flow.

**Keywords:** monodisperse concentrated emulsion; size-dependence; thermal and mechanical properties; nanocapillary flow; graphene nanochannels; total wetting; precursor film.

# Content

doi:10.6342/NTU202404382

doi:10.6342/NTU202404382

# Figure captions

doi:10.6342/NTU202404382

doi:10.6342/NTU202404382

doi:10.6342/NTU202404382

# Table captions

doi:10.6342/NTU202404382

# Chapter 1 Packing microstructures and thermal properties of compressed emulsions: effect of droplet size

## Abstract

In preparing thermodynamically metastable emulsions, the droplets tend to coalesce. Consequently, it is difficult to investigate the properties of a monodisperse compressed emulsion experimentally or by simulations. At a specified volume fraction, the properties of emulsions vary with the droplet size but the relevant studies are very limited. The dissipative particle dynamics simulations are adopted to explore the highly concentrated emulsion of monodisperse droplets. Prior knowledge of the microstructure and inter-droplet interaction is not required. The critical packing associated with the onset of the jammed structure can be identified from the growth of the projected area and perimeter of droplets with the volume fraction ($\phi$), $\phi_c \approx 0.65$. The mean coordination number ($\underline{Z}$) from the radial distribution function rises with increasing the volume fraction, and can be described by the scaling relation $(\underline{Z}-Z_c) \sim (\phi-\phi_c)^{0.82}$ with $Z_c \approx 6.3$. The effects of the volume fraction, droplet diameter (D), and interfacial tension ($\sigma$) on the internal energy ($\underline{U}$) and heat capacity ($\underline{C}_v$) are studied systematically. Both $\underline{U}$ and $\underline{C}_v$ are found to grow as $\phi$ and $\sigma$ are increased but D is decreased. According to dimensional analysis, all the data points can be well represented by the scaling relations $(\underline{C}_v-\underline{C}_{v,c}) \sim \phi(\phi-\phi_c)^{1/3}(\sigma/D)$ and $(\underline{U}-\underline{U}_c) \sim \phi(\phi-\phi_c)^{1/3}(\sigma/D)$.

**Keywords:** compressed emulsion; monodisperse emulsion; heat capacity; coordination number; scaling relations.

## 1-1 Introduction

An emulsion contains droplets of one liquid dispersed in a second immiscible liquid which is a continuous phase [1]. It is a metastable system and droplet coalescence is impeded by surfactant molecules located at the interface [2]. As the volume fraction of the dispersed phase exceeds about $\phi_c \approx 0.64$, the droplets become crowded and their shapes are deformed from sphere to polyhedron [3-5]. Nonetheless, the dispersed phase is still separated by thin films of the continuous phase. This concentrated system has a large volume of internal (dispersed) phase and is often referred to as high internal phase emulsion (HIPE) [6-9]. For example, the sunflower oil droplets with a 0.94 volume fraction can be stably dispersed in an aqueous solution containing xanthan gum and Tween 20 [10]. Although HIPE is comprised solely of fluids, its rheology is highly unusual and can exhibit elastic behavior at small deformation like solids because of the high degree of crowding. The structural disorder of the droplets is reminiscent of a glass state [1, 11].

HIPE is also called the highly concentrated or compressed emulsion and has the characteristics of kinetic stability and mechanical strength [12, 13]. The applications of concentrated emulsions include foods, cosmetics, coatings, paints, and pharmaceuticals [14-17]. It can be considered as the solid-like colloidal suspension with the isotropic disordered nonergodic state. The characteristic length of the highly concentrated emulsion is the order of the inter-droplet distance beyond which the static inhomogeneity vanishes. Different from the network gel structure, the elasticity of the concentrated emulsion is originated from the caging (jamming) effect [12]. That is, the constituent droplets of the emulsion are in close contact with each other and the entire system experiences a dynamic arrest. The jamming transition emerging beyond the critical concentration of random close packing can be viewed as a phase transition [18].

The detailed structure of a compressed emulsion is difficult to analyze directly in experiments. Recently, the raw image of a plane in the bulk of polydisperse emulsions was acquired by laser-scanning confocal microscopy with the fluorescent dye. The droplet positions of the marginally jammed system were then reconstructed three-dimensionally by the sphere-matching method. Consequently, the structural characterization of jammed packings can be obtained, including the mean number of neighbors and the radial distribution function g(r) [19].

The physical properties of concentrated emulsions vary significantly with the volume fraction ($\phi$) of the dispersed phase. In addition, it is found that the properties such as heat capacity ($C_p$) and viscosity depend on the size of the droplets (D) significantly in experiments [20-22]. Although the thermophysical property of emulsions was seldom studied, the heat capacity of the concentrated castor oil-in-water emulsions was investigated by differential scanning calorimetry measurement at different emulsification times [23, 24]. It is found that the specific heat capacity varies with the surface-to-volume ratio which increases with the emulsification time. In other words, the specific heat capacity grows with the increment of the interfacial area, corresponding to the reduction of droplet sizes at a given $\phi$ [20].

Highly concentrated emulsions are metastable systems but the spontaneous coalescence between droplets can be impeded by the surfactant layers at the liquid-liquid interfaces. In experimental studies, it is a challenge to acquire concentrated emulsions with a uniform size of droplets. Because of the limitation of preparation techniques and droplet coalescence, the droplet size distribution of the emulsion is generally very broad. As result, the dependence of the emulsion properties on the droplet size is difficult to be accurately investigated from experiments. In contrast, in molecular simulation studies, the droplet size can be easily controlled and thus systematic studies of the influences of droplet size

doi:10.6342/NTU202404382

and volume fraction may be achieved. However, in previous simulation studies, the coalescence between droplets is difficult to prevent and the size of the simulated system limits the number of droplets, leading to the inaccuracy of simulation results.

Until now, there are few simulation studies on highly concentrated emulsions. Typically, droplets in emulsions were modeled as assemblies of particles interacting via harmonic pair-potentials to form spring networks [1, 25, 26]. Because of the limitation of accurate knowledge of microstructures of concentrated emulsions, simple simplifications such as the local coordination number and minimum separation distance are often made [27]. Recently, the microstructure of marginally jammed polydisperse packings has been modeled and agrees excellently with 3D micrographs from experiments on jammed emulsion droplets [19]. In this work, prior knowledge of the microstructure and inter-droplet interaction is not required, and the highly concentrated emulsion of monodisperse droplets, whose coalescences are prevented, will be developed in dissipative particle dynamics (DPD) simulations. At a specified volume fraction ($\phi > \phi_c$), the structure evolves toward quasi-equilibrium and the deformed droplets are randomly dispersed in the continuous solvent without controlling the coordination number and minimum separation distance. At quasi-equilibrium, the packing microstructure and thermodynamic properties can be examined. The influences of the volume fraction, droplet size, and interfacial tension are then explored systematically.

## 1-2 Method

DPD simulation which is similar to molecular dynamics (MD) is a coarse-grained approach and can overcome the time and space scale limitation in MD [28-32]. A DPD bead with mass *m* comprises a few atoms or molecules and its motion obeys Newton's equation of motion [33]. The interactions between DPD beads are soft and repulsive and generally contain three types of pairwise-additive and short-ranged forces: conservative force ($\boldsymbol{F}_{ij}^{C}$), random force, and dissipative force [34, 35]. The equilibrium state is controlled by the conservative force, $\boldsymbol{F}_{ij}^{C} = a_{ij}(1 - r_{ij} / r_c)\hat{\boldsymbol{r}}_{ij}$, which vanishes as $r_{ij} > r_c$. $a_{ij}$ is the interaction parameter which determines the maximum repulsion. Here $r_{ij}$ represents the distance between the beads $i$ and $j$, $\hat{\boldsymbol{r}}_{ij}$ the unit vector along the line joining them, $r_c$ the interaction range. The random force is adopted to control the system temperature T and related to the dissipative force so that the fluctuation-dissipation relation is satisfied [28, 30, 36, 37]. In our simulations, all the mass, length, and energy are nondimensionalized by $m$, $r_c$, and $k_BT$, where $k_B$ denotes the Boltzmann constant.

In this work, the emulsion system contains droplets of the same size dispersed in the continuous phase. Without loss of generality, monodisperse oil droplets are randomly distributed in the water phase initially. For the same types of beads, the interaction parameter $a_{ii}$ is chosen as 25, for example, $a_{oo} = a_{ww} = 25$ for both oil (o) and water (w) phases. For different types of beads, $a_{ij}$ deviates positively from 25 as the incompatibility increases. The interaction parameter between the oil and water phases affects their interfacial tension (σ) and is assumed as $a_{ow}$ = 50~80. For example, as $a_{ow}$=50, σ=2.02 and $a_{ow}$=70, σ=3.20. The thermodynamic instability of emulsions (coalescence of droplets) is generally hindered by the addition of surfactant. However, in this study, the emulsion stability is ensured by introducing a very strong repulsion (e.g., $a_{oo}^{*} = 3000$) between two touching oil droplets. This assumption is very similar to the strong repulsion between the surfactant layers adsorbed on the two droplets nearly in contact. Note that the simulation result is not sensitive to the value of $a_{oo}^{*}$ as long as the coalescence can be prevented even in the compressed emulsion. As a result, the deformable droplets remain monodisperse throughout the simulations and all of them contain the same number of DPD beads.

The emulsion was simulated in a cubic box with V = $(32.2)^3$ under periodic boundary

doi:10.6342/NTU202404382

conditions subject to the NVT ensemble (constant bead number, simulation box volume, and temperature). The number densities of both dispersed and continuous phases were approximately $\rho \approx 3$ and the total number of DPD beads was $N = 100000$ [30]. The equation of motion was integrated by the velocity Verlet scheme, and the time increment was set as $\Delta t = 0.01$. The system temperature was always maintained at unity. It took about $3 \times 10^6$ steps for the jammed system to reach the quasi-equilibrium state. The volume fraction ($\phi$) of the dispersed (oil) phase was defined as the ratio of the total beads in the dispersed phase to those in the system, and it ranged from $\phi = 0.1$ to $0.95$. The typical snapshots of the emulsion systems were given in Figure 1-1 for various volume fractions. The structural characteristics (e.g., the radial distribution function) and thermodynamic properties (e.g., heat capacity) were calculated for quasi-equilibrium emulsions with different volume fractions ($\phi$), interfacial tensions ($\sigma$), and droplet sizes (D).

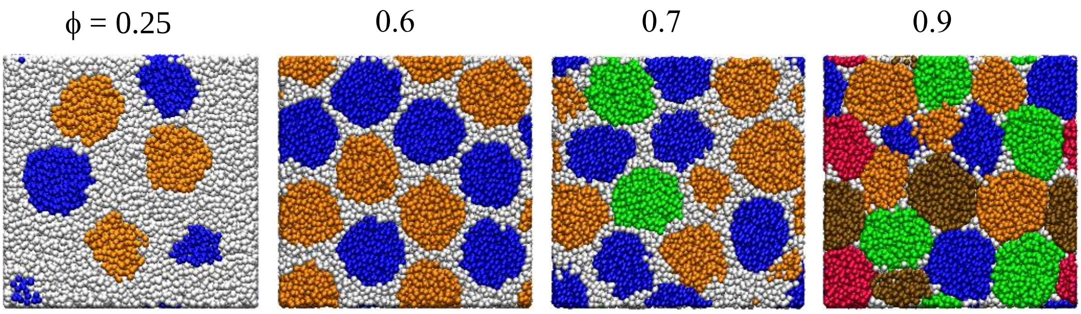

Figure 1-1. Snapshots of emulsions at different volume fractions $\phi$ = 0.25 - 0.9. The droplets are colored, while the continuous phase is represented by white beads.

The average diameter of the droplet (D) was determined from a few images in the dilute limit where the droplets are nearly spherical, and it was slightly greater than $[n_o/(\rho\times\pi/6)]^{1/3}$, where $n_o$ denotes the number of DPD beads in a droplet. Note that the droplet size (D) can be adjusted by varying $n_o$. For example, as $n_o = 600$ , $D = 7.57$ and $n_o = 1000$ , $D = 9.27$. The average project perimeter (P) and area (A) of the deformed droplet

doi:10.6342/NTU202404382

were estimated from a few snapshots over several projections. The structure of a compressed emulsion which is closely associated with the dispersed phase is often realized by the radial distribution function g(r), which described how the droplet density varies as a function of the distance from one particular droplet [38, 39]. The radial distribution function of monodisperse droplets is defined as

$$\mathrm{g(r)} = \left(\frac{\mathrm{dn(r)}}{4\pi((\mathrm{r}+\mathrm{dr})^2 - \mathrm{r}^2)}\right) / \ \rho_d, \tag{1}$$

where dn(r) represents the number of droplets whose centers of mass are located at a distance between r and $\mathrm{r} + \mathrm{dr}$ from the center of the specified droplet and $\rho_d$ denotes the bulk droplet density which varies with the volume fraction (ϕ) and droplet size (D). The mean coordination number ($\underline{Z}$) depicts the average value of the number of the nearest neighboring droplets and it is linked to g(r) directly.

## 1-3 Results and discussion

The compressed emulsion in which the volume fraction of the dispersed phase exceeds the critical value ($\phi_c$ = 0.60 ~ 0.65) is investigated. In our simulations, the emulsion is always monodisperse and stable because the coalescence between any pair of droplets is completely prevented. The function of the emulsifier which is required to obtain metastable emulsions is simply replaced by the strong short-ranged repulsion between two droplets. Phase inversion which occurs in microemulsions will not take place by adjusting the oil-water ratio. After reaching equilibrium, the microstructure of the jammed system can be analyzed thoroughly and the internal energies can be calculated in details, including those of dispersed phase, continuous phase, and interphase. In this study, both phases are formed by simple liquids such as water and alkane. However, the general influences of the volume fraction, interfacial tension, and droplet size on the behavior of the compressed emulsions are demonstrated and not limited to specific emulsions indicated by the earlier reports [40-42].

### 1-3-1 Structure of compressed emulsions

Although the droplet shape fluctuates persistently and the random motion is frequent in the continuous phase, the packing structure of the emulsion can be analyzed statistically. The representative shapes of the droplets which are in the quasi-equilibrium state are demonstrated in Figure 1-2(a) for $\phi = 0.85$, $D = 18.1$, and $\sigma = 3.20$.

The perimeter and area of the chosen droplets at different times are determined. Note that the perimeter (P) and area (A) are dimensionalized by those of the spherical droplet in the dilute limit (e.g., $\phi = 0.1$). As the volume fraction is high, the droplet shape deviates from the sphere evidently and both P and A exceed unity. Some images look like a hexagonal structure. Because of jamming, the mean perimeter and area of a droplet are expected to vary with the volume fraction. Figure 1-2(b) shows the variations of P and A with $\phi$ from 0.1 to 0.95 and the turning points corresponding to the onset of jamming are found to appear at $\phi = \phi_c \approx 0.65$. The perimeter and area were averaged over 100 samples acquired every 1000 time steps. As $\phi < \phi_c$, the slow increment of P and A is accompanied by the shape deformation caused by more collisions between droplets at higher $\phi$. The shape deformation grows more significantly with increasing $\phi > \phi_c$, leading to the rapid rise of P and A.

doi:10.6342/NTU202404382

(a) Typical projected shapes of the droplet

| **Perimeter(P)** | **1.04** | **1.04** | **1.03** | **1.02** |
|---|---|---|---|---|
| Area (A) | 1.07 | 1.06 | 1.06 | 1.07 |
| Snapshot | 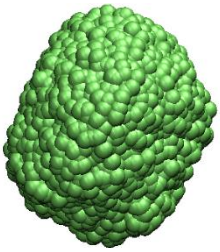<br>(t = 30000) | 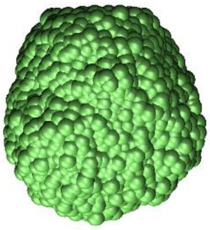<br>(t = 28000) | 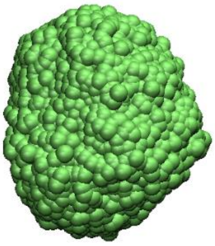<br>(t = 25000) | 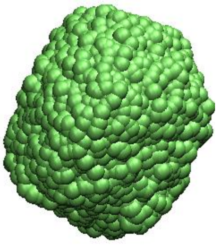<br>(t = 24000) |

(b) Effect of the volume fraction

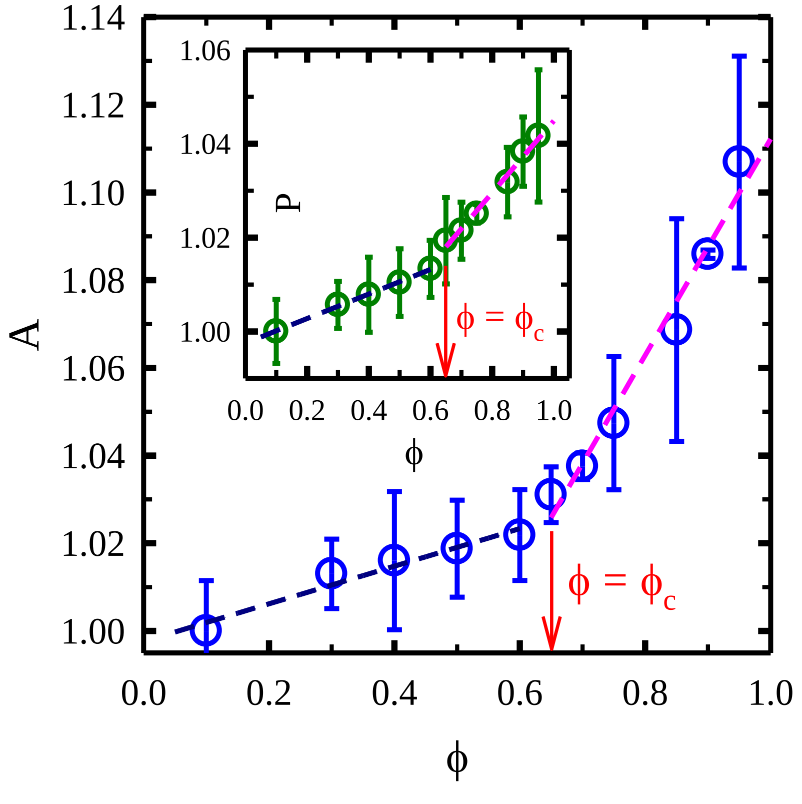

Figure 1-2. (a) The dimensionless projected perimeter (P) and area (A) associated with the typical droplet shown in the snapshots for ϕ = 0.85, D = 18.1, and σ = 3.20. P and A

are scaled by those of droplets in the dilute limit. (b) The variation of the mean perimeter and area with the volume fraction. The turning point gives the critical volume fraction $\phi_c \approx 0.65$.

The microstructure of the compressed emulsion can be realized by the radial distribution function g(r), which depicts the probability of finding a droplet from the reference droplet over various displacements. The typical g(r) of $\phi = 0.8$ for $D = 7.57$ and $\sigma = 3.20$ is illustrated in the inset of Figure 1-3. The first peak is located at $r = 6.75$, which is less than $D = 7.57$, indicating that droplets are crowded and deformed significantly. Because of the deformable nature of the droplet and nearly incompressible condition, g(r) drops to zero between the first and second peaks. The influence of the volume fraction $\phi$ on the position of the first peak is shown in Figure 1-3. As $\phi$ is decreased, the position of the first peak is generally increased and close to the droplet diameter D. This consequence can be understood from the fact that lower volume fractions yield less jammed configurations.

doi:10.6342/NTU202404382

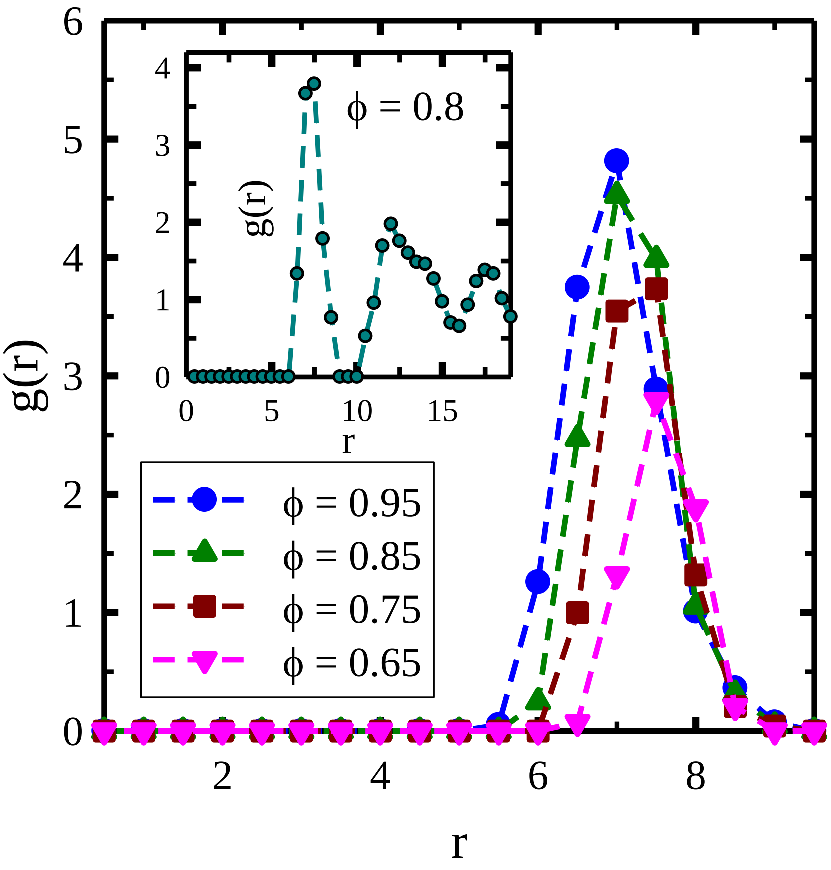

Figure 1-3. The short-range radial distribution function g(r) for the monodisperse compressed emulsions with D = 7.57 and σ = 3.20 at volume fractions from 0.65 to 0.95. In the inset, the typical radial distribution function g(r) for ϕ = 0.8 is demonstrated.

The distribution of the distance between the centers of two neighboring droplets is closely related to the first peak of g(r). Note that two neighboring soft droplets do not necessarily contact each other in the compressed emulsion. A representative cross-section picture is demonstrated in Figure 1-4, and it shows that the centered droplet is either in direct contact with the nearby droplet or separated from the neighboring droplet by a thin water layer. The mean distance $r_m$ and standard deviation (SD) are expected to vary with the volume fraction. As anticipated, Figure 1-4 with D = 7.57 shows that the mean dis-

doi:10.6342/NTU202404382

tance declines with increasing ϕ. However, the standard deviation of the distance distribution is found to grow with increasing ϕ, as depicted in the inset. This result reveals that the greater shape deformation associated with larger ϕ leads to the wider distribution of the distance between neighboring droplets. Since the standard deviation is much smaller than the droplet size, the nearly incompressible condition is still fulfilled.

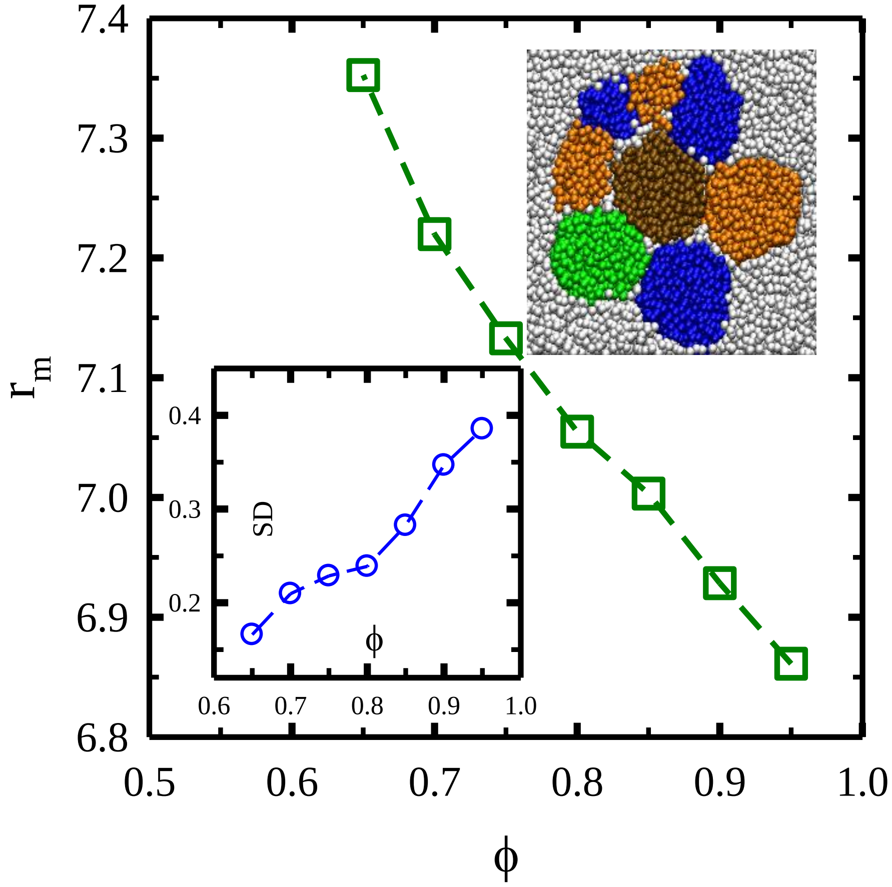

Figure 1-4. The mean distance between two neighboring droplets ($r_m$) is plotted against the volume fraction at D = 7.57 and σ = 3.2. The lower inset shows the standard deviation (SD) of the distribution of the interdroplet distance. In the upper inset, the snapshot illustrates the neighboring droplets surrounding the central droplet.

The feature of the first shell around a center droplet can be described by the coordination number, which varies with the position and depends on the volume fraction as well.

Figure 1-5(a) demonstrates the probability distribution of the coordination number (Z) for different values of $\phi$ with D = 7.57. As $\phi$ is increased, the distribution shifts to the large Z and becomes narrower. The largest coordination number can reach 18 at $\phi = 0.95$. As shown in Figure 1-5(b), the mean coordination number ($\underline{Z}$) grows with increasing $\phi$ and the turning point can be identified at $\phi_c = 0.65$, corresponding to the onset of droplet jamming. For $\phi > \phi_c$, the rapid rise of $\underline{Z}$ is accompanied with serious shape deformation. The relation between the mean coordination number and volume fraction may be depicted by the power law $(\underline{Z} - Z_c) \sim (\phi - \phi_c)^{\alpha}$ [18, 27], where $Z_c$ is $\underline{Z}$ at $\phi = \phi_c$. The inset of Figure 1-5(b) shows a linear line with the slope $\alpha = 0.82$ in the logarithmic plot of $(\underline{Z} - Z_c)$ against $(\phi - \phi_c)$ for $\phi > \phi_c$, which is slightly greater than the value reported in literature 0.5 obtained soft sphere simulations based on the network spring model [27].

(a) Distribution of the coordination number

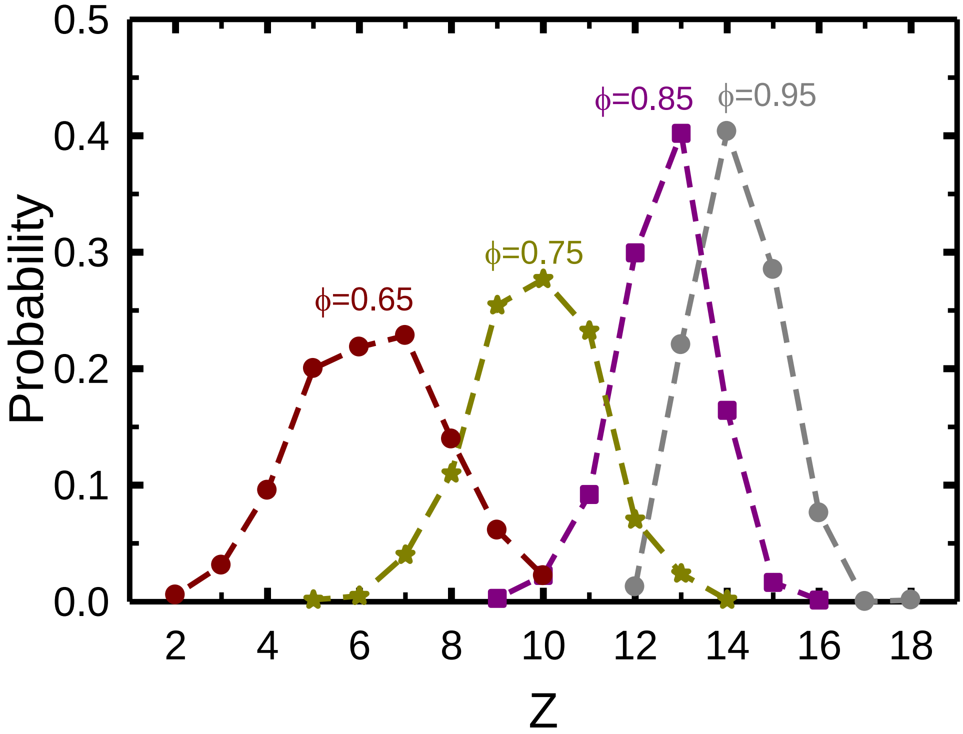

(b) Effect of the volume fraction

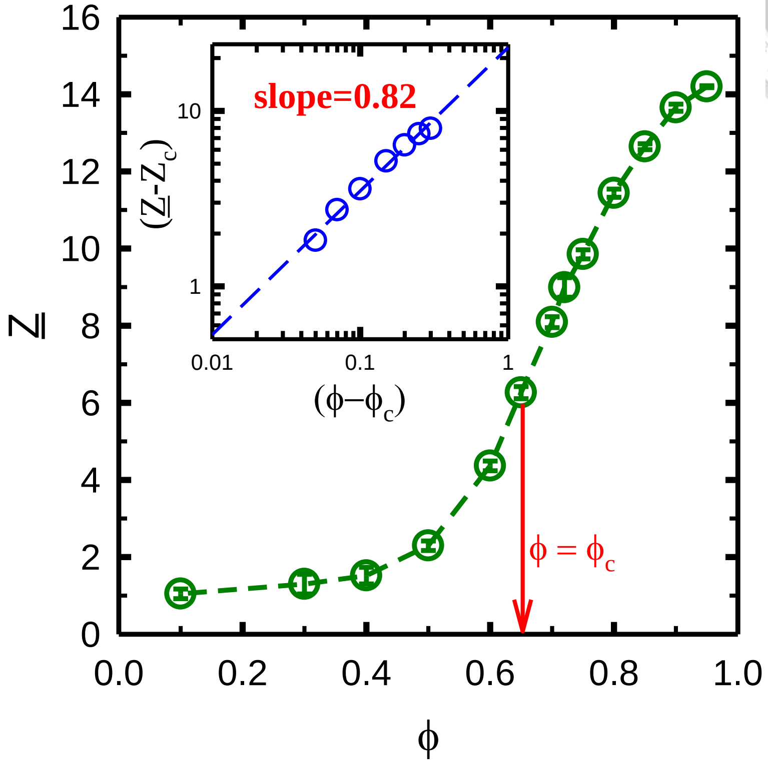

Figure 1-5. (a) The probability distribution of the coordination number (Z) with D = 7.57 and $\sigma$ = 3.20 for different values of $\phi$. The sum of the distribution equals unity. (b) The variation of the mean coordination number ($\underline{Z}$) with the volume fraction. In the inset, ($\underline{Z}$ - $Z_c$) is plotted logarithmically against ($\phi$ - $\phi_c$) and the data points can be represented by the linear line with the slope of 0.82.

### 1-3-2 Internal energy and heat capacity

In previous simulation studies [1, 27], the internal energy of the compressed emulsion which is a disordered droplet packing has been modeled as a system of soft spheres which interact with their nearest neighbors. The repulsive central-force potential such as harmonic-spring potential is frequently adopted to reflect the behavior of facets. As a result, the details of the shape response to deformation and the coupling between different facets on each droplet are ignored. Based on the average coordination number and a single effective potential, the internal energy of the system becomes tractable, as the forces acting on each droplet are balanced. In this work, however, the stable compressed emulsion is simulated without assuming the interdroplet interaction potential. As the droplets are compressed, the changes in interfacial energy are accounted for directly and the effects of the volume fraction, droplet size, and interfacial tension on the internal energy can be calculated.

The internal energy (U) of the emulsion is separated into three contributions: dispersed phase ($U_d$), continuous phase ($U_c$), and interface ($U_i$). The total energy of the system is $U = U_d+U_c+U_i$ where $U_i$ represents the sum of the pair potentials between oil and water beads at contacts. The internal energy per bead is denoted by $\underline{U}_k$ (k=c, d, or i) and $\underline{U}_i$ is $U_i$ divided by the number of beads in the dispersed phase which are in contact with the continuous phase. Figure 1-6 shows the variation of the internal energy with the volume fraction of the dispersed phase for the droplet diameter D = 9.27 and interfacial tension $\sigma = 3.20$. Evidently, near the critical volume fraction, $\underline{U}_c$ decreases fast while $\underline{U}_i$ ascends rapidly. Without loss of generality, the continuous phase is assumed as water and the dispersed phase is oil for simplicity. As $\phi - \phi_c$ is increased, the average number of oil beads in contact with each water bead rises, leading to the rapid growth of $\underline{U}_i$. In contrast, the number of water-water pairs per water bead decreases accordingly, resulting in the sharp decrement of $\underline{U}_c$. In addition to the changes of $\underline{U}_i$ and $\underline{U}_c$, $\underline{U}_d$ is also found to vary with $\phi$, as shown in the inset of Figure 1-6. For $\phi < \phi_c$, the linear increase of $\underline{U}_d$ with $\phi$ is associated with the growth of the osmotic pressure. For $\phi > \phi_c$, the increment of $\underline{U}_d$ is attributed to the internal pressure buildup due to the jamming structure. The turning point at $\phi = \phi_c$ reflects the two different mechanisms. Note that the contribution of direct contacts between two droplets to the total internal energy is negligible (about 0.08%).

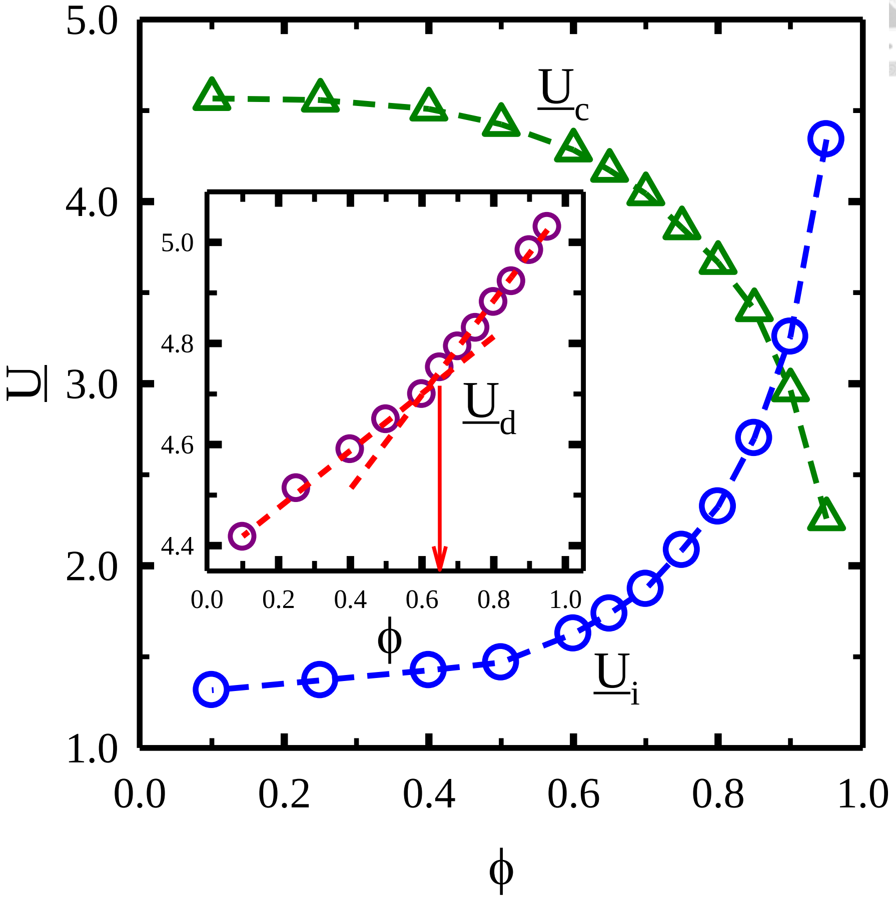

Figure 1-6. The variation of the internal energy associated with the continuous phase ($\underline{U}_c$) and interface ($\underline{U}_i$) with the volume fraction for D = 9.27 and $\sigma = 3.20$. In the inset, the internal energy of the dispersed phase ($\underline{U}_d$) is plotted against the volume fraction.

In addition to $\phi$, the internal energy per bead ($\underline{U}$) of the compressed emulsion depends on $\sigma$ and D as well. Figure 1-7(a) shows the variation of the internal energy contributions with the interfacial tension at the volume fraction $\phi = 0.8$ and droplet size D = 8.6. As $\sigma$ is increased, the water bead disfavors the oil bead more, facilitating the contacts between water beads. Therefore, $\underline{U}_i$ (interface) decreases but $\underline{U}_c$ (water phase) ascends. Besides, $\underline{U}_d$ (oil phase) is also found to grow with increasing $\sigma$. This result is accompanied by the increment of the pressure inside the droplet based on the Young-Laplace equation ($P_d = P_c + 4\sigma/D$). Figure 1-7(b) shows the variation of the internal energy contributions with the droplet diameter (D) at $\phi = 0.8$ and $\sigma = 3.20$. As D is decreased from 17.21 to 6.83, the interfacial area increases, and therefore $\underline{U}_i$ grows accordingly. It is somewhat surprising to find the increment of $\underline{U}_d$ and the slight decline of $\underline{U}_c$ with decreasing the droplet size. According to the Young-Laplace equation ($\Delta P = 4\sigma/D$), either $P_d$ (dispersed phase) ascends or $P_c$ (continuous phase) descends, as D is decreased [43-45]. The rise of $P_d$ results in the decrease of the mean distance between beads, leading to the growth of $\underline{U}_d$. In contrast, the fall of $P_c$ gives the decrease of $\underline{U}_c$.

(a) Effect of the interfacial tension

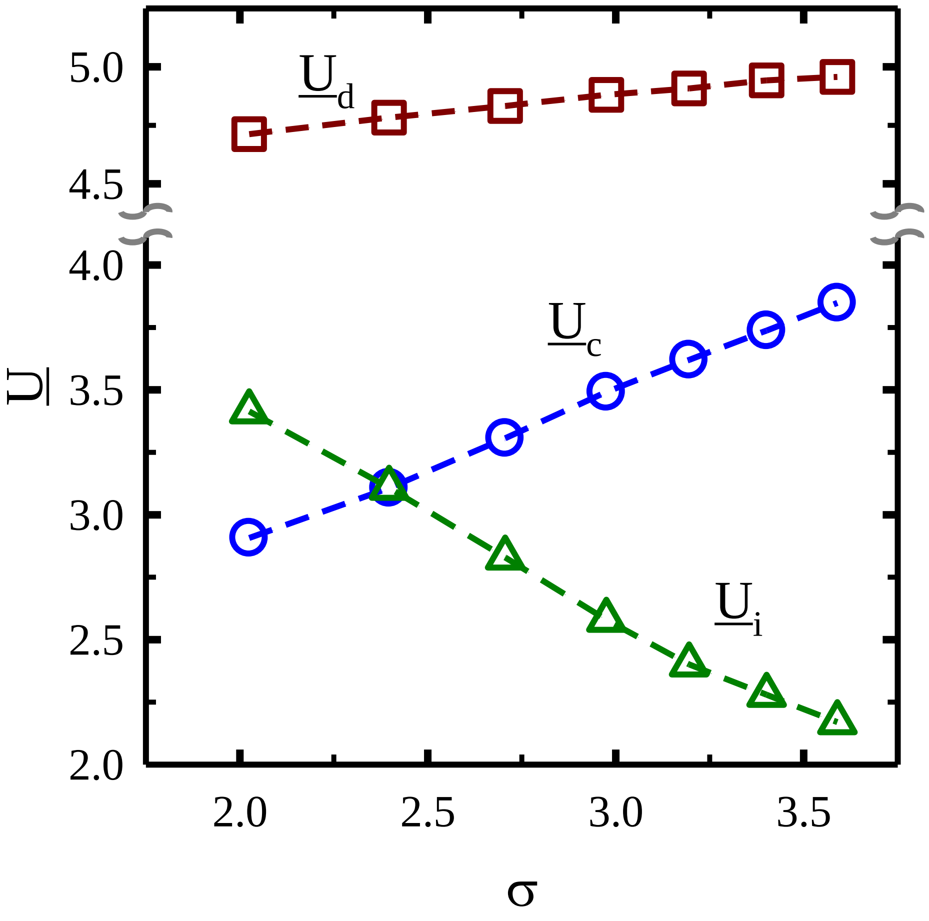

(b) Effect of the droplet size

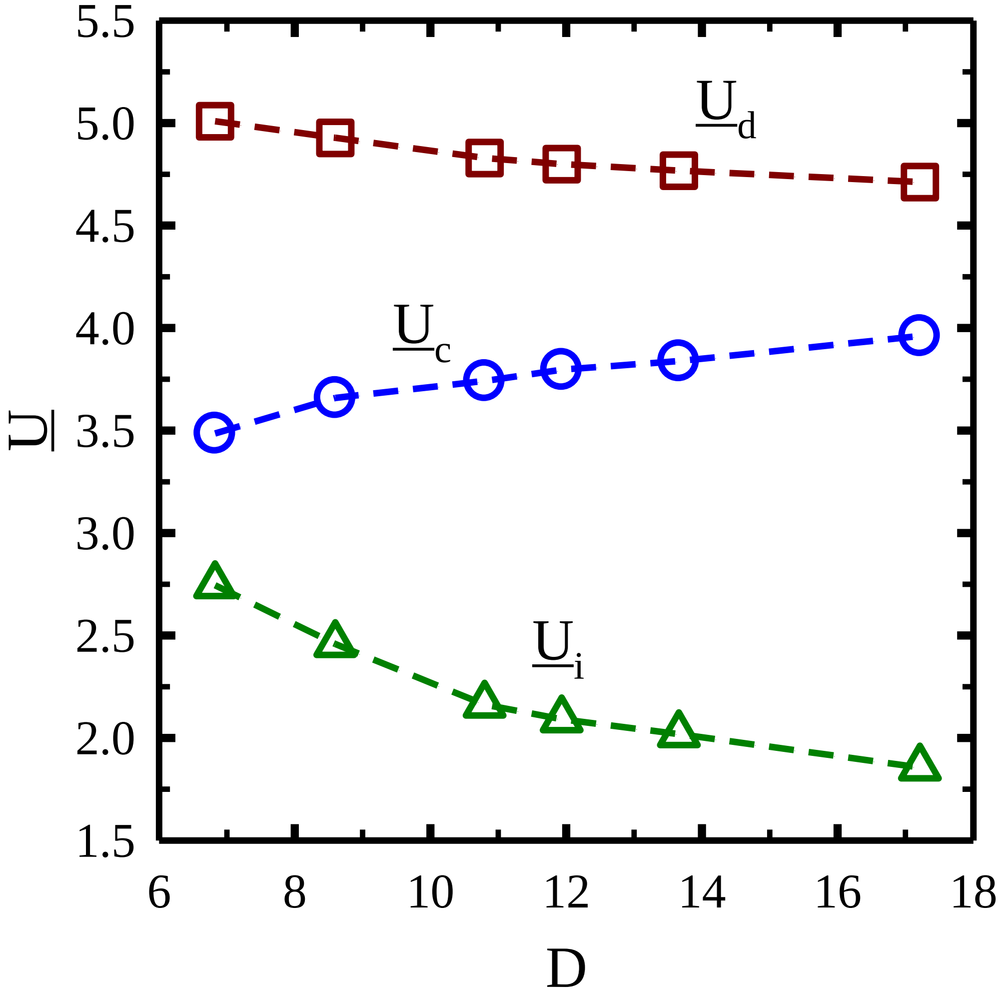

Figure 1-7. (a) The variation of the internal energy ($\underline{U}_c$, $\underline{U}_d$, and $\underline{U}_i$) with the interfacial tension for $\phi = 0.8$ and $D = 8.6$. (b) The variation of the internal energy with the droplet size for $\phi = 0.8$ and $\sigma = 3.20$.

The heat capacity $C_v$ is important for applications involving heating or cooling processes, and it describes the amount of thermal energy required to raise the temperature of the system by one degree. However, very few studies report the thermophysical property such as heat capacity of emulsions. By using a differential-scanning-calorimetry technique, the specific heat capacity of highly concentrated castor oil-in-water emulsions (more than 90% oil) was obtained [20]. It is found that at a given composition, the heat capacity grows with the emulsification time which affects the mean droplet size. Short emulsification times give more polydisperse emulsions with bigger droplets. That is, the heat capacity of emulsions varies with the emulsion morphology or mean droplet size [20]. This result is interesting because the thermophysical property of a mixture is generally expected to depend on the composition only. To eliminate the effect of polydispersity, concentrated emulsions of monodisperse droplets are considered to evaluate the internal energies and specific heat capacities in our simulations.

The specific heat capacity can be determined by the fluctuation of the internal energy [46],

$$\underline{C}_v = \left(\frac{\partial \underline{U}}{\partial T}\right)_V = \frac{\langle \underline{U}^2\rangle - \langle \underline{U}\rangle^2}{k_B T^2}. \tag{2}$$

$\underline{U}^2$ and $\underline{U}$ are recorded every 100 DPD steps during the simulation. According to the results of the internal energy, the heat capacity of the emulsion system has to vary with the droplet size (D) and interfacial tension ($\sigma$) as well, in addition to the composition ($\phi$). As demonstrated in the inset of Figure 1-8, $\underline{U}$ grows with increasing the volume fraction ($\phi$) for $D = 7.57$ and $\sigma = 3.20$. It seems that there exists a turning point at $\phi \approx 0.65$ although the difference between the slopes (0.72 and 0.82) is not significant. The transition from the free movement of droplets to the jammed structure is more eminent in the plot of the heat capacity against the volume fraction (Figure 1-8). The sharp change of $\underline{C}_v$ for $D = 7.57$ can be clearly seen in the regime $\phi = 0.6 \sim 0.7$, indicating the structural transition associated with the emergence of the jamming.

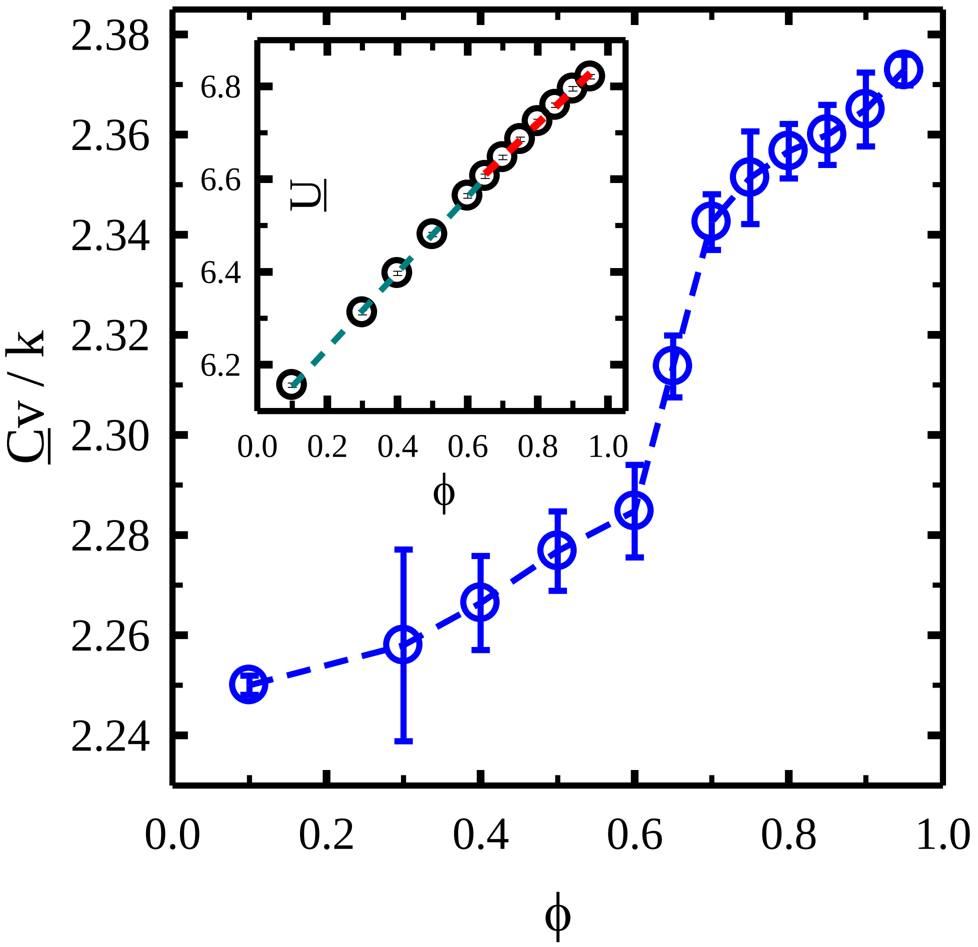

Figure 1-8. The heat capacity $\underline{C}_v$ is plotted against the volume fraction for D = 7.57 and σ = 3.20. The inset shows that the internal energy per bead ($\underline{U}$) is plotted against the volume fraction.

Because the internal energy is a function of $\underline{U}(\phi,\sigma,D)$, the heat capacity is also a function of $\underline{C}_v(\phi,\sigma,D)$. The variation of $\underline{C}_v$ with σ for ϕ = 0.8 and D = 8.6 is illustrated in the inset of Figure 1-9. Obviously, $\underline{C}_v$ grows linearly with σ although the interfacial interaction energy $\underline{U}_i$ decreases with increasing σ (see Figure 1-7(a)). In fact, $\underline{U}$ is also found to grow linearly with σ, indicating that $\underline{U}_c$ and $\underline{U}_d$ dominate the change of $\underline{U}$ with σ. The variation of $\underline{C}_v$ with 1/D for ϕ = 0.8 and σ = 3.20 is shown in Figure 1-9. Again, $\underline{C}_v$ grows linearly with 1/D, which is consistent with the decrement of $\underline{U}_i$ and $\underline{U}_d$ with D (see Figure

7(b)). Note that $\underline{U}$ grows linearly with 1/D, revealing that $\underline{U}_i$ and $\underline{U}_d$ dominate the change of $\underline{U}$ with D. Because the interfacial area increases and the buildup of the Laplace pressure with 1/D, $\underline{U}_i$, and $\underline{U}_d$ prevail over the linear change of $\underline{U}_c$ with 1/D. The results shown in Figure 1-9 for $\phi = 0.8$ demonstrate that $\underline{C}_v$ is proportional to both $\sigma$ and 1/D for $\phi \geq \phi_c$. Moreover, it is not surprising to observe that $\underline{U}$ is proportional to both $\sigma$ and 1/D for $\phi \geq \phi_c$ as well.

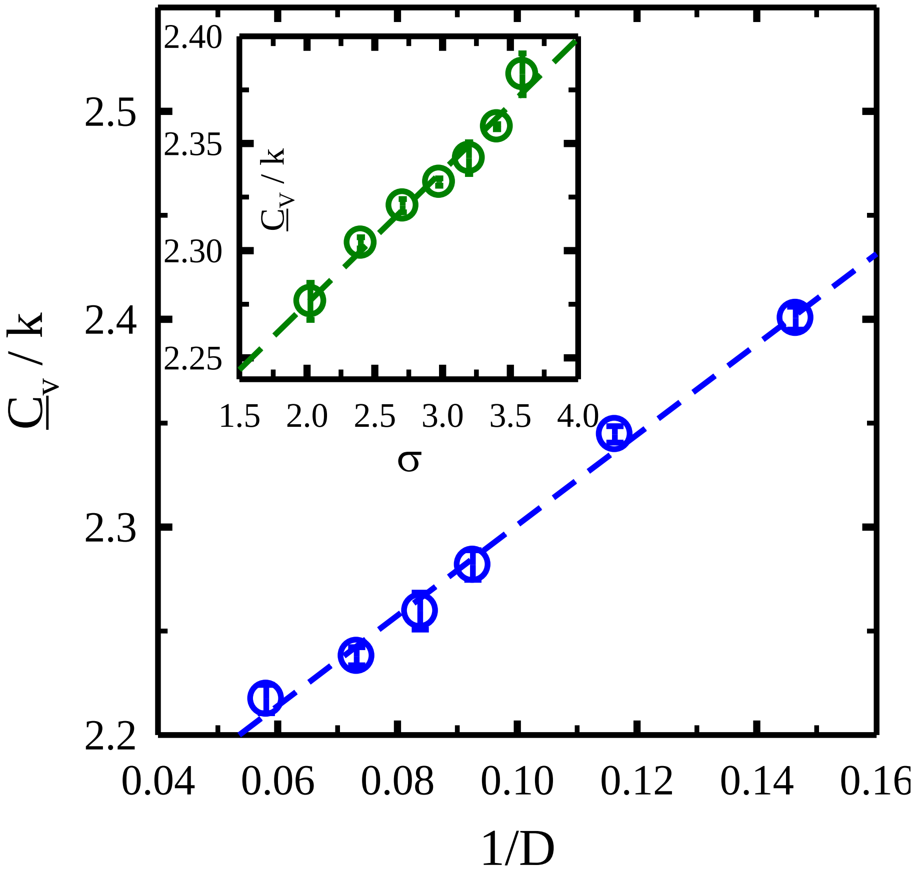

Figure 1-9. The heat capacity ($\underline{C}_v$) is plotted against the reciprocal of the droplet size (1/D) for $\phi = 0.8$ and $\sigma = 3.20$. The inset shows that the heat capacity ($\underline{C}_v$) is plotted against the interfacial tension for $\phi = 0.8$ and D = 8.6.

$\underline{U}$ and $\underline{C}_v$ are a function of $\phi$, $\sigma$, and D because of the existence of the interfaces in emulsions. The above findings and dimensional analysis reveal that $\rho\underline{C}_v$ and $\rho\underline{U}$ may be a linear function of $\sigma/D$, where the density is $\rho = 3$ in this work. Figure 1-10(a) shows the variation of $\underline{C}_v$ and $\underline{U}$ with $\sigma/D$ for different combinations of $\sigma$ and D at $\phi = 0.8$. All data points are collapsed reasonably into a single line, indicating the linear relationship between $\underline{C}_v$ (or $\underline{U}$) and $\sigma/D$. The dependence of the physical quantities on $\phi$ for compressed emulsions are often described by $\phi^{\alpha}(\phi\text{-}\phi_c)^{\beta}$ [1, 3, 47]. As a result, the contribution at $\phi = \phi_c$ must be eliminated and the relations between $\Delta\underline{U} = \underline{U}(\phi) - \underline{U}(\phi_c)$ or $\Delta\underline{C}_v = \underline{C}_v(\phi) - \underline{C}_v(\phi_c)$ and $\phi$ are considered. Figure 1-10(b) shows the plots of $\Delta\underline{C}_v/(\sigma/D)$ and $\Delta\underline{U}/(\sigma/D)$ against $\phi(\phi\text{-}\phi_c)^{1/3}$ for various combinations of $\phi$, $\sigma$, and D. Again, all data points are collapsed reasonably into a single line, revealing that $\Delta\underline{C}_v$ and $\Delta\underline{U}$ are linearly proportional to $\phi(\phi\text{-}\phi_c)^{1/3}(\sigma/D)$.

(a) Function of σ/D

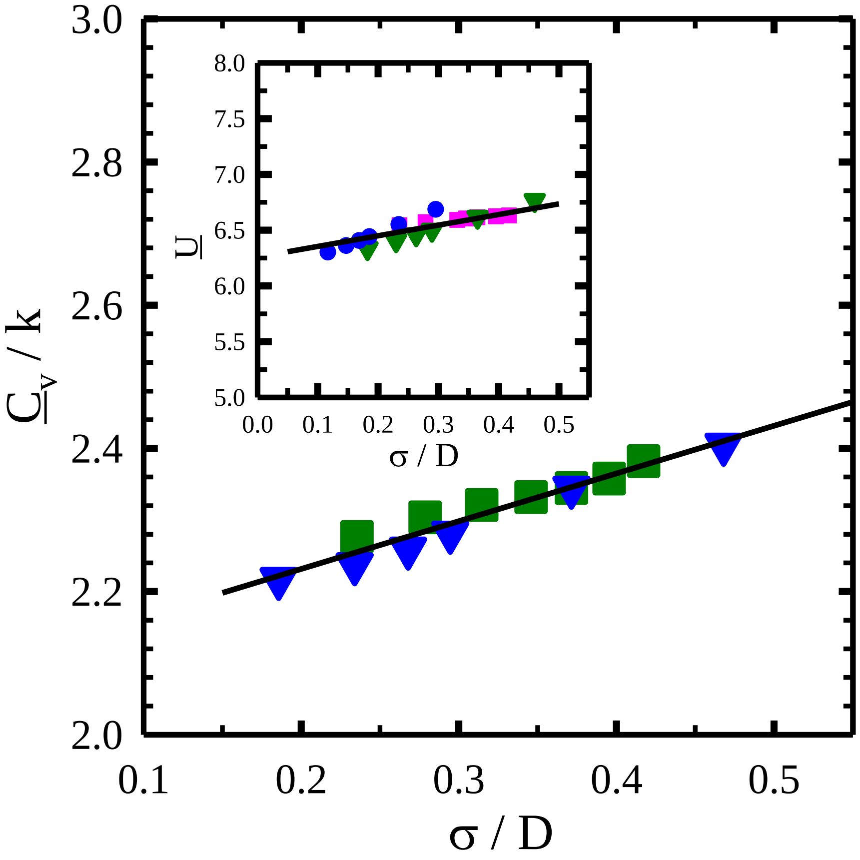

doi:10.6342/NTU202404382

(b) Function of ($\phi$ - $\phi_c$)

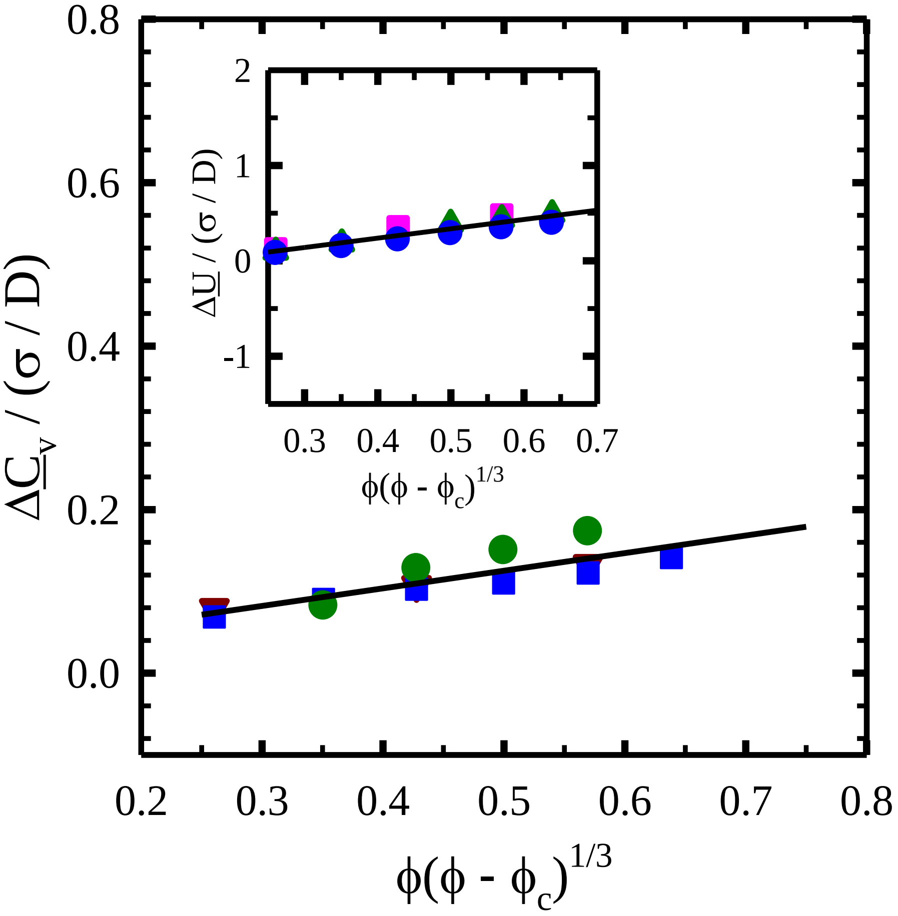

Figure 1-10. (a) The plots of $\underline{C}_v$ and $\underline{U}$ against $\sigma$/D for various combinations of $\sigma$ and D at $\phi$ = 0.8. (b) The plots of $\Delta\underline{C}_v/(\sigma/D)$ and $\Delta\underline{U}/(\sigma/D)$ against $\phi(\phi-\phi_c)^{1/3}$ for various combinations of $\phi$, $\sigma$, and D. All data points can collapse into a linear line reasonably.

## 1-4 Conclusion

The emulsion is thermodynamically metastable because the droplets stabilized by adsorbed surfactant tend to coalesce with time. As a result, it is difficult to investigate the properties of a monodisperse compressed emulsion experimentally or by simulations. Even subject to a specified volume fraction, the influence of the droplet size is significant but still not clear. In this work, DPD simulations are employed to study the compressed

doi:10.6342/NTU202404382

emulsion in which the monodisperse droplets are jammed but their coalescences are completely prevented. At quasi-equilibrium, the microstructures of the compressed emulsions are examined for various volume fractions ($\phi$). By analyzing the growth of the projected area and perimeter of droplets with $\phi$, the critical volume fraction corresponding to the turning point is identified as $\phi_c \approx 0.65$. Moreover, the radial distribution function and the coordination number from a reference droplet are acquired. As the volume fraction increases, it is found that the mean coordination number ($\underline{Z}$) rises and can be described by the scaling relation ($\underline{Z}$ - $Z_c$) ~ ($\phi$ - $\phi_c$)$^{0.82}$ with $Z_c \approx 6.3$.

The internal energy per bead ($\underline{U}$) and heat capacity ($\underline{C}_v$) of compressed emulsions are evaluated as well and the effects of the volume fraction, droplet diameter (D), and interfacial tension ($\sigma$) are examined. To analyze the underlying mechanism, $\underline{U}$ is separated into three contributions: continuous phase $\underline{U}_c$, dispersed phase $\underline{U}_d$, and interface $\underline{U}_i$. As $\phi$ is increased or D is decreased, $\underline{U}$ rises because both $\underline{U}_d$ and $\underline{U}_i$ increase. The increment of $\underline{U}_d$ is associated with the buildup of the Laplace pressure, while the increment of $\underline{U}_i$ is accompanied with the growth of the interfacial area. As $\sigma$ is increased, $\underline{U}$ ascends but $\underline{U}_i$ is found to decay surprisingly. The change in $\underline{U}$ is attributed to the growths of both $\underline{U}_d$ and $\underline{U}_c$ associated with the increment of the Laplace pressure. The dependence of the heat capacity on $\phi$, D, and $\sigma$ is the same as the internal energy. According to the dimensional analysis, all the data points can be well represented by the scaling relations ($\underline{C}_v - \underline{C}_{v,c}$) ~ $\phi(\phi-\phi_c)^{1/3}(\sigma/D)$ and ($\underline{U}$ - $\underline{U}_c$) ~ $\phi(\phi-\phi_c)^{1/3}(\sigma/D)$. In addition to structural and thermodynamic properties, our new simulation approach can be applied to explore the mechanical and viscoelastic properties of compressed emulsions, which are currently under study.

doi:10.6342/NTU202404382

## 1-5 Reference

[1] T. Mason, J. Bibette, D. Weitz, Elasticity of compressed emulsions, Phys. Rev. Lett. 75(10) (1995) 2051.

[2] C.-Y. Lu, J. Yu, Dielectric response of a dilute oil-in-water emulsion solution, Chin. J. Phys. 40(1) (2002) 60-68.

[3] H. Princen, A. Kiss, Rheology of foams and highly concentrated emulsions: III. Static shear modulus, J. Colloid Interface Sci. 112(2) (1986) 427-437.

[4] S. Torquato, T.M. Truskett, P.G. Debenedetti, Is random close packing of spheres well defined?, Phys. Rev. Lett. 84(10) (2000) 2064.

[5] R. Foudazi, S. Qavi, I. Masalova, A.Y. Malkin, Physical chemistry of highly concentrated emulsions, Adv. Colloid Interface Sci. 220 (2015) 78-91.

[6] T. Zhang, R.A. Sanguramath, S. Israel, M.S. Silverstein, Emulsion templating: porous polymers and beyond, Macromolecules 52(15) (2019) 5445-5479.

[7] S.-W. Hu, P.-J. Sung, T.P. Nguyen, Y.-J. Sheng, H.-K. Tsao, UV-Resistant Self-Healing Emulsion Glass as a New Liquid-like Solid Material for 3D Printing, ACS Appl. Mater. Interfaces 12(21) (2020) 24450-24457.

[8] V.G. Babak, M.-J. Stébé, Highly concentrated emulsions: physicochemical principles of formulation, J. Dispers. Sci. Technol. 23(1-3) (2002) 1-22.

[9] G. Sun, Z. Li, T. Ngai, Inversion of particle-stabilized emulsions to form high-internal-phase emulsions, Angew. Chem. 122(12) (2010) 2209-2212.

[10] H. Tan, G. Sun, W. Lin, C. Mu, T. Ngai, Gelatin particle-stabilized high internal phase emulsions as nutraceutical containers, ACS Appl. Mater. Interfaces 6(16) (2014) 13977-13984.

[11] T.P. Nguyen, S.-W. Hu, Y.-J. Lin, Y.-J. Sheng, H.-K. Tsao, Coexistence of liquid-like emulsion and solid-like emulsion glass beyond the close-packing limit, J. Taiwan Inst.

doi:10.6342/NTU202404382

Chem. Eng. 115 (2020) 28-34.

[12] T.P. Nguyen, S.-W. Hu, Y.-J. Sheng, H.-K. Tsao, Scanty-water oil-in-water emulsion glasses synthesized through a low-energy process: Nucleation and growth mechanism, J. Taiwan Inst. Chem. Eng. 109 (2020) 129-136.

[13] D. Langevin, S. Poteau, I. Hénaut, J. Argillier, Crude oil emulsion properties and their application to heavy oil transportation, Oil Gas Sci. Technol. 59(5) (2004) 511-521.

[14] N.R. Cameron, High internal phase emulsion templating as a route to well-defined porous polymers, Polymer 46(5) (2005) 1439-1449.

[15] J. Bibette, D. Morse, T. Witten, D. Weitz, Stability criteria for emulsions, Phys. Rev. Lett. 69(16) (1992) 2439.

[16] A. Speltini, G. Tripodo, F. Rinaldi, G. Massolini, A. Profumo, E. Calleri, Carbon nanotubes-modified poly-high internal phase emulsions for pharmaceuticals pre-concentration and determination, J. Pharm. Biomed. Anal. 207 (2022) 114391.

[17] E.M. Shchukina, D.G. Shchukin, Layer-by-layer coated emulsion microparticles as storage and delivery tool, Curr. Opin. Colloid Interface Sci. 17(5) (2012) 281-289.

[18] H. Zhang, H. Makse, Jamming transition in emulsions and granular materials, Phys. Rev. E 72(1) (2005) 011301.

[19] C. Zhang, C.B. O'Donovan, E.I. Corwin, F. Cardinaux, T.G. Mason, M.E. Möbius, F. Scheffold, Structure of marginally jammed polydisperse packings of frictionless spheres, Phys. Rev. E 91(3) (2015) 032302.

[20] A. Jamil, S. Caubet, B. Grassl, T. Kousksou, K. El Omari, Y. Zeraouli, Y. Le Guer, Thermal properties of non-crystallizable oil-in-water highly concentrated emulsions, Colloids Surf. A Physicochem. Eng. Asp. 382(1-3) (2011) 266-273.

[21] R. Pal, A novel method to correlate emulsion viscosity data, Colloids Surf. A Physicochem. Eng. Asp. 137(1-3) (1998) 275-286.

doi:10.6342/NTU202404382

[22] P. Partal, A. Guerrero, M. Berjano, C. Gallegos, Influence of concentration and temperature on the flow behavior of oil-in-water emulsions stabilized by sucrose palmitate, J. Am. Oil Chem. Soc. 74(10) (1997) 1203-1212.

[23] K. Jørgensen, Calorimetric detection of a sub-main transition in long-chain phosphatidylcholine lipid bilayers, Biochim. Biophys. Acta Biomembr. 1240(2) (1995) 111-114.

[24] D. Clausse, F. Gomez, I. Pezron, L. Komunjer, C. Dalmazzone, Morphology characterization of emulsions by differential scanning calorimetry, Adv. Colloid Interface Sci. 117(1-3) (2005) 59-74.

[25] J. Brujić, S.F. Edwards, D.V. Grinev, I. Hopkinson, D. Brujić, H.A. Makse, 3D bulk measurements of the force distribution in a compressed emulsion system, Faraday Discuss. 123 (2003) 207-220.

[26] T. Mason, M.-D. Lacasse, G.S. Grest, D. Levine, J. Bibette, D. Weitz, Osmotic pressure and viscoelastic shear moduli of concentrated emulsions, Phys. Rev. E 56(3) (1997) 3150.

[27] M.-D. Lacasse, G.S. Grest, D. Levine, T. Mason, D. Weitz, Model for the elasticity of compressed emulsions, Phys. Rev. Lett. 76(18) (1996) 3448.

[28] P. Espanol, P. Warren, Statistical mechanics of dissipative particle dynamics, EPL 30(4) (1995) 191.

[29] P. Hoogerbrugge, J. Koelman, Simulating microscopic hydrodynamic phenomena with dissipative particle dynamics, EPL 19(3) (1992) 155.

[30] R.D. Groot, P.B. Warren, Dissipative particle dynamics: Bridging the gap between atomistic and mesoscopic simulation, J. Chem. Phys. 107(11) (1997) 4423-4435.

[31] A.F. Jakobsen, Constant-pressure and constant-surface tension simulations in dissipative particle dynamics, J. Chem. Phys. 122(12) (2005) 124901.

[32] T.-Y. Wang, H.-K. Tsao, Y.-J. Sheng, Perforated Vesicles of ABA Triblock Copolymers with ON/OFF-Switchable Nanopores, Macromolecules 53(23) (2020) 10582-10590.

[33] K.-C. Huang, C.-M. Lin, H.-K. Tsao, Y.-J. Sheng, The interactions between surfactants and vesicles: Dissipative particle dynamics, J. Chem. Phys. 130(24) (2009) 06B622.

[34] Y.-L. Yang, Y.-J. Sheng, H.-K. Tsao, Hybridization of lipids to monolayer and bilayer membranes of triblock copolymers, J. Colloid Interface Sci. 544 (2019) 53-60.

[35] Y.-S. Peng, Z. Wang, K.-C. Chu, Y.-J. Sheng, H.-K. Tsao, Favorable partition of nanoswimmers toward a confined slit, Phys. Rev. E 100(4) (2019) 042604.

[36] I. Pagonabarraga, M. Hagen, D. Frenkel, Self-consistent dissipative particle dynamics algorithm, EPL 42(4) (1998) 377.

[37] H.-Y. Chang, P.-H. Chiu, H.-K. Tsao, Y.-J. Sheng, Strengthening mechanism of the mechanical properties of graft copolymers with incompatible pendant groups: nano-clusters and weak cross-linking, Soft Matter 17(23) (2021) 5730-5737.

[38] Y.-L. Lin, C.-S. Chiou, S.K. Kumar, J.-J. Lin, Y.-J. Sheng, H.-K. Tsao, Self-assembled superstructures of polymer-grafted nanoparticles: effects of particle shape and matrix polymer, J. Phys. Chem. C 115(13) (2011) 5566-5577.

[39] S.-W. Hu, Y.-J. Sheng, H.-K. Tsao, Self-assembly of organophilic nanoparticles in a polymer matrix: Depletion interactions, J. Phys. Chem. C 116(2) (2012) 1789-1797.

[40] F. Alvarez, E. Flores, L. Castro, J. Hernández, A. López, F. Vazquez, Dissipative particle dynamics (DPD) study of crude oil− water emulsions in the presence of a functionalized co-polymer, Energy fuels 25(2) (2011) 562-567.

[41] J. Zhang, L. Chen, A. Wang, Z. Yan, Dissipative particle dynamics simulation of ionic liquid-based microemulsion: Quantitative properties and emulsification mechanism,

Ind. Eng. Chem. Res. 59(2) (2019) 763-773.

[42] M. Li, H. Zhang, Z. Wu, Z. Zhu, X. Jia, DPD Simulation on the Transformation and Stability of O/W and W/O Microemulsions, Molecules 27(4) (2022) 1361.

[43] K.-C. Chu, H.-K. Tsao, Y.-J. Sheng, Pressure-gated capillary nanovalves based on liquid nanofilms, J. Colloid Interface Sci. 560 (2020) 485-491.

[44] H. Liu, G. Cao, Effectiveness of the Young-Laplace equation at nanoscale, Sci. Rep. 6(1) (2016) 1-10.

[45] M. Matsumoto, K. Tanaka, Nano bubble—Size dependence of surface tension and inside pressure, Fluid Dyn. Res. 40(7-8) (2008) 546.

[46] H.-L. Wu, Y.-J. Sheng, H.-K. Tsao, Phase behaviors and membrane properties of model liposomes: Temperature effect, J. Chem. Phys. 141(12) (2014) 09B619_1.

[47] I. Masalova, A.Y. Malkin, Rheology of highly concentrated emulsions–Concentration and droplet size dependencies, Appl. Rheol. 17(4) (2007) 42250-1-42250-9.

doi:10.6342/NTU202404382

# Chapter 2 Solid-like elastic behavior of nanosized concentrated emulsions: size-dependent Young's and bulk moduli

## Abstract

Concentrated emulsions with volume fractions exceeding the critical value have diverse applications in foods, cosmetics, coatings, and pharmaceuticals. They have a jammed structure and tend to exhibit a solid-like behavior. Unfortunately, the mechanical properties of monodisperse concentrated emulsions are challenging to study by experiments or simulations because of thermodynamic instability and droplet coalescence. A mesoscopic simulation method is employed to study the mechanical properties of the concentrated emulsion. Knowledge of the microstructure and interdroplet interaction among monodisperse droplets is not a prerequisite. Effects of the volume fraction ($\phi$), droplet diameter (D), and interfacial tension ($\sigma$) on Young's modulus (E) and bulk modulus (K) are investigated systematically. For $\phi<\phi_c$, Young's modulus is absent and the bulk modulus rises with increase $\phi$. For $\phi>\phi_c$, both Young's and bulk moduli are found to grow with increasing $\phi$ and $\sigma$. However, these solid-like properties become more prominent as D is decreased. On the basis of the interfacial energy per unit volume, our simulation results can be well represented by the relations $E\sim\phi^{0.13}(\phi-\phi_c)^{1.55}(\sigma/D)$ and $K\sim\phi^{1.06}(\phi-\phi_c)^{0.15}(\sigma/D)$. Moreover, the relationship for soft materials $E=3K(1-2\nu)$ is satisfied. The Poisson's ratio ($\nu$) is very close to 0.5 but still decreases slightly with increasing $\phi$.

**Keywords:** monodisperse concentrated emulsion; Young's modulus; bulk modulus; size-dependence; jammed structure; interfacial tension.

doi:10.6342/NTU202404382

## 2-1 Introduction

An emulsion contains two immiscible liquids in which droplets of one liquid (dispersed or internal phase) are dispersed in another liquid (continuous phase) [1-3]. The system is unstable and can become metastable through the addition of surfactants [2, 4]. As the volume fraction of the dispersed phase exceeds the limit of close packing, the droplets are packed together tightly, and the system is called concentrated emulsion or high internal phase emulsion (HIPE) [5]. For monodisperse droplets, the critical volume fraction to develop concentrated emulsions is about 0.74 for the closest packing and 0.64 for random packing [5-8]. The droplets in a concentrated emulsion are jammed and generally adopt polygonal shapes [9, 10]. As a result, the concentrated emulsion exhibits a solid-like behavior, and its disordered structure is reminiscent of a glass state [11-13]. HIPE has a wide range of applications in cosmetic and pharmaceutical industries[14, 15], and it is able to impede sedimentation or creaming because of its jammed structure preventing downward or upward movements of droplets [6, 16].

In concentrated emulsions, the typical work required to adjust the packing structure or alter the positions of the jammed droplets is large compared to the thermal energy [17]. That is, the concentrated emulsion is arrested in a metastable state subjected to external work such as compression, and thus it can withstand the applied stress [17, 18]. Because the mechanical work is not converted to kinetic energy, it is actually stored in the interfacial energy. The ability to store the input work through the deformation of a solid is represented by the elasticity, and it is generally indicated by Young’s modulus, which can be acquired from the stress-strain curve. By using the texture analyzer in parallel plate geometry for uniaxial compression, the stress-strain curves of compressed sunflower oil-in-emulsions were obtained [19]. During the compression treatment, the droplet size distribution did not change significantly because droplet coalescence is weak. Although the

doi:10.6342/NTU202404382

emulsions were polydisperse, Young's moduli were found to grow with increasing the volume fraction of droplets but decreasing the average diameter.

Young's modulus characterizes the response (strain) of a substance to normal compression as the force is applied lengthwise [20]. As a substance is under pressure on all surfaces, its volume is reduced but recovered when the applied pressure is removed. The bulk modulus (K) measures the resistance of a material (solid or fluid) to compression and expresses the change in density as external pressure is applied. It represents the rigidity of the material and the speed of transmission of pressure waves [21]. The inverse of K is often referred to as isothermal compressibility. Evidently, the substance with a large bulk modulus (small compressibility) is difficult to compress [22]. For a fluid, Young's modulus is absent, and only the bulk modulus is meaningful [23]. However, for a solid, there exists a relation between Young's modulus and bulk modulus by Poisson's ratio, which is a measure of the deformation of a substance in directions perpendicular to the specific direction of loading. Poisson's ratio ($\nu$) is specified as the negative of the transverse to axial strain ratio, and its value generally ranges between 0 and 1/2 [24]. The incompressible isotropic material, which deforms elastically at infinitely small strains, gives $\nu = 0.5$. For soft materials like rubber, Poisson's ratio is near 0.5 [25].

Highly concentrated emulsions display a behavior distinctly different from typical liquid-like emulsions because of the jammed structure. The mechanical properties of concentrated emulsions are important in their applications and processing but difficult to measure in experiments due to their soft nature. In this work, the solid-like elastic behavior of concentrated emulsions is explored by dissipative particle dynamics (DPD) simulations. Prior knowledge of the microstructure of emulsions and interdroplet interactions is not required. The influences of the droplet size, the volume fraction of the dispersed phase, and the interfacial tension on the mechanical properties of concentrated emulsions,

doi:10.6342/NTU202404382

including Young's modulus and bulk modulus, will be systematically investigated. Finally, the scaling law between the property and the influencing factors is proposed, and the relationship between the two moduli (E and K) is examined based on Poisson's ratio.

## 2-2 Simulation method

Dissipative particle dynamics (DPD) is a mesoscale simulation. Every DPD bead combines atoms or molecules into a distinct coarse-grained element with mass $m$, and it obeys Newton's equation of motion [26-29]. DPD inherits some of the detailed descriptions of molecular dynamics but allows the simulation for much larger system sizes and up to the microsecond range. The interaction between a pair of DPD beads is soft, short-ranged, and pairwise-additive. It generally consists of three forces: conservative ($\mathbf{F}_{\mathrm{ij}}^{\mathrm{C}}$), dissipative ($\mathbf{F}_{\mathrm{ij}}^{\mathrm{D}}$), and random forces ($\mathbf{F}_{\mathrm{ij}}^{\mathrm{R}}$) [30, 31]. The equilibrium state is governed by the conservative force, $\mathbf{F}_{\mathrm{ij}}^{\mathrm{C}} = \mathrm{a_{ij}}(1 - \mathrm{r_{ij}} / r_c)\hat{\mathbf{r}}_{\mathrm{ij}}$ for $\mathrm{r_{ij}} < r_c$, which becomes zero as $\mathrm{r_{ij}} > r_c$ [16, 32]. The interaction parameter $\mathrm{a_{ij}}$ denotes the maximum repulsion and $\mathrm{r_{ij}}$ is the distance between the beads i and j. $r_c$ represents the interaction range and $\hat{\mathbf{r}}_{\mathrm{ij}}$ is the unit vector along the line joining the beads i and j. $\mathbf{F}_{\mathrm{ij}}^{\mathrm{D}}$ and $\mathbf{F}_{\mathrm{ij}}^{\mathrm{R}}$ between the beads are brought in to describe the hydrodynamic behavior, and the local momentum conservation law is fulfilled [33]. The aforementioned forces have the same interaction range $r_c$. All variables in our simulations are non-dimensionalized. The mass, length, and thermal energy are scaled by $m$, $r_c$, and $k_BT$, respectively.

In our work, the emulsion system comprises droplets of the same size dispersed in the continuous phase. Monodisperse droplets (e.g. oil) are randomly distributed in another liquid phase (e.g. water). The value of $\mathrm{a_{ij}}$ is always set as 25 for the same types of beads; for example, $\mathrm{a_{ww}} = \mathrm{a_{oo}} = 25$ for both water (w) and oil (o) phases. As the incompatibility between the beads i and j grows, $\mathrm{a_{ij}}$ is increased [34]. The interfacial tension ($\sigma$) between

doi:10.6342/NTU202404382

the oil and water phases is affected by the interaction parameter $a_{ow}$, which is assumed in the range of 50 ~ 80. The emulsion is thermodynamically unstable, but it can be maintained at the metastable state by preventing the coalescence of droplets by virtue of the addition of surfactants [2, 35, 36]. The stability of the emulsion is guaranteed by giving a strong repulsion (such as $a^{*}_{oo} = 2000$) between two contacting droplets. This setting is equivalent to the strong repulsive interaction between the layers of surfactants adsorbed on the surface of the two close contact droplets in experiments [37]. Consequently, the deformable droplets which have the same number of DPD beads are in a stable and monodisperse state throughout the simulation.

First, the equilibrium state of the concentrated emulsion was conducted in the canonical ensemble (constant number of beads $N$, simulation box volume $V$, and temperature $T$). The cube box with $V = (32.2)^3$ was used, and the total number of DPD beads in the simulation system was $N = 10^5$. Thereby, the number densities of both dispersed and continuous phases are $\rho \approx 3$. The temperature of the system was always kept at unity ($k_B T = 1$). The equation of motion was integrated by using the velocity Verlet scheme with the time increment $\Delta t = 0.01$. To reach the quasi-equilibrium state of the jammed system, at least $3 \times 10^6$ steps were run. The volume fraction of the dispersed phase ($\phi$) is the ratio of the total beads in the dispersed phase to those of the overall system ($N$). $\phi$ is ranged from 0.1 to 0.95. In the inset of Figure 2-1, a typical snapshot of a concentrated emulsion is demonstrated. The solid-like elastic properties (e.g., the Young's and bulk moduli) of concentrated emulsions were evaluated from the quasi-equilibrium systems for different volume fractions, interfacial tensions, and droplet sizes.

The mechanical responses of concentrated emulsions (Young's and bulk moduli) were determined by the following procedures. For Young's modulus (E), non-equilibrium elon-

doi:10.6342/NTU202404382

gation was performed by a uniaxial deformation on the simulation box under the canonical ensemble (*NVT*) [38]. The box size is increased in the x direction at a constant engineering strain rate ($\Delta L$ per time step), and it is decreased in the y and z directions simultaneously to maintain a constant volume and $\rho = 3$ [39]. The average stress ($\tau$) in the x direction was then evaluated by the deviatoric part of the pressure tensor,

$$\tau = 3(- P_{xx} + P) / 2, \tag{1}$$

where $P = \Sigma_k P_{kk} / 3$ is the equilibrium pressure [38, 39]. The stress-strain relation was obtained to determine Young's modulus at small deformations. For bulk modulus (K), the isothermal-isobaric ensemble (*NPT*) was adopted to reach the equilibrium state. At constant pressure, the instantaneous volume fluctuations of the concentrated emulsion system were monitored. The bulk modulus can be acquired by

$$\mathrm{K} = \frac{\langle V \rangle k_B T}{\langle V^2 \rangle - \langle V \rangle^2}, \tag{2}$$

where $\langle V \rangle$ and $\langle V \rangle^2$ denote the mean values of $V$ and $V^2$ recorded every 100 DPD steps during the simulation, respectively [40]. Periodic boundary conditions are always imposed on each simulation system in the x, y, and z directions.

The interfacial tension $\sigma$ between two immiscible phases can be determined by Irving-Kirkwood expression [41-43]. Consider an oil layer placed in the middle of the simulation box which contains water. The oil-water interface was perpendicular to the z-direction. After obtaining the diagonal components of the pressure tensor $P_{kk}$, the interfacial tension is calculated by $\sigma = [P_{zz}-(P_{xx}+P_{yy})/2](L_z/2)$. The factor of 1/2 associated of $L_z$ is because of the two interfaces in the system. Note that interfacial tension ($\sigma$) and Young's modulus (E) are non-dimensionalized by $k_BT/r_c^2$ and $k_BT/r_c^3$, respectively.

## 2-3 Results and discussion

Since the coalescence between any two droplets is prevented, the monodisperse concentrated emulsion is stable. As the volume fraction of the dispersed phase exceeds the critical value ($\phi_c \approx 0.65$), concentrated emulsions are generally regarded as solid-like liquids. Therefore, they tend to exhibit elasticity and viscoelasticity. In this work, the effects of the volume fraction, droplet size, and interfacial tension on Young's modulus (E) and bulk modulus (K) are investigated. The volume fraction varies from $\phi = 0.1$ to 0.95, the droplet diameter is in the range of D = 6.83 - 17.21, and the interfacial tension between the dispersed and continuous phase is altered from $\sigma = 2.02$ to 3.59. The ranges of $\phi$, D, and $\sigma$ are not specially selected. However, the droplet diameter (D) is limited by the size of the simulation system and the interfacial tension ($\sigma$) is constrained by the interaction parameter $a_{ij}$.

### 2-3-1 Young's modulus of concentrated emulsions

The elastic behavior of a sample is generally expressed by the plot of stress versus strain from the tensile testing. At a constant elongation speed ($v = \Delta L / \Delta t$), the variation of the stress with the deformation ($\Delta L$) is obtained for the concentrated emulsion with specified $\phi$, D, and $\sigma$. Figure 2-1 shows the stress-strain curves at different elongation speeds for concentrated emulsions with $\phi = 0.7$, D = 7.57, and $\sigma = 3.20$. Here the engineering strain ($\varepsilon$) is defined as $\Delta L / L_0$. Similar to the typical stress-strain curve of a solid sample, the stress grows with increasing the strain, reaches the ultimate strength, and begins to decline. In the growth region, the linear regime associated with elastic deformation (Young's modulus) at lower strains is significantly narrower than the nonlinear regime associated with plastic deformation (strain hardening) at higher strains.

The typical elastic and plastic behaviors of the concentrated emulsion can be realized by the relaxation process shown in Supporting Information Figure 2-S1. After the stress reaches the ultimate strength defined in the typical stress-strain curve, the decay of the stress is actually caused by the change of the relative positions of some droplets, leading to the relaxation of the stress in the concentrated emulsion. In experiments, the value of Young's modulus (E) is often found to vary with the elongation speed (v). Moreover, E grows with increasing v [44]. These behaviors have been observed in our simulations. This phenomenon can be realized by the competition between the local relaxation rate and the deformation rate (elongation speed). As the former is fast enough, the local equilibrium is satisfied and Young's modulus should be independent of the elongation speed. In contrast, as the former is relatively slow, the extent of the structure relaxation depends on the elongation speed and thus E varies with v.

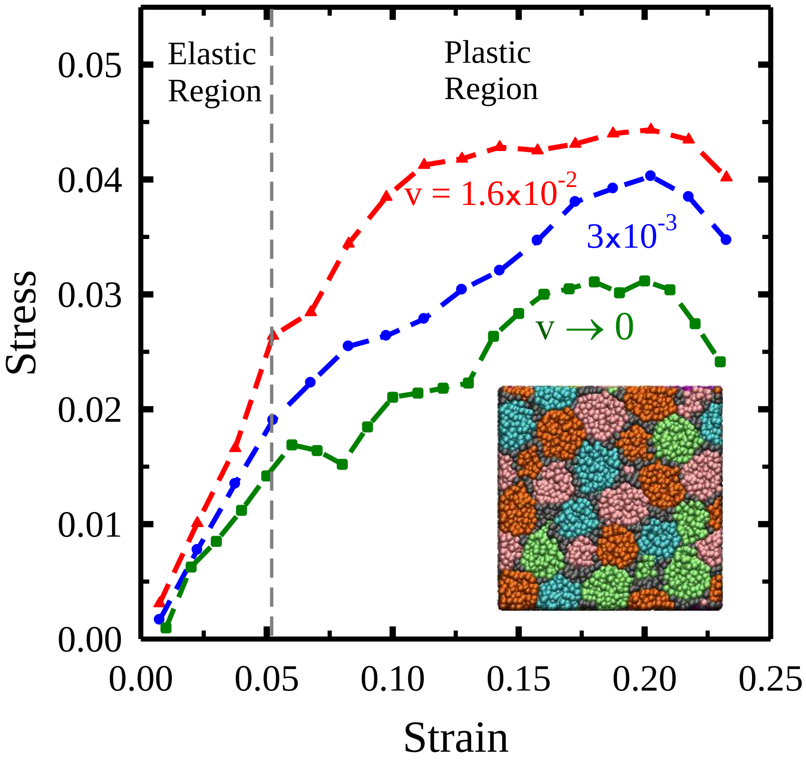

Figure 2-1. The stress-strain curves for the concentrated emulsion with $\phi = 0.7$, $D = 7.57$, and $\sigma = 3.20$ at different elongation speeds (v).

Young's modulus (E) represents the elasticity, and it can be determined from the slope of the linear curve at low strains. Although E depends on the elongation speed, the value

doi:10.6342/NTU202404382

acquired from the quasi-equilibrium stretching process ($v \to 0$) is adopted for simplicity. The influence of the volume fraction on Young's modulus is shown in Figure 2-2 for $D = 7.57$ and $\sigma = 3.20$. As the strain is less than 4%, the linear behavior of the stress-strain curve can be clearly identified, as illustrated in the inset. As expected, Young's modulus increases as the volume fraction grows. Note that Young's modulus vanishes as $\phi < 0.65$, indicating the liquid-like behavior in the absence of the jammed structure. In contrast, as $\phi > \phi_c$, the droplets tend to contact neighboring ones and become jammed with each other. The movement of a droplet is severely constrained by the surrounding droplets. Therefore, the increment of E with the volume fraction is closely related to the degree of crowdedness, which resists the stretching deformation. Since the interfacial area of droplets per unit volume is larger for a higher volume fraction, more work is required to obtain the same displacement of elongation, corresponding to the larger Young's modulus.

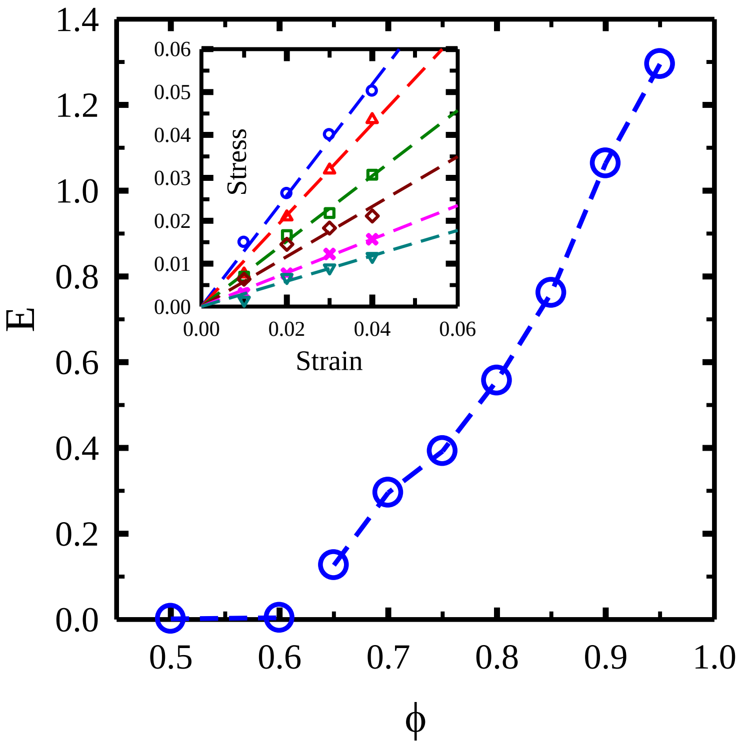

Figure 2-2. The variation of Young's modulus (E) with the volume fraction ($\phi$) at D =

7.57 and $\sigma = 3.20$. The linear relationship between the stress and strain for small deformation is shown in the inset for different values of $\phi$.

At the same volume fraction, the effect of the droplet size on the properties of the system is a unique feature associated with emulsions [16, 45, 46]. Figure 2-3 shows the variation of Young's modulus (E) with the droplet diameter (D) at the same volume fraction ($\phi$) and interfacial tension ($\sigma$). It is interesting to find that E grows linearly with 1/D at specified $\phi$ and $\sigma$. This consequence displays the effect of the interfacial area clearly. For the same $\phi$ and $\sigma$, the interfacial area per unit volume is increased as the droplet size decreases, and it is approximatively proportional to 1/D if the droplet is spherical. The above analysis indicates that Young's modulus is actually proportional to the interfacial area per unit volume. As the droplet size decreases, more interfacial areas are present in the emulsion, and thus more work is required to stretch the system, corresponding to a larger Young's modulus. Until now, one can arrive at the conclusion that E varies with $\phi$ and D, i.e., $E(\phi,D)$. By comparing the three lines at the same diameter of droplets in Figure 2-3, one has an expected result that $E(\phi = 0.95) > E(\phi = 0.80)$ at $\sigma = 3.2$, consistent with Figure 2-2. In addition, another result is $E(\sigma = 3.2) > E(\sigma = 2.4)$ at $\phi = 0.80$, revealing that the interfacial tension also plays an important role in affecting Young's modulus of the emulsion.

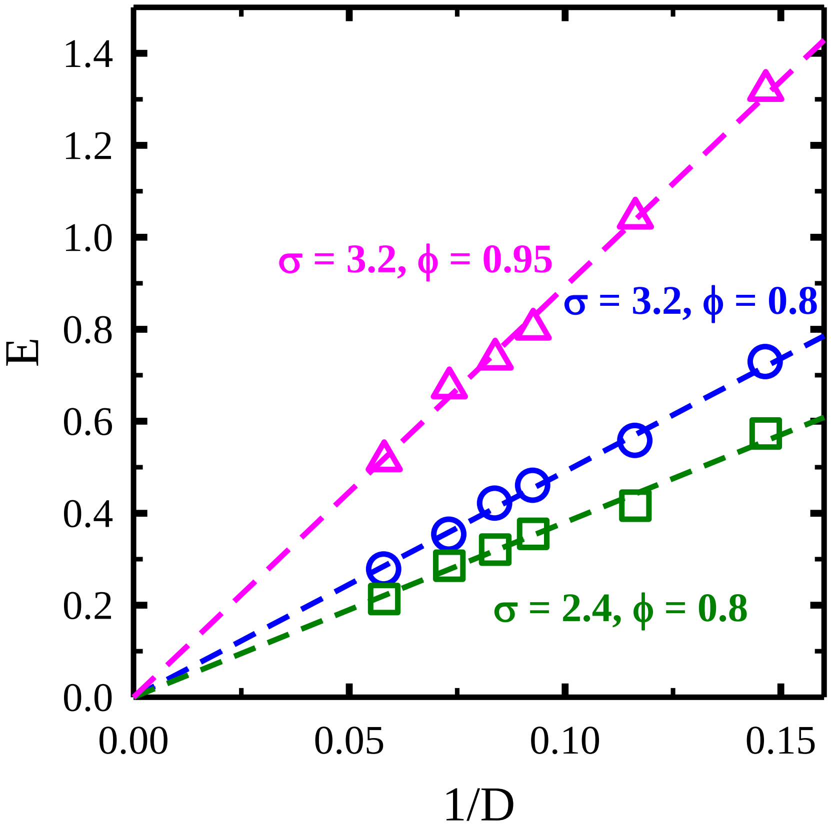

Figure 2-3. The variation of Young's modulus with the inverse of the droplet diameter (1/D) for different combinations of σ and ϕ.

The stored potential energy due to the deformation of concentrated emulsions has to exist in the interfacial energy associated with the liquid-liquid interface. Consequently, the interfacial tension (σ) comes into play, and the larger value of σ can store more work subject to the same deformation. Figure 2-4 shows the variation of Young's modulus with the interfacial tension at the same volume fraction and droplet size. It is found that E grows linearly with increasing σ at specified ϕ and D. The finding in Figure 2-4 implies that Young's modulus is indeed proportional to the interfacial energy per unit volume, which is the product of the interfacial tension and area per unit volume. As the interfacial tension rises, more interfacial energy is present in the emulsion, and thereby more work

doi:10.6342/NTU202404382

is required to expand the system, corresponding to a larger Young's modulus. Clearly, the aforementioned outcomes indicate the three factors $\phi$, D, and $\sigma$ affect Young's modulus, i.e., E($\phi$,D,$\sigma$). Again, by comparing the three lines at the same interfacial tension in Figure 2-4, one has expected results, E($\phi$ = 0.95) > E($\phi$ = 0.80) at D = 8.6 and E(D = 8.6) > E(D = 9.8) at $\phi$ = 0.8, in agreement with Figures 2-2 and 2-3. Because the linearity is always observed in those Figures, a simple relationship of E($\phi$,D,$\sigma$) may be obtained based on some simple arguments.

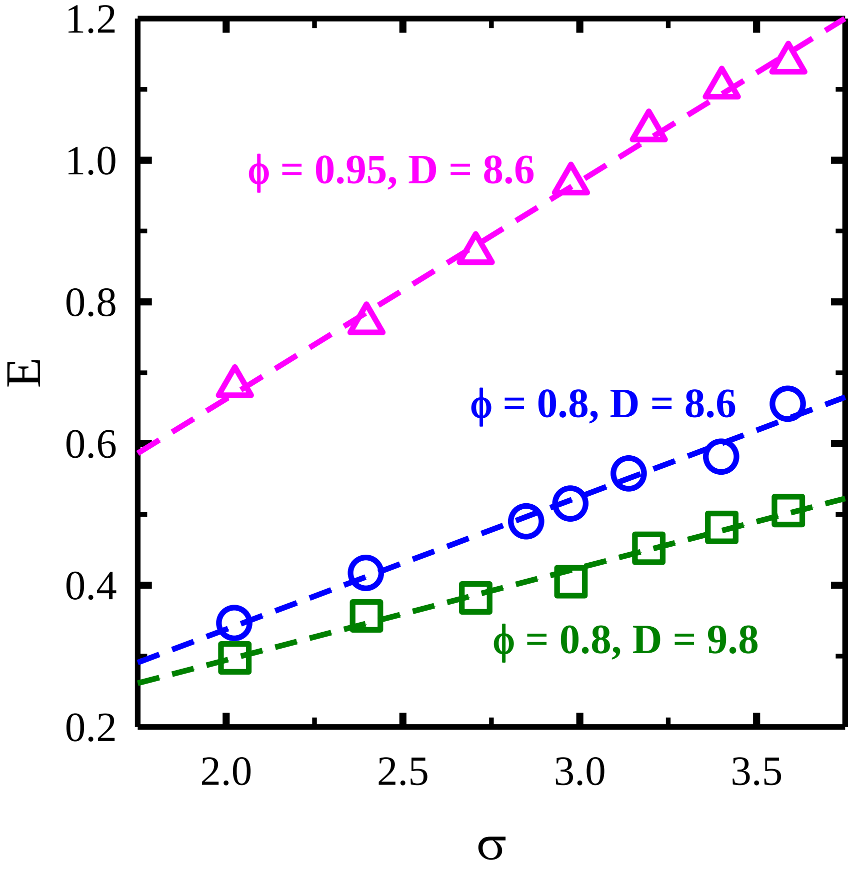

Figure 2-4. The variation of Young's modulus with the interfacial tension ($\sigma$) for various combinations of D and $\phi$.

The above analyses show that Young's modulus (E) ascends with increasing $\phi$ and $\sigma$ but descends with increasing D. According to the Young-Laplace equation, the normal

doi:10.6342/NTU202404382

stress difference across a curved surface is proportional to the ratio of the interfacial tension to the droplet size $\sigma/D$. As a result, Young's modulus, which has the same unit as the normal stress, is expected to be a function of $\sigma/D$. The data points depicted in the inset of Figure 2-5a represent the variation of E with D and $\sigma$ at a specified volume fraction $\phi = 0.8$. When these data points are replotted as E against $\sigma/D$, it is observed that all data points are collapsed reasonably into a single line, as demonstrated in Figure 2-5a. This consequence indicates that there is a linear relationship between E and $\sigma/D$. At a specified combination of $\sigma$ and D, Young's modulus rises with increasing $\phi$ but vanishes as $\phi < \phi_c$. For concentrated emulsions, the dependence of the physical properties on $\phi$ is often described by $\phi^\alpha(\phi - \phi_c)^\beta$ [47-49]. As demonstrated in the inset of Figure 2-5b, E is found to grow linearly with $\phi^{0.13}(\phi - \phi_c)^{1.55}$ but the slope and intercept vary with the combination of $\sigma$ and D. To eliminate the influence associated with the critical volume fraction, the relative Young's modulus which is defined as $\Delta E = E(\phi) - E(\phi_c)$ is used. The aforementioned analyses suggest that the effects of $\phi$, $\sigma$, and D on E can be realized by the plot of $\Delta E/(\sigma/D)$ against $\phi^{0.13}(\phi - \phi_c)^{1.55}$ for various combinations. As shown in Figure 2-5b, all data points can be represented reasonably by a single linear line, revealing that E is linearly proportional to $\phi^{0.13}(\phi - \phi_c)^{1.55}(\sigma / D)$.

doi:10.6342/NTU202404382

(a) Function of σ/D

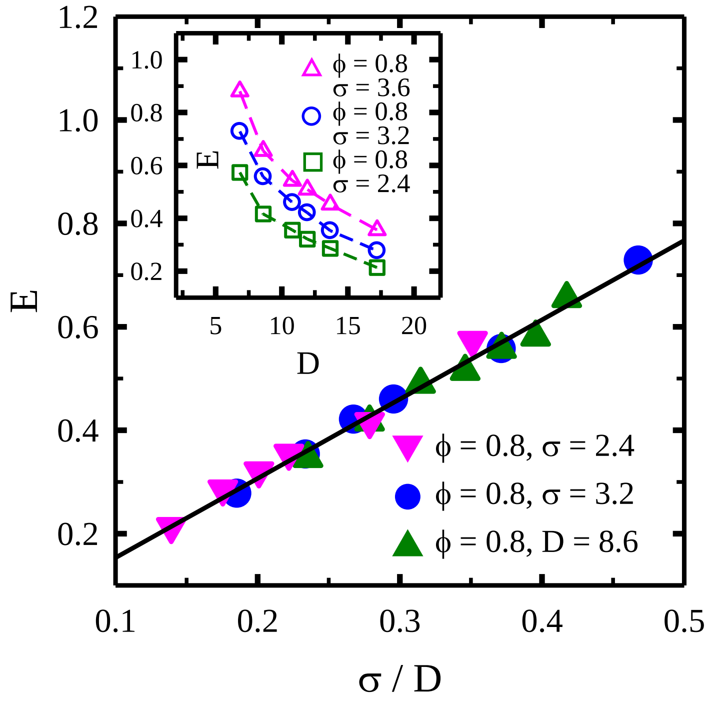

(b) Function of (ϕ - ϕc)

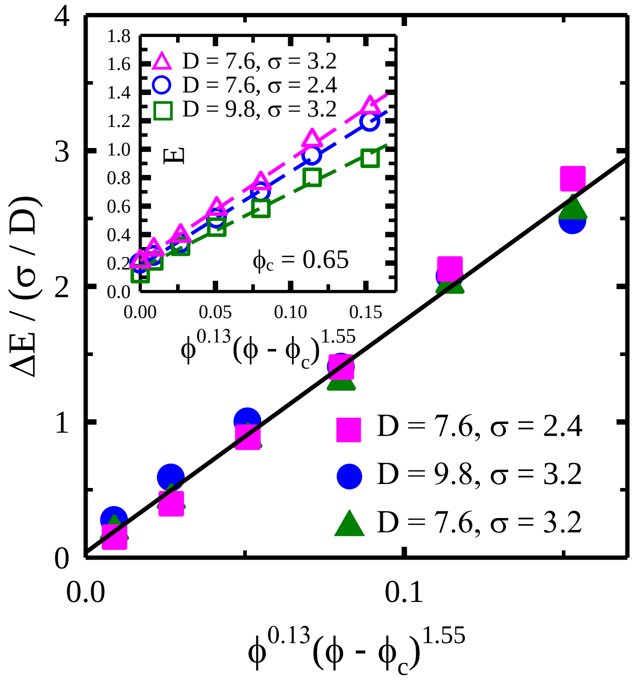

Figure 2-5. (a) The plot of E against σ/D for various combinations of σ and D at ϕ = 0.8.

E is plotted against D for different $\sigma$ in the inset. (b) The plot of $\Delta E/(\sigma/D)$ against $\phi^{0.13}(\phi - \phi_c)^{1.55}$ for different combinations of $\phi$, $\sigma$, and D. In the inset, E is plotted against $\phi^{0.13}(\phi - \phi_c)^{1.55}$. Here $\phi_c$ is determined as 0.65.

### 2-3-2 Bulk modulus of concentrated emulsions

The bulk modulus (K) of a material represents a measure of the ability of a solid or fluid resisting compression on all surfaces. It is defined as the ratio of the applied infinitesimal pressure to the relative decrease of the volume, $K = -V(\partial P/\partial V)_T > 0$. For a typical solid, the bulk modulus is related to Young's modulus by $E = 3K(1 - 2\nu)$, where $\nu$ represents Poisson's ratio which ranges between 0.0 and 0.5 generally. For a fluid, Young's modulus is absent, and the reciprocal of the bulk modulus is referred to as isothermal compressibility [50]. The bulk modulus can be determined from the fluctuation of the volume of the equilibrium system ($V$). The typical fluctuation of $V$ with time is demonstrated in the inset of Figure 2-6 for $\phi = 0.85$ (solid-like state). Figure 2-6 shows the variation of the bulk modulus with the volume fraction at D = 7.57 and $\sigma$ = 3.20. The sharp change of K is evidently observed in the range of $\phi$ = 0.6~0.7, showing the emergence of jamming associated with a structural transition. That is, the behavior of the emulsion changes from the liquid-like ($\phi < \phi_c$) to solid-like ($\phi > \phi_c$) state due to the jammed structure.

doi:10.6342/NTU202404382

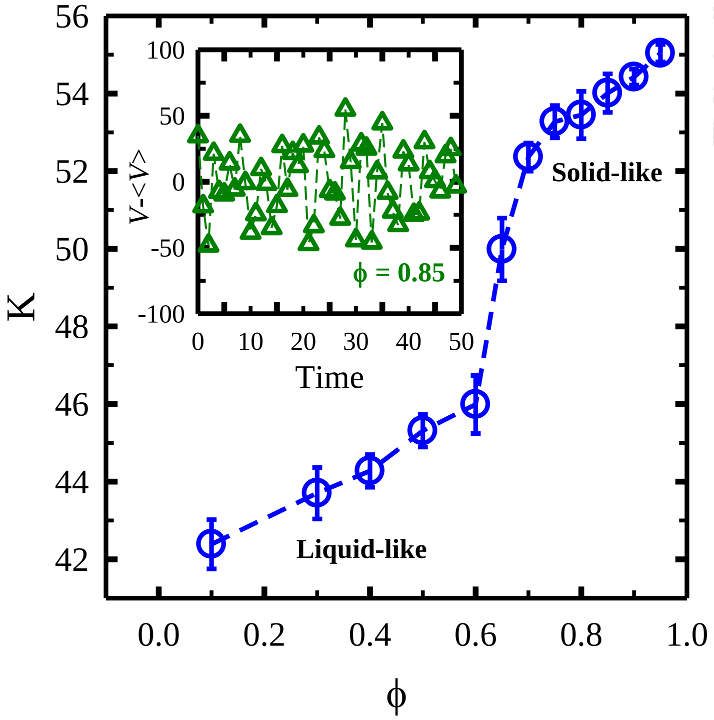

Figure 2-6. The variation of the bulk modulus (K) with the volume fraction ($\phi$) for D = 7.57 and $\sigma$ = 3.20. In the inset, the typical volume fluctuation ($V - \langle V \rangle$) is plotted against the time.

At fixed volume fraction and interfacial tension, the effect of the droplet size on the ability of the concentrated emulsion to withstand changes in volume when under compression on all sides can be understood from the bulk modulus. Figure 2-7 shows the variation of K with D for different combinations of $\phi$ and $\sigma$. As the droplet diameter decreases, the bulk modulus is found to increase, suggesting that the concentrated emulsion with smaller droplets is more elastic. This result of K(D) is in agreement with that of E(D). That is, subject to the same volume compression, more interfacial areas change in the system with smaller droplets, leading to more stored interfacial energy and higher bulk modulus. The quantitative dependence of K on D can be revealed from the plot of K against 1/D, and the linear relationship between them is observed for different combinations of ϕ and σ. Similar to E(ϕ, D), K is a function of ϕ and D, K(ϕ, D), and it is supposed to vary with σ following the analysis of Young's modulus. In fact, Figure 2-7 reveals that K(σ = 3.2) > K(σ = 2.4) regardless of the droplet size at ϕ = 0.8.

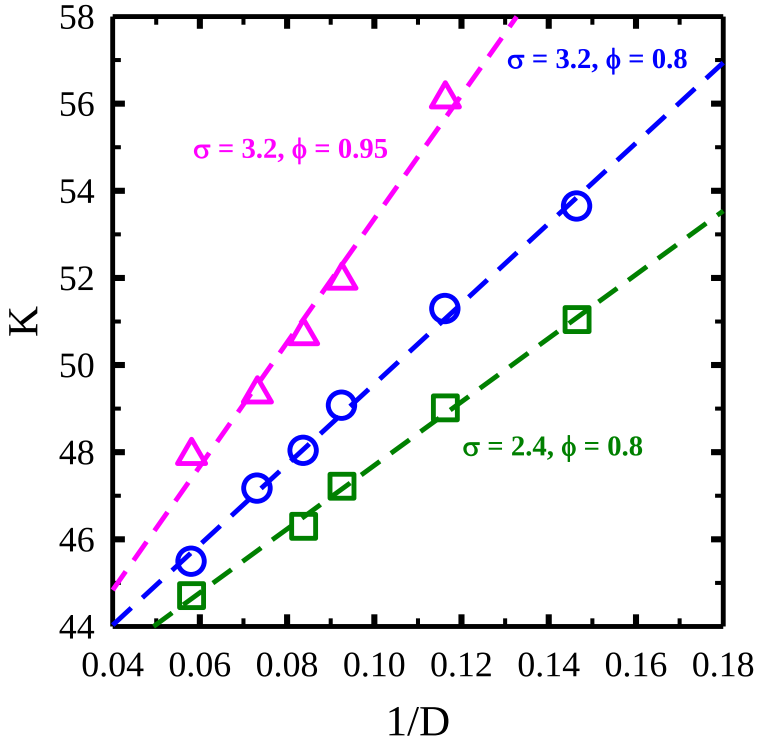

Figure 2-7. The variation of the bulk modulus (K) with the inverse of the droplet diameter (1/D) for different combinations of ϕ and σ.

Figure 2-8 illustrates the variation of K with σ for different combinations of ϕ and D. It is observed that the bulk modulus ascends linearly with increasing interfacial tension. Again, this result of K(σ) is similar to that of E(σ) depicted in Figure 2-4. At the same compression of the system volume and the increment of the liquid-liquid interfacial area, the interfacial energy generated by the deformation of the droplets grows with increasing interfacial tension. Consequently, the bulk modulus is proportional to interfacial tension, in addition to 1/D. The above results show that the bulk modulus (K) rises with increasing

doi:10.6342/NTU202404382

$\phi$ and $\sigma$, but declines with increasing D, similar to Young's modulus. Following the same arguments based on the Young-Laplace equation, the data points shown in the inset of Figure 2-9a for $\phi = 0.8$ are replotted against $\sigma$/D. Again, K($\sigma$,D) can be well represented by a linear function of $\sigma$/D, as illustrated in Figure 2-9a. Furthermore, the dependence of the dimensionless bulk modulus K/($\sigma$/D) of concentrated emulsions on the volume fraction is examined by the expression $\phi^{\alpha}(\phi - \phi_c)^{\beta}$ [47-49]. Because the bulk modulus of emulsions still exists as $\phi < \phi_c$, the relative bulk modulus, which is defined as $\Delta K = K(\phi) - K(\phi_c)$, is adopted. Figure 2-9b shows that all data points can be depicted reasonably by a single linear line, suggesting that K is linearly proportional to $\phi^{1.06}(\phi - \phi_c)^{0.15}(\sigma / D)$.

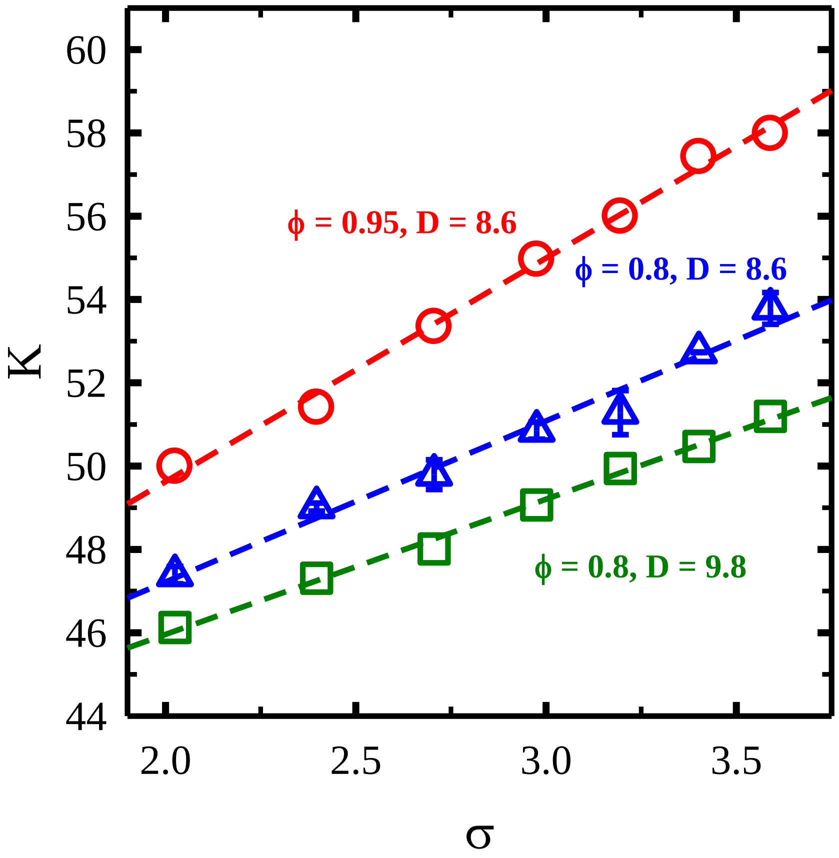

Figure 2-8. The bulk modulus (K) is plotted against the interfacial tension ($\sigma$) for different combinations of $\phi$ and D.

(a) Function of σ/D

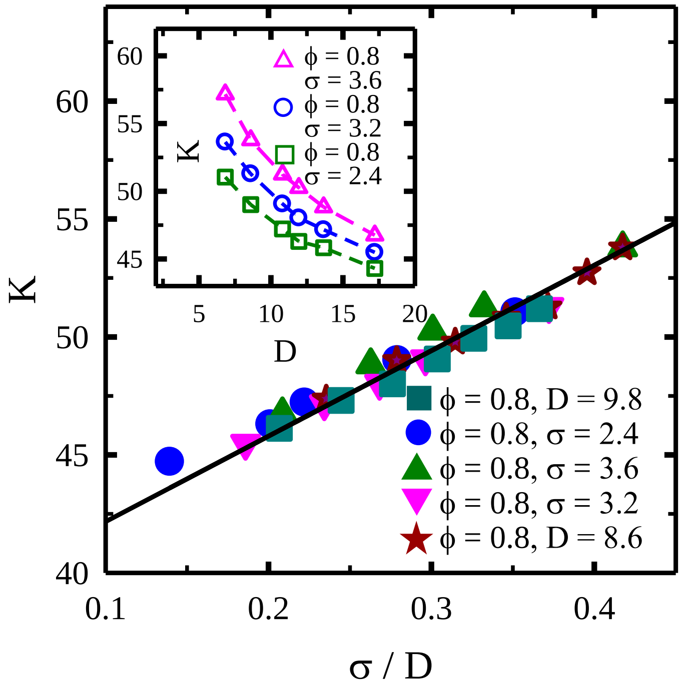

(b) Function of $(\phi - \phi_c)$

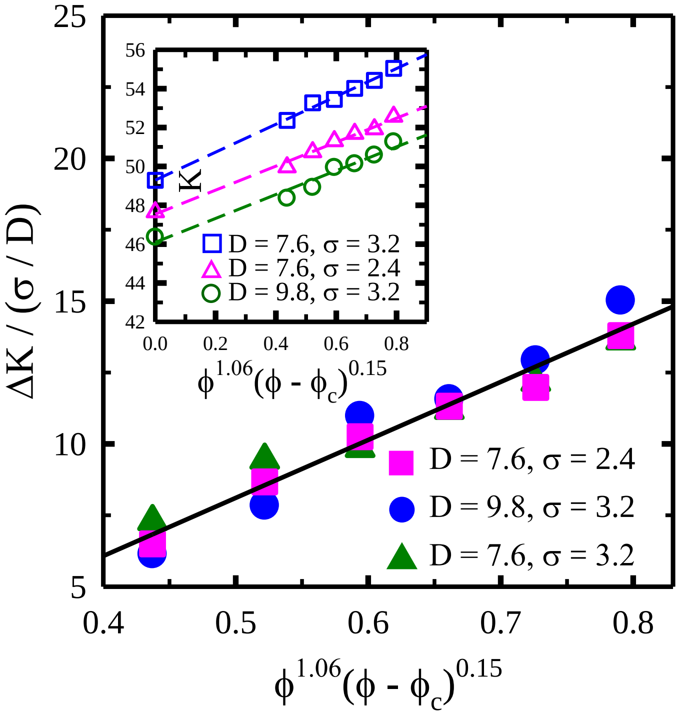

Figure 2-9. (a) The plot of K against σ/D for various combinations of σ and D at $\phi = 0.8$. K is plotted against D in the inset. (b) The plot of $\Delta K/(\sigma/D)$ against $\phi^{1.06}(\phi - \phi_c)^{0.15}$ for

different combinations of $\phi$, $\sigma$, and D. In the inset, K is plotted against $\phi^{1.06}(\phi - \phi_c)^{0.15}$. Here $\phi_c$ is determined as 0.65.

Poisson's ratio ($\nu$) is defined as the negative ratio of the amount of lateral contraction ($\varepsilon_{lateral}$) to that of axial elongation ($\varepsilon_{axial}$) in response to an applied load, $\nu = -\varepsilon_{lateral}/\varepsilon_{axial}$ [51]. For isotropic and homogeneous materials, Poisson's ratio can be estimated from the Young's and bulk moduli, $\nu = (1\text{-}E/3K)/2$. Figure 2-10 shows the variation of $\nu$ with the volume fraction for concentrated emulsions with three combinations of interfacial tensions and droplet sizes. It is found that all values of $\nu$ are very close to 0.5, but it still decreases slightly with increasing $\phi$. The data points of the three systems are close to each other and can be described by the expression by $\nu(\phi) = [1\text{-}\ E(\phi) / 3K(\phi)] / 2$, revealing that Poisson's ratio depends weakly on $\sigma$ and D. Poisson's ratio of the concentrated emulsion can also be calculated from the relation between Young's modulus and shear modulus (G), $E = 2G(1+\nu)$. For the system with $\phi = 0.8$, $\sigma = 3.2$, and $D = 7.57$, the Young's, bulk, and shear moduli are obtained by the simulations of LAMMPs, $E = 1.057$, $K = 54.4$, and $G = 0.353$. As a consequence, one has $\nu = 0.497$ based on the shear modulus, which is very close to the outcome based on the bulk modulus. Our results of concentrated emulsions are consistent with $\nu$ of soft materials, which generally have the bulk modulus (K) much higher than the shear modulus (G), giving Poisson's ratio near 0.5.

doi:10.6342/NTU202404382

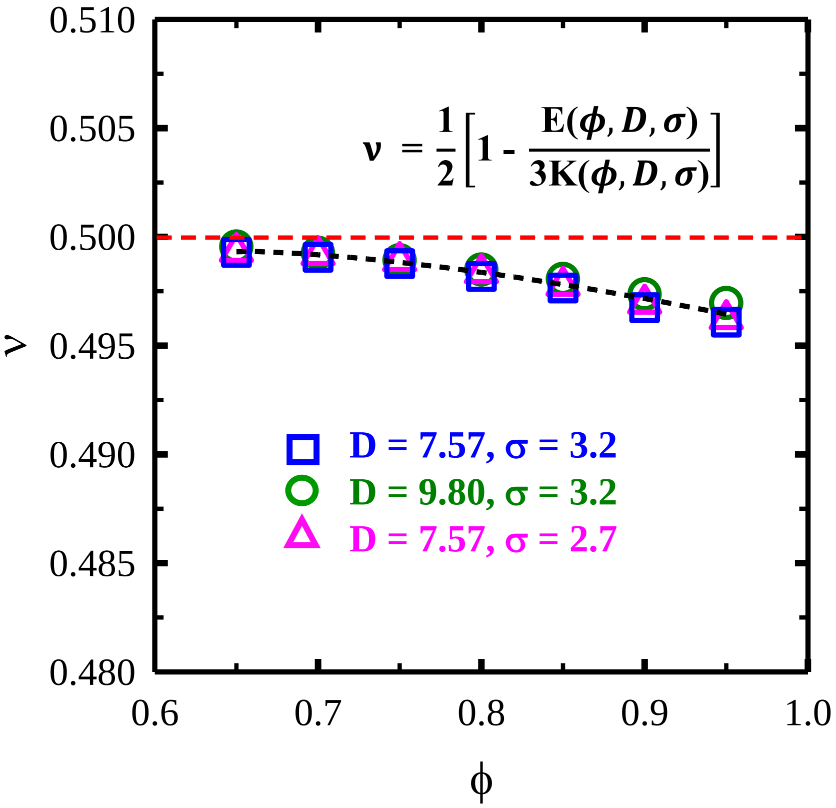

Figure 2-10. Poisson's ratio ($\nu$) is plotted against the volume fraction ($\phi$) for different combinations of $\sigma$ and D. The data points of the three systems are close to each other.

## 2-4 Conclusion

The concentrated emulsions with volume fractions exceeding the critical value ($\phi_c$) display an elastic solid-like behavior due to their jammed structures. In this work, the mechanical properties, including Young's modulus (E) and bulk modulus (K) of monodisperse concentrated emulsions, are explored by DPD simulations. The influences of the volume fraction ($\phi$), droplet size (D), and interfacial tension ($\sigma$) are examined systematically. As $\phi < \phi_c$ ($\approx 0.65$), the emulsion exhibits the liquid-like behavior, and thus Young's modulus vanishes. Nonetheless, the bulk modulus exists and ascends with increasing $\phi$. For $\phi > \phi_c$, E determined at an infinitely low elongation speed emerges, and it grows with increasing $\phi$. Similarly, K rises with $\phi$ but increases rapidly near $\phi_c$, signifying the liquid-

doi:10.6342/NTU202404382

solid transition.

In addition to the volume fraction, the droplet size and interfacial tension are found to affect the behavior of concentrated emulsions significantly. Both Young's and bulk moduli grow as D decreases or $\sigma$ increases. Those consequences can be realized by the fact that more elastic work stored in the interfacial free energy is required for the larger Young's modulus. Therefore, E is proportional to the interfacial energy per unit volume ($\sigma D^2/D^3 = \sigma/D$). On the basis of the dimensional analysis, all the simulation data points agree well with the scaling relations $E(\phi) - E(\phi_c) \sim \phi^{0.13}(\phi - \phi_c)^{1.55}(\sigma / D)$ and $K(\phi) - K(\phi_c) \sim \phi^{1.06}(\phi - \phi_c)^{0.15} (\sigma / D)$. The $\phi$-dependent Young's and bulk moduli satisfy the relation $E = 3K(1 - 2\nu)$ valid for isotropic and homogeneous solids. Poisson's ratio $\nu$ of concentrated emulsions is very close to 0.5 in agreement with soft materials, but it still decreases slightly with increasing $\phi$. To further understand the solid-like properties of concentrated emulsions, the shear modulus and yield stress are currently under study.

## 2-5 Reference

[1] Z.A. Chen, F. Huang, P.A. Tsai, A. Komrakova, Numerical study of microfluidic emulsion dynamics under the influence of heterogeneous surface wettability, Int. J. Multiph. Flow 147 (2022) 103863. https://doi.org/10.1016/j.ijmultiphaseflow.2021.103863.

[2] J.I. Contreras-Ramírez, J.A. Gallegos-Infante, W. Rosas-Flores, R.F. González-Laredo, J.F. Toro-Vázquez, J.D. Pérez-Martínez, Relationship of rheological and thermal properties in organogel emulsions (W/O): Influence of temperature, time, and surfactant concentration on thermomechanical behavior, J. Mol. Liq. 337 (2021) 116403. https://doi.org/10.1016/j.molliq.2021.116403.

[3] G. Chen, D. Tao, An experimental study of stability of oil-water emulsion, Fuel

Process. Technol. 86(5) (2005) 499-508. https://doi.org/10.1016/j.fuproc.2004.03.010.

[4] A.K. Barkat, A. Naveed, M.S.K. Haji, W. Khalid, M. Tariq, R. Akhtar, I. Muhammad, K. Haroon, Basics of pharmaceutical emulsions: A review, Afr. J. Pharmacy Pharmacol. 5(25) (2011) 2715-2725. https://doi.org/10.1016/j.msec.2019.01.137.

[5] R. Foudazi, S. Qavi, I. Masalova, A.Y. Malkin, Physical chemistry of highly concentrated emulsions, Adv. Colloid Interface Sci. 220 (2015) 78-91. https://doi.org/10.1016/j.cis.2015.03.002.

[6] H. Gao, L. Ma, C. Cheng, J. Liu, R. Liang, L. Zou, W. Liu, D.J. McClements, Review of recent advances in the preparation, properties, and applications of high internal phase emulsions, Trends Food Sci. Technol. 112 (2021) 36-49. https://doi.org/10.1016/j.tifs.2021.03.041.

[7] T.P. Nguyen, S.-W. Hu, Y.-J. Lin, Y.-J. Sheng, H.-K. Tsao, Coexistence of liquid-like emulsion and solid-like emulsion glass beyond the close-packing limit, J. Taiwan Inst. Chem. Eng. 115 (2020) 28-34. https://doi.org/10.1016/j.jtice.2020.10.006.

[8] J. Su, Y. Cai, K. Tai, Q. Guo, S. Zhu, L. Mao, Y. Gao, F. Yuan, P. Van der Meeren, High-internal-phase emulsions (HIPEs) for co-encapsulation of probiotics and curcumin: Enhanced survivability and controlled release, Food Funct. 12(1) (2021) 70-82. https://doi.org/10.1039/D0FO01659D.

[9] W. Liu, H. Gao, D.J. McClements, L. Zhou, J. Wu, L. Zou, Stability, rheology, and β-carotene bioaccessibility of high internal phase emulsion gels, Food Hydrocoll. 88 (2019) 210-217. https://doi.org/10.1016/j.foodhyd.2018.10.012.

[10] T. Mason, New fundamental concepts in emulsion rheology, Curr. Opin. Colloid

doi:10.6342/NTU202404382

Interface Sci. 4(3) (1999) 231-238. https://doi.org/10.1016/S1359-0294(99)00035-7.

[11] S.-W. Hu, P.-J. Sung, T.P. Nguyen, Y.-J. Sheng, H.-K. Tsao, UV-Resistant Self-Healing Emulsion Glass as a New Liquid-like Solid Material for 3D Printing, ACS Appl. Mater. Interfaces 12(21) (2020) 24450-24457. https://doi.org/10.1021/acsami.0c04121.

[12] T.P. Nguyen, S.-W. Hu, Y.-J. Sheng, H.-K. Tsao, Scanty-water oil-in-water emulsion glasses synthesized through a low-energy process: Nucleation and growth mechanism, J. Taiwan Inst. Chem. Eng. 109 (2020) 129-136. https://doi.org/10.1016/j.jtice.2020.02.018.

[13] T.H. Vo, P.K. Lam, Y.-J. Sheng, H.-K. Tsao, Amphibious superamphiphilic polystyrene monolith with underwater superoleophilicity: Capture of underwater oil, Appl. Surf. Sci. 570 (2021) 151142. https://doi.org/10.1016/j.apsusc.2021.151142.

[14] Y.-T. Xu, C.-H. Tang, B.P. Binks, High internal phase emulsions stabilized solely by a globular protein glycated to form soft particles, Food Hydrocoll. 98 (2020) 105254. https://doi.org/10.1016/j.foodhyd.2019.105254.

[15] H. Tan, G. Sun, W. Lin, C. Mu, T. Ngai, Gelatin particle-stabilized high internal phase emulsions as nutraceutical containers, ACS Appl. Mater. Interfaces 6(16) (2014) 13977-13984. https://doi.org/10.1021/am503341j.

[16] H.-Y. Chang, Y.-J. Sheng, H.-K. Tsao, Packing microstructures and thermal properties of compressed emulsions: effect of droplet size, J. Mol. Liq. (2022) 120025. https://doi.org/10.1016/j.molliq.2022.120025.

[17] J. Brujić, S.F. Edwards, I. Hopkinson, H.A. Makse, Measuring the distribution of interdroplet forces in a compressed emulsion system, Phys. A: Stat. Mech. Appl.

327(3-4) (2003) 201-212. https://doi.org/10.1016/S0378-4371(03)00477-1.

[18] M. Cates, J. Wittmer, J.-P. Bouchaud, P. Claudin, Jamming and static stress transmission in granular materials, Chaos: An Interdisciplinary Journal of Nonlinear Science 9(3) (1999) 511-522. https://doi.org/10.1063/1.166456.

[19] G.A. van Aken, Flow-induced coalescence in protein-stabilized highly concentrated emulsions, Langmuir 18(7) (2002) 2549-2556. https://doi.org/10.1021/la011540s.

[20] H. Williams, Measuring Young's modulus with a tensile tester, Phys. Educ. 57(2) (2022) 025016. http://dx.doi.org/10.1088/1361-6552/ac3f75.

[21] H. Gholizadeh, R. Burton, G. Schoenau, Fluid bulk modulus: a literature survey, Int. J. Fluid Power. 12(3) (2011) 5-15. https://doi.org/10.1080/14399776.2011.10781033.

[22] Britannica, The Editors of Encyclopaedia. "bulk modulus". Encyclopedia Britannica, 1 Jun. 2006, https://www.britannica.com/science/bulk-modulus. Accessed 12 September 2022.

[23] R. Nave, Bulk elastic properties, HyperPhysics, Georgia State University2016.

[24] Y.-J. Lee, S.-M. Lim, S.-M. Yi, J.-H. Lee, S.-g. Kang, G.-M. Choi, H.N. Han, J.-Y. Sun, I.-S. Choi, Y.-C. Joo, Auxetic elastomers: mechanically programmable meta-elastomers with an unusual Poisson's ratio overcome the gauge limit of a capacitive type strain sensor, Extreme Mech. Lett. 31 (2019) 100516. https://doi.org/10.1016/j.eml.2019.100516.

[25] G.N. Greaves, A.L. Greer, R.S. Lakes, T. Rouxel, Poisson's ratio and modern materials, Nat. Mater. 10(11) (2011) 823-837. https://doi.org/10.1038/nmat3134.

[26] H.-Y. Chang, P.-H. Chiu, H.-K. Tsao, Y.-J. Sheng, Strengthening mechanism of the mechanical properties of graft copolymers with incompatible pendant groups: nano-

clusters and weak cross-linking, Soft Matter 17(23) (2021) 5730-5737. https://doi.org/10.1039/D1SM00472G.

[27] H.-Y. Chang, Y.-J. Sheng, H.-K. Tsao, Structural and mechanical characteristics of polymersomes, Soft Matter 10(34) (2014) 6373-6381. https://doi.org/10.1039/C4SM01092B.

[28] Y.-J. Sheng, T.-Y. Wang, W.M. Chen, H.-K. Tsao, A-B diblock copolymer micelles: Effects of soluble-block length and component compatibility, J. Phys. Chem. B 111(37) (2007) 10938-10945. https://doi.org/10.1021/jp073408s.

[29] F. Alvarez, E. Flores, L. Castro, J. Hernández, A. López, F. Vazquez, Dissipative particle dynamics (DPD) study of crude oil-water emulsions in the presence of a functionalized co-polymer, Energy Fuels 25(2) (2011) 562-567. https://doi.org/10.1021/ef1012038.

[30] Y.-L. Yang, Y.-J. Sheng, H.-K. Tsao, Hybridization of lipids to monolayer and bilayer membranes of triblock copolymers, J. Colloid Interface Sci. 544 (2019) 53-60. https://doi.org/10.1016/j.jcis.2019.02.071.

[31] Y.-S. Peng, Z. Wang, K.-C. Chu, Y.-J. Sheng, H.-K. Tsao, Favorable partition of nanoswimmers toward a confined slit, Phys. Rev. E 100(4) (2019) 042604. https://doi.org/10.1103/PhysRevE.100.042604.

[32] R.D. Groot, P.B. Warren, Dissipative particle dynamics: Bridging the gap between atomistic and mesoscopic simulation, J. Chem. Phys. 107(11) (1997) 4423-4435. http://dx.doi.org/10.1063/1.474784.

[33] J. Xu, C. Yang, Y.-J. Sheng, H.-K. Tsao, Apparent hydrodynamic slip induced by density inhomogeneities at fluid-solid interfaces, Soft Matter 11(35) (2015) 6916-6920. https://doi.org/10.1039/C5SM01627D.

[34] H.-C. Tsai, Y.-L. Yang, Y.-J. Sheng, H.-K. Tsao, Formation of asymmetric and

symmetric hybrid membranes of lipids and triblock copolymers, Polymers 12(3) (2020) 639. https://doi.org/10.3390/polym12030639.

[35] Y. Wei, Y. Xie, Z. Cai, Y. Guo, M. Wu, P. Wang, R. Li, H. Zhang, Interfacial and emulsion characterisation of chemically modified polysaccharides through a multiscale approach, J. Colloid Interface Sci. 580 (2020) 480-492. https://doi.org/10.1016/j.jcis.2020.07.048.

[36] R. Zheng, J. Tian, B.P. Binks, Z. Cui, W. Xia, J. Jiang, Oil-in-Water emulsions stabilized by alumina nanoparticles with organic electrolytes: Fate of particles, J. Colloid Interface Sci. 627 (2022) 749-760. https://doi.org/10.1016/j.jcis.2022.07.085.

[37] F. Ravera, K. Dziza, E. Santini, L. Cristofolini, L. Liggieri, Emulsification and emulsion stability: The role of the interfacial properties, Adv. Colloid Interface Sci. 288 (2021) 102344. https://doi.org/10.1016/j.cis.2020.102344.

[38] T. Jiang, L. Wang, J. Lin, Mechanical properties of designed multicompartment gels formed by ABC graft copolymers, Langmuir 29(39) (2013) 12298-12306. https://doi.org/10.1021/la403098p.

[39] T. Zhang, S. Biswas, J. Cuthbert, T. Kowalewski, K. Matyjaszewski, A.C. Balazs, Understanding the origin of softness in structurally tailored and engineered macromolecular (STEM) gels: A DPD study, Polymer 208 (2020) 122909. https://doi.org/10.1016/j.polymer.2020.122909.

[40] A. Rajabpour, L. Seidabadi, M. Soltanpour, Calculating the bulk modulus of iron and steel using equilibrium molecular dynamics simulation, Procedia Materials Science 11 (2015) 391-396. http://dx.doi.org/10.1016/j.mspro.2015.11.005.

[41] J. Irving, J.G. Kirkwood, The statistical mechanical theory of transport processes. IV. The equations of hydrodynamics, J. Chem. Phys. 18(6) (1950) 817-829.

doi:10.6342/NTU202404382

https://doi.org/10.1063/1.1747782.

[42] J.G. Kirkwood, F.P. Buff, The statistical mechanical theory of surface tension, J. Chem. Phys. 17(3) (1949) 338-343. https://doi.org/10.1063/1.1747248.

[43] Y.-H. Tsao, T.-Y. Wang, H.-K. Tsao, Y.-J. Sheng, Thermally assisted mobility of nanodroplets on surfaces with weak defects, J. Colloid Interface Sci. 604 (2021) 150-156. https://doi.org/10.1016/j.jcis.2021.06.163.

[44] M. Khandelwal, P. Ranjith, Z. Pan, J.G. Sanjayan, Effect of strain rate on strength properties of low-calcium fly-ash-based geopolymer mortar under dry condition, Arab. J. Geosci. 6 (2013) 2383-2389. http://dx.doi.org/10.1007/s12517-011-0507-0.

[45] R. Pal, Effect of droplet size on the rheology of emulsions, AIChE J. 42(11) (1996) 3181-3190. https://doi.org/10.1002/aic.690421119.

[46] W. Chantrapornchai, F. Clydesdale, D.J. McClements, Influence of droplet size and concentration on the color of oil-in-water emulsions, J. Agric. Food Chem. 46(8) (1998) 2914-2920. https://doi.org/10.1021/jf980278z.

[47] T. Mason, J. Bibette, D. Weitz, Elasticity of compressed emulsions, Phys. Rev. Lett. 75(10) (1995) 2051. https://doi.org/10.1103/PhysRevLett.75.2051.

[48] H. Princen, A. Kiss, Rheology of foams and highly concentrated emulsions: III. Static shear modulus, J. Colloid Interface Sci. 112(2) (1986) 427-437. https://doi.org/10.1016/0021-9797(86)90111-6.

[49] I. Masalova, A.Y. Malkin, Rheology of highly concentrated emulsions-concentration and droplet size dependencies, Appl. Rheol. 17(4) (2007) 42250-1-42250-9. https://doi.org/10.1515/arh-2007-0011.

[50] T. Honorio, F. Masara, F. Benboudjema, Heat capacity, isothermal compressibility, isosteric heat of adsorption and thermal expansion of water confined in CSH, Cement 6 (2021) 100015. https://doi.org/10.1016/j.cement.2021.100015.

[51] D. Wong, A. Andriyana, B.C. Ang, J.J.L. Lee, E. Verron, M. Elma, Poisson's ratio and volume change accompanying deformation of randomly oriented electrospun nanofibrous membranes, Plastics, Plast. Rubber Compos. 48(10) (2019) 456-465. https://doi.org/10.1080/14658011.2019.1660838.

doi:10.6342/NTU202404382

## 2-6 Supporting Information

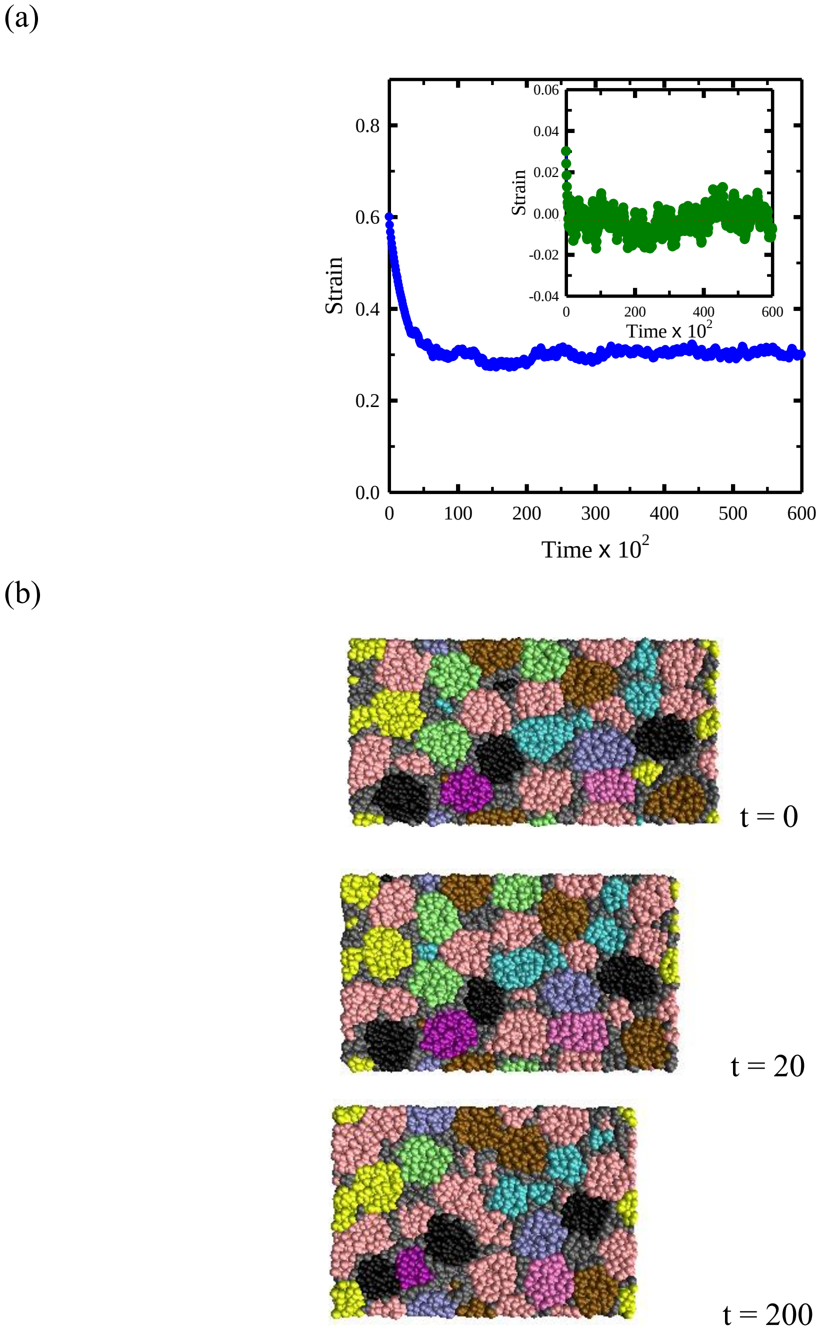

Figure 2-S1. (a) The relaxation process after stretching to a specific engineering strain. (b) The evolving snapshots of the concentrated emulsion for the initial strain 0.6. The initial elongation strain (t=0) was induced by the application of a stress. After removal of the applied stress, the system displayed the backward spring motion toward the initial position. For small elongation strain, the system can spring back to its initial position (elastic behavior), as shown in the inset. In contrast, for large elongation strain, it fails to recover the initial position (plastic behavior).

# Chapter 3 Abnormal wicking dynamics of total wetting ethanol in graphene nanochannels

## Abstract

Although the unexpectedly fast capillary flow of water (partial wetting) in graphene nanoslits has been reported, the wicking dynamics of total wetting liquid in a nanocapillary have not been studied. In this work, the spreading behavior on graphene sheets and the imbibition process in graphene nanochannels are explored by Molecular Dynamics for ethanol (total wetting). For spreading dynamics, two regimes are identified: inertia-dominated initial spreading and viscous spreading with an exponent greater than Tanner's law. For imbibition dynamics, the total wetting liquid behaves quite differently from the partial wetting liquid. The advancing motions of both the precursor film and main flow are clearly seen, and their advancing lengths are proportional to the square root of time. However, the proportional constant of the former which is independent of channel widths is greater than that of the latter which decreases with increasing channel widths. Both the thickness of the precursor film and the diameter of curvature of the menisci, which is less than the channel width, grow with increasing channel widths. For very narrow nanoslits, the precursor film cannot be distinguished from the main flow and the surprisingly rapid imbibition behavior is observed.

**Keywords:** nanocapillary flow, graphene nanochannels, total wetting, precursor film, spreading dynamic, imbibition dynamics.

## 3-1 Introduction

Spontaneous capillary flow describes the motion of a liquid imbibed into narrow spaces by negative capillary pressure without the assistance of external forces [1,2]. The negative capillary pressure is originated from the Laplace pressure across the concave meniscus [3]. The capillary flow can also be realized from the phenomenon of a liquid wetting the pores persistently, leading to the continuous decrease of surface free energy. Therefore, the spontaneous flow is driven by interfacial tensions, and it will not stop as long as the resistant force is not present or the pore end is not reached. However, in opposition to gravity, the capillary flow will cease at a certain height (Jurin height), known as capillary rise, because of the buildup of hydrostatic pressure [4]. This phenomenon is commonly seen in daily life and industrial applications, including brain capillary flow [5], microfluidic diagnostics [6], lab-on-a-chip devices [7,8], and fabrication of flexible printed electronics [9,10]. Since the early twentieth century, the physical mechanism associated with the capillary flow has been studied, but the capillarity in cylindrical tubes was focused [11-14]. Nonetheless, capillarity in micro- and nano-scale channels and in complex structures of narrow spaces have been an attractive subject of investigation nowadays [15].

The emergence of graphene and other 2D materials allows the fabrication of nanodevices which consist of artificial planar channels with widths close to a few molecular diameters [16]. Graphene has been extensively studied and may provide frictionless capillary channels owing to its smoothness of the surface and large specific surface area [15,17]. In fact, graphene-based membranes have been fabricated for water purification and they have a better performance of selectivity and permeability than polymer-based membranes [18-21]. Recently, nanocapillaries with atomic-scale precise channel width were constructed by graphene through van der Waals assembly [15,22]. The width of the nanoslit was lowered to only two layers of the graphene sheet. Unexpectedly fast capillary

doi:10.6342/NTU202404382

flow (about 1 m/s) of water was reported in narrow graphene slits [14,22-24]. It was attributed to high disjoining pressures and large slip lengths. Because of the structured arrangement of water molecules in nanoscale channels, the nano-confined liquid tends to exhibit distinctive characteristics [18]. That is, the physical and chemical properties of liquids under extreme nanoscale confinement can deviate from those of the bulk significantly, leading to anomalous mass transport behavior [16].

The wetting state of a liquid droplet on a solid substrate can be simply classified into partial and total wetting [25]. The former with different degrees of wetting (wettability) is always characterized by the contact angle $0° < \theta < 180°$ and the water droplet on graphene is an example [4,26,27]. In contrast, the latter is manifested by the continuous spreading behavior and corresponding to $\theta = 0°$ [28-30]. A typical example is an ethanol droplet on a glass slide [31]. According to Young's equation, a finite contact angle is the consequence of the balance among interfacial tensions [32]. However, the total wetting state can be further realized by the spreading coefficient defined as $S = \gamma_{sv} - \gamma_{sl} - \gamma_{lv}$ [33], where $\gamma_{sv}$, $\gamma_{sl}$, and $\gamma_{lv}$ represent solid-vapor, solid-liquid, and liquid-vapor tensions, respectively. While the partial wetting state is associated with $S < 0$, the total wetting state corresponds to $S \geq 0$, to which Young's equation fails to apply [34].

Until now, most of the studies of wicking dynamics in nanochannels involve spontaneous capillary flows of partial wetting liquids, such as molecular transport of water through graphene nanoslits [35-40]. However, a lot of liquids on graphene sheets exhibit total wetting behavior, including ethanol, dimethylformamide, and N-methyl-2-pyrrolidone [41-43]. Recently, penetration dynamics through hydrophilic nanocapillaries has been investigated by coarse-grained mesoscale simulations [34]. The breakdown of Washburn's equation is observed as the positive spreading coefficient is large enough.

doi:10.6342/NTU202404382

Moreover, on a wall extended infinitely outside the exit mouth of the nanoslit, the extended meniscus is limited by the edge effect or equilibrium contact angle for partial wetting liquids, but it can spread spontaneously for total wetting liquids. The latter is driven by the precursor film spreading and follows a power law. However, studies of real systems involving total wetting liquids are still lacking. In this work, the spreading behavior of the total wetting liquid (ethanol) on graphene sheets is studied first. Then the wicking process in graphene nanochannels is explored by Molecular Dynamics. The channel width ranges from two to ten layers of thickness of graphene sheets. The structural characteristics of the meniscus and precursor film are analyzed. The time evolutions of the main flow and precursor film are monitored. Finally, their dependence on the channel width is examined.

## 3-2 Method

Nanoscale Molecular Dynamics (NAMD) package is a parallel molecular dynamics [44,45] and is used for simulating the droplet wetting behavior and spontaneous capillary flow in this work. The free software VMD (Visual Molecular Dynamics) is adopted for making the initial configurations and for visualizing and analyzing the obtained simulation data [46]. The NAMD simulation was conducted out in the canonical (NVT) ensemble with the Langevin thermostat. The system was maintained at a temperature of 300 K.

The interatomic interaction between the molecules was calculated by the CHARMM force field for ethanol and graphene [47,48]. The pairwise van der Waals interaction between atoms was described by Lennard-Jones (L-J) 12-6 potential, and the cutoff distance is set at 12 Å with the pair list distance extended to 14 Å. The L-J parameters between different atoms are acquired by the Lorentz-Berthelot mixing rule [49,50]. The electrostatic interaction was calculated by the Coulomb potential, and the long-range effect was

doi:10.6342/NTU202404382

accounted for by the particle-mesh Ewald summation method [51]. All atoms of the graphene sheets were fixed in space during simulations. In experiments [22,26], the graphene walls are composed of numerous graphene layers, which allows them to be considered as rigid solid surfaces. The distance between two nearby carbon atoms in a graphene layer was 0.142 nm, and the interlayer distance was set to b = 0.335 nm. For both ethanol and graphene, the non-bonded parameters ($\varepsilon$ and $R_{min}$ of L-J) and charge (q) of each atom were listed in the Supporting Information **Table 3-S1(a)** and the bonded parameters were given in **Table 3-S1(b)**.

In this work, three simulation systems were considered: imbibition dynamics, interfacial tensions, and spreading dynamics. While the last will be described in Sec. 3.1, the imbibition system consists of a graphene nanoslit atop an ethanol reservoir, as shown in Figure 3-1. The reservoir was equilibrated at 300 K for 4 ns before the nanoslit was placed above it. To prevent the capillary flow took place along the outer walls of the nanoslit, a single graphene sheet acting as a baffle was placed atop the reservoir. The wall of the nanocapillary was constructed with three layers of graphene sheets. The width of the nanochannel (w) was $w = N \times b$, where N depicted the number of graphene sheets accommodated in the nanoslit. The total length of the nanocapillary along the z-direction was $L_z$ = 30 nm, and the box sizes in the x- and y-direction were $L_x$ = 16.75 nm and $L_y$ = 4.25 nm, subject to periodic boundary conditions. Both the penetration length describing the main capillary flow l(t) and the advancing front of the precursor film $l_p(t)$ were monitored during imbibition simulations.

doi:10.6342/NTU202404382

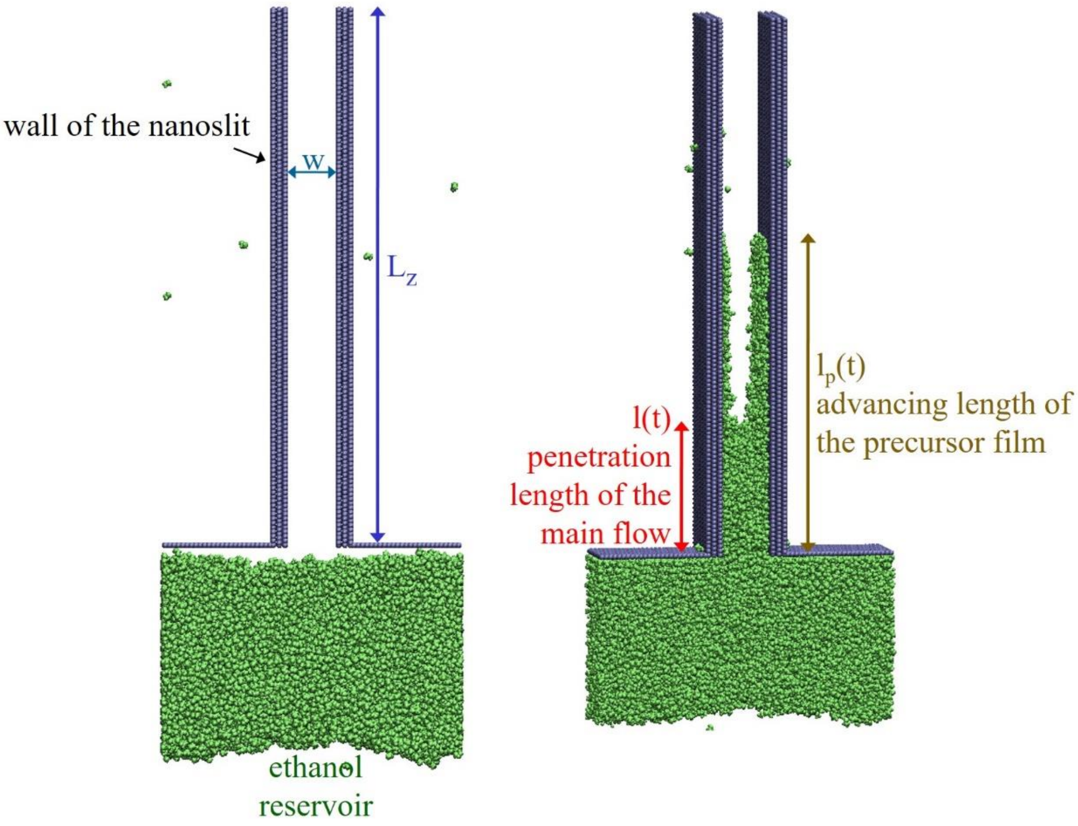

Figure 3-1. The schematic diagram for spontaneous capillary flow in a nanoslit atop the ethanol reservoir. The total length of the nanocapillary is $L_z$, and the width of the nanochannel is w.

To calculate the surface tension $\gamma_{lv}$ of ethanol, an ethanol liquid layer was placed in the middle of the simulation box, and the liquid-vapor interface was perpendicular to the z-direction. After reaching equilibrium in canonical ensemble simulation, the pressure tensor of the system was recorded. The surface tension $\gamma_{lv}$ was then calculated by Irving-Kirkwood expression $\gamma_{lv} = [p_{zz}-(p_{xx}+p_{yy})/2](L_z/2)$, where $p_{xx}$, $p_{yy}$, and $p_{zz}$ denote the diagonal components of the pressure tensor [52-54]. The factor of 1/2 associated with $L_z$ is due to the two surfaces in the system. The interfacial tensions $\gamma_{sv}$ - $\gamma_{sl}$ was estimated from the free energy perturbation theory in which the free energy difference between two states was evaluated based on a coupling parameter λ varying from 0 to 1 to connect the reference and perturbed states [55,56]. Consider a sheet of graphene placed in the middle of the system containing ethanol molecules. After obtaining the free energy difference (ΔF) between the two systems with and without ethanol-graphene interactions, $\gamma_{sv}$ - $\gamma_{sl}$ was determined by ΔF/(2A) where 2A denotes the solid-liquid interfacial area. The viscosity of ethanol was acquired from a fully equilibrated system according to the Green-Kubo formula, which uses the ensemble average of the auto-correlation of the pressure tensor [57,58].

## 3-3 Results and discussion

### 3-3-1 The total wetting behavior of ethanol on graphene

The wetting state which is responsible for driving capillarity, can be predicted from the interfacial tensions. By employing NAMD, the interfacial tensions of water on graphene at 25 °C were evaluated from the free energy perturbation method, $\gamma_{sv} - \gamma_{sl} = 15.7$ mN/m, and from the Irving-Kirkwood expression, $\gamma_{lv} = 66.9$ mN/m, giving the Young contact angle $\theta_Y = 76.4°$ [4]. The simulation results of $\gamma_{lv}$ and $\theta_Y$ agree reasonably with the experimental data [26]. Evidently, the water/graphene system has S = -51.2 mN/m < 0, corresponding to the partial wetting state. Following the same approach, the interfacial tensions of ethanol on graphene are calculated as $\gamma_{sv} - \gamma_{sl} = 80.4$ mN/m and $\gamma_{lv} = 24.1$ mN/m. The simulation outcome of $\gamma_{lv}$ is very close to the experimentally reported value of 22.3 mN/m [59]. Contrary to the water/graphene system, the spreading coefficient of the ethanol/graphene system is S = 56.4 mN/m > 0, predicting a total wetting state.

The wetting behavior of an ethanol droplet on the graphene surface can be directly observed by the dynamics after the deposition of a nanodroplet. The ethanol droplet was equilibrated at 300 K for 3 ns and then placed almost in contact with the graphene substrate, which contains three layers of graphene sheets. The spreading process is illustrated

doi:10.6342/NTU202404382

in Figure 3-2 (both side and top views) by a series of snapshots from 0 to 1.2 ns. As expected, the height of the droplet from the side view decreases gradually with time, and the wetted area from the top view grows accordingly. The apparent contact angle decays continuously but never reaches an equilibrium value. In fact, the nanodroplet becomes essentially flattened at 1.2 ns. This spontaneous spreading behavior indicates the absence of a finite equilibrium contact angle and corresponds to a total wetting state. This observation is consistent with the prediction of a positive spreading coefficient mentioned above.

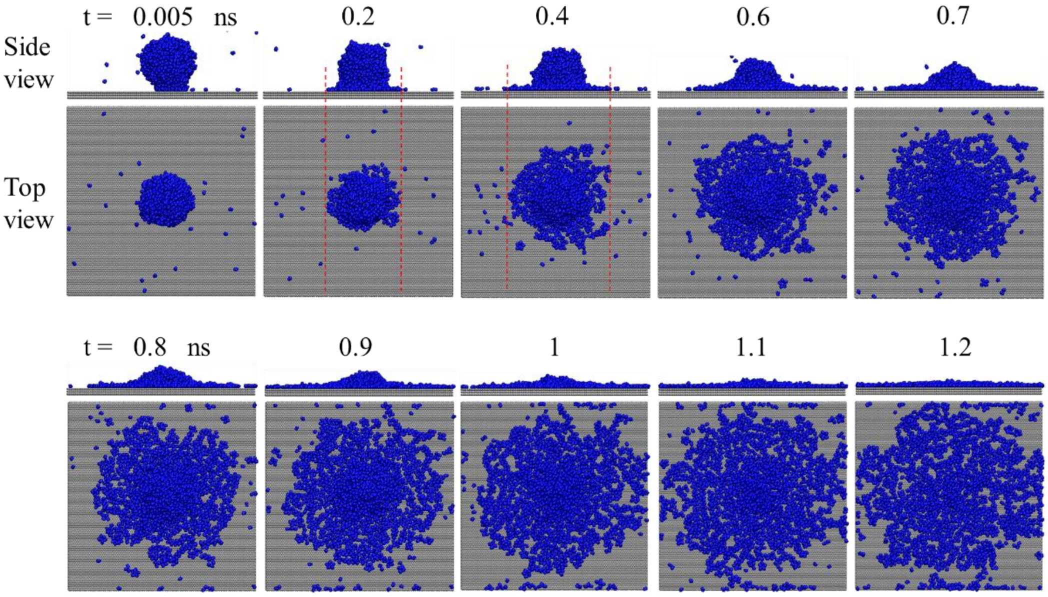

Figure 3-2. A series of snapshots (side and top views) of an ethanol nanodroplet deposited on graphene at different time periods.

The initial spreading stage of a droplet which starts at a radius r = 0 upon contact, is generally very fast for low-viscosity liquids [60], regardless of surface wettability. The characteristic inertio-capillary time scale is $t_c=(\rho R^3/\gamma_{lv})^{1/2}$, where $\rho$ denotes the liquid density and R the initial radius of the droplet. In the inertial regime, the contact radius (r) or wetted area (A) grows with time, which follows the power law $r \sim t^{1/2}$ or $A \sim t$ [60,61]. On a total wetting surface, the expanding process of the droplet continues indefinitely, and the spreading dynamics in the long time limit can also be depicted by the power law $r \sim t^m$ or $A \sim t^{2m}$. The balance between capillary and viscous forces gives the exponent m = 1/10, known as Tanner's law [60,62,63]. By the plot of log(A) against log(t), Figure 3-3 shows the spreading behavior of a nanodroplet of ethanol deposited on graphene for three different sizes of droplets. These droplets exhibit similar behaviors, with two distinct regimes clearly identified. The first regime ($t < 0.4$ ns) has a unity slope (2m = 1), revealing the inertia-dominated initial spreading. The inertio-capillary time is about $t_c = 0.03 \sim 0.05$ ns for an ethanol nanodroplet with $R = 4.1 \sim 5.7$ nm. It is consistent with our simulation observation of the early spreading process. The transition from the first to the second regime is accompanied by the emergence of the precursor film. In contrast, the second regime ($t > 0.4$ ns) has a slope of about 2m = 0.5, which is significantly greater than the exponent of Tanner's law. The deviation may be attributed to our definition that the precursor film is included in the wetted area based on the top view. As the precursor film is considered, it has been reported that the exponent of the power law exceeds 2m = 0.4 significantly and grows with the spreading coefficient [64].

doi:10.6342/NTU202404382

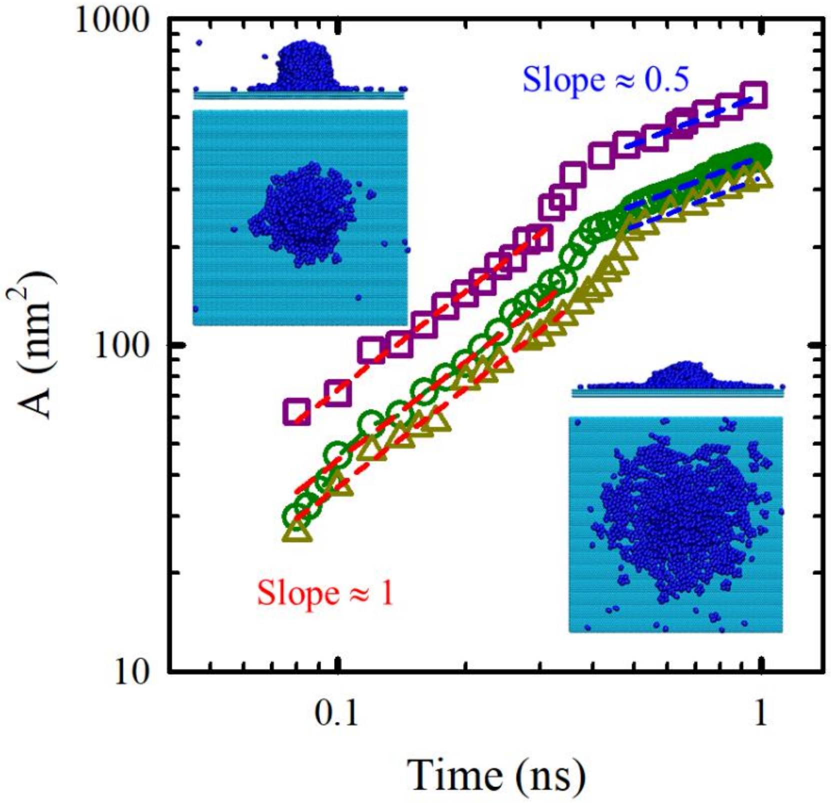

Figure 3-3. The variation of wetted area (A) with time (t) for three different sizes of droplets. The snapshots denote the top and side views for the two spreading behaviors of R = 4.9 nm.

## 3-3-2 Meniscus and precursor film

As the graphene nanochannel with two parallel walls is placed atop a reservoir of ethanol at thermodynamic equilibrium, spontaneous imbibition appears, and the capillary flow can be monitored. Both the meniscus in the nanoslit and the bottom of the reservoir are exposed to the vapor phase of ethanol. The typical snapshots of the capillary flow at different time periods are shown in Figure 3-4 for the channel width N = 8. As expected, the penetration length (l) defined by the meniscus bottom surface grows progressively with time, as illustrated in Figure 3-4(a). Indeed, the capillary flow stops as the meniscus

doi:10.6342/NTU202404382

reaches the end of the channel (at t ≈ 11 ns). According to the side view, however, a thin liquid film ahead of the meniscus is clearly observed on the wall. To examine the feature of the thin film, the front views, which look from the channel center toward the wall (corresponding to their halves of the side views), are depicted in Figure 3-4(b). It is interesting to find that the thin film covers the wall essentially, and the film length is actually increased with time. This abnormal observation is different from the typical menisci associated with the capillary flow, and it can be considered as the precursor film accompanied with the spreading behavior of a droplet of total wetting liquid on a substrate, as observed in Sec. 3.1. Note that total wetting is characterized by the continuous spreading of the droplet, with the precursor front identified by a zero contact angle.

Evidently, the front structure of the imbibed liquid for total wetting ethanol differs distinctly from that for partial wetting liquids such as water. That is, there exists a significant difference between their advancing menisci which are generally characterized by the dynamic contact angle ($\theta_D$) and radius of curvature (R). For partial wetting liquids, the dynamic contact angle is finite ($\theta_D > 0°$), and thus the diameter of curvature (2R) must exceed the channel width (w). In contrast, for total wetting liquids, the equilibrium contact angle is essentially zero, which corresponds to the condition of 2R = w. Under nonequilibrium flow, the dynamic contact angle is always greater than the equilibrium contact angle because of the contribution of the dynamic pressure. In this simulation, it is somewhat surprising to observe that the diameter of curvature is less than the channel width, and the dynamic contact angle is indeed zero.

doi:10.6342/NTU202404382

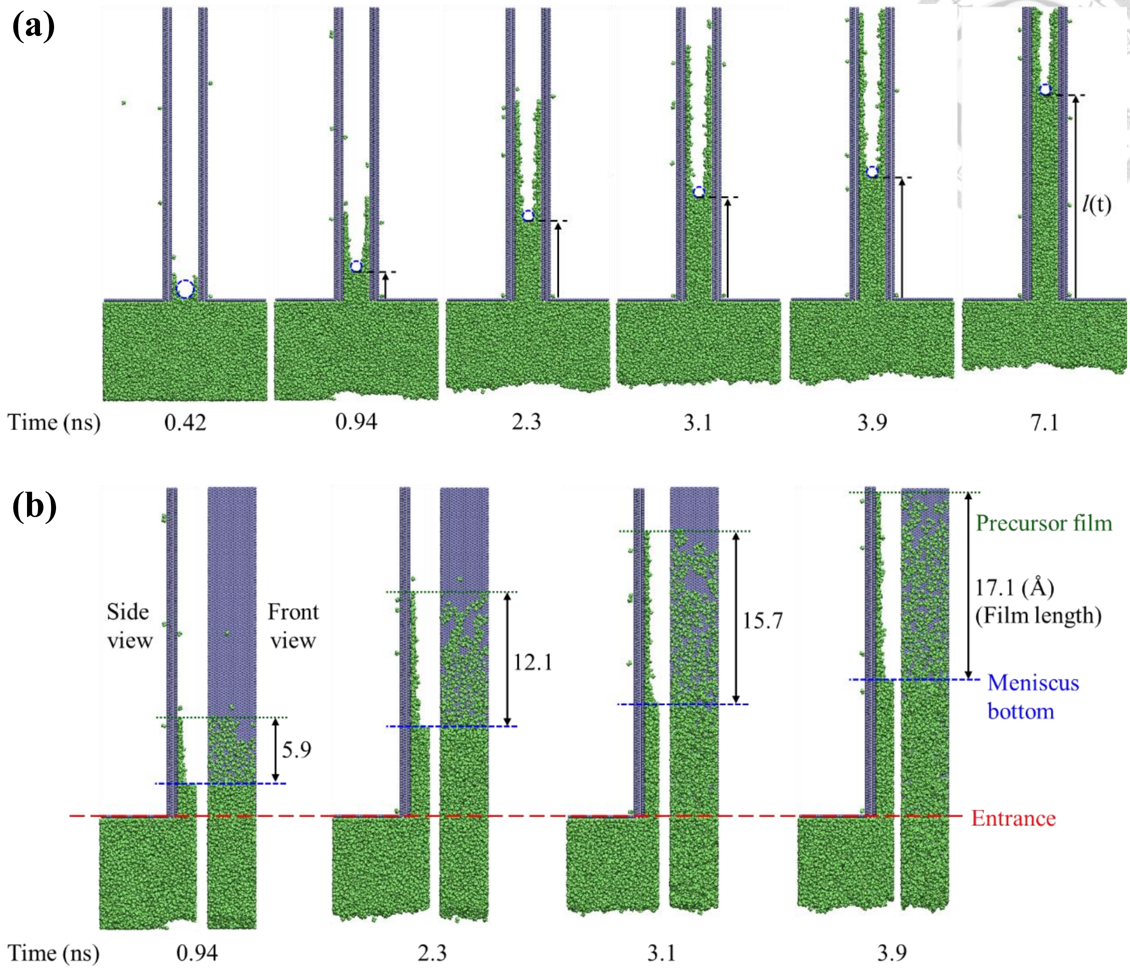

Figure 3-4. Snapshots of the wicking process of ethanol through a nanoslit with N = 8, (a) full side views and (b) halves of side views and their corresponding front views.

The imbibition dynamics is closely related to the advancing meniscus, which is characterized by the radius of curvature. As a result, the evolution of the meniscus shape is monitored and shown in Figure 3-5. The magnified images of the menisci at different times are depicted in the insets of Figure 3-5. It is found that the radius of the curvature (R) decreases rapidly near the entrance but approaches a constant eventually (platform stage with a steady curvature radius). It drops from about 14.6 Å at 0.1 ns to 7.4 Å at 0.5 ns and remains unchanged (R = 7.4 Å) later, revealing that a steady meniscus of the liquid front is obtained. The thickness of the precursor film ($t_p$) in the proximity of the meniscus can be well described by $t_p = (w - 2R)/2$. That is, the film thickness grows from 0 to 6.0 Å, corresponding to 0 ~ 2.1 ethanol layer. Apparently, the initial shrinkage of the radius of curvature characterizing the meniscus is caused by the development of the precursor film accompanied with the earlier imbibition process.

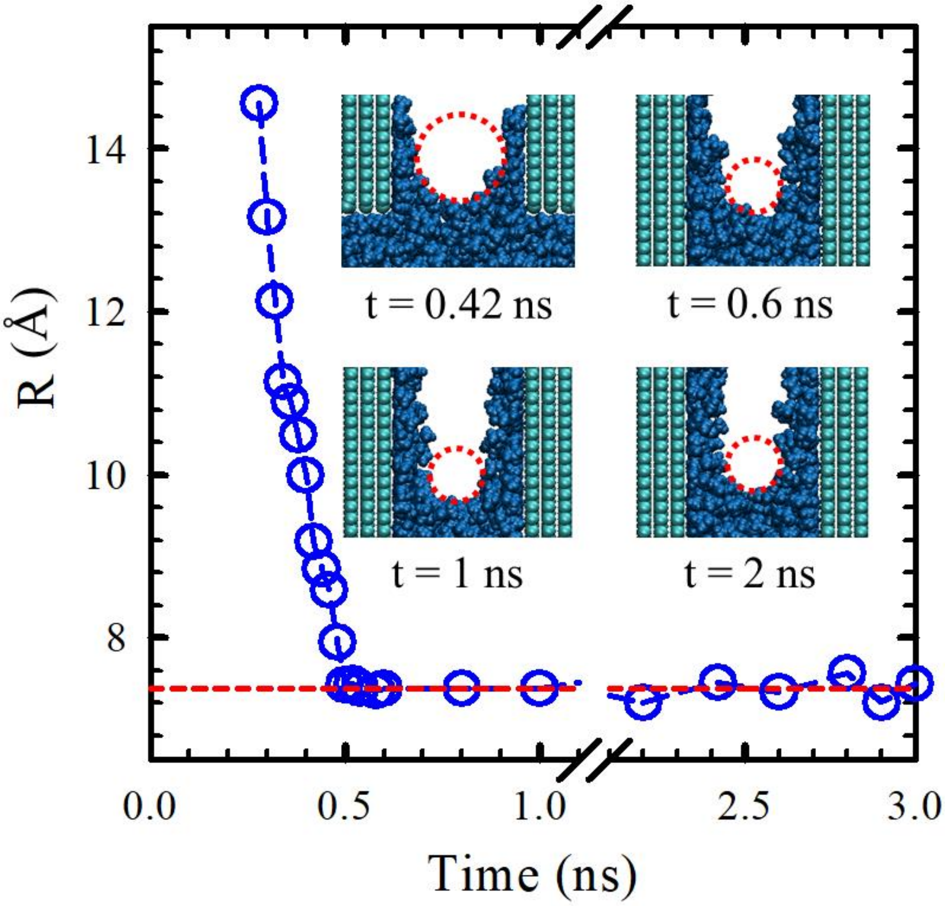

Figure 3-5. The time evolution of the radius of curvature of the advancing meniscus for N = 8. Some enlarged images of the advancing meniscus are shown in the inset.

For partial wetting liquids, it is known that the radius of curvature (R) of the advancing meniscus is inversely proportional to the channel width (w) [4]. However, for total wetting liquids, the R-w relationship is no longer valid because of the appearance of the precursor film. Figure 3-6(a) shows magnified images of advancing menisci away from the capillary entrance for different channel widths. For the channel widths N = 2 and 3

doi:10.6342/NTU202404382

which are comparable to the molecular size, the meniscus shape is difficult to characterize, and the precursor film is not seen. In fact, one is unable to distinguish the meniscus from the precursor film for such narrow nanochannels. For $N \geq 4$, the radius of curvature of the advancing meniscus can be measured, and it grows with increasing the channel width. If the thickness of the precursor film does not change with the channel width, one expects that the radius curvature is proportional to the channel width, $R \sim w$. As illustrated in the inset of Figure 3-6(b), the thickness of the precursor film actually increases from 3.4 to 8.2 Å as the channel width increases. Figure 3-6(b) also shows that the steady radius curvature in the platform stage rises approximately linearly with increasing N. Certainly, the condition of $2(R + t_p) = w$ is satisfied. Evidently, the features of the advancing meniscus for total wetting liquids are distinctly different from those for partial wetting liquids during the imbibition process.

**(a)**

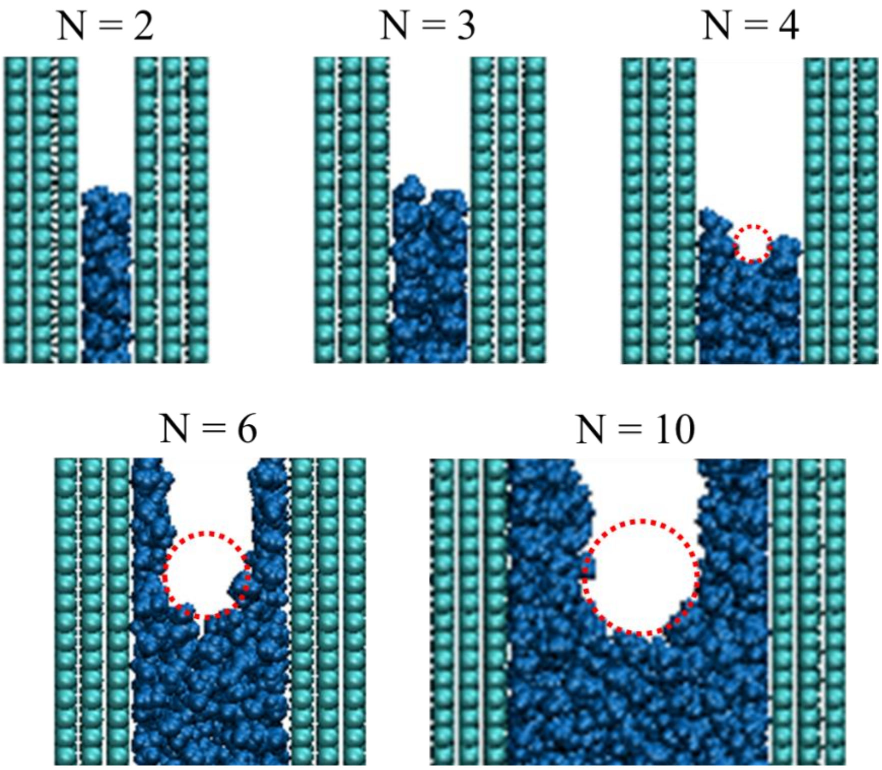

doi:10.6342/NTU202404382

**(b)**

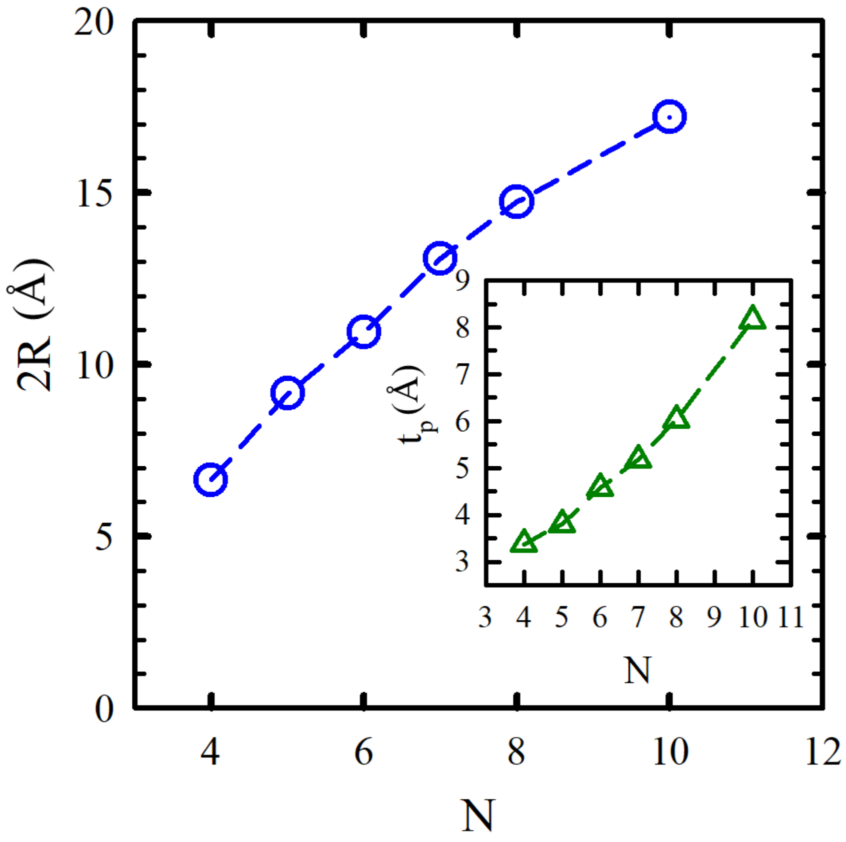

Figure 3-6. (a) Magnified images of advancing menisci for different nanochannel widths, N = 2, 3, 4, 6, and 10. The red dotted line denotes the circle associated with the radius of curvature. (b) The variation of the diameter of curvature (2R) with the nanochannel widths (N). The plot of the thickness of the precursor film ($t_p$) against the channel width (N) is shown in the inset.

### 3-3-3 Imbibition dynamics

The imbibition dynamics is often described by Washburn's equation [4,65,66], which gives the variation of the penetration length (l) with time, $l^2 = \alpha t$ with $\alpha = [\gamma_{lg}\cos(\theta_D)/(3\mu)](w+6l_s)$ [67]. Here $\mu$ represents the viscosity, $\theta_D$ the dynamic contact angle, and $l_s$ the slip length. The condition of $l_s = 0$ corresponds to the no-slip boundary condition. The penetration length is generally defined as the distance of the advancing meniscus from

doi:10.6342/NTU202404382

the entrance. Figure 3-7(a) shows the time evolution of the lowest position of the advancing meniscus of ethanol in the graphene nanocapillaries with different channel widths. The channel height ($L_z = 30$ nm) is sufficiently long to observe the capillary motion before the spontaneous flow is halted by the end of the nanoslit. The results of the linear relationship between $l^2$ and t (besides the entrance region) are consistent with Washburn's equation. However, the slope $\alpha$ corresponding to the imbibition rate is found to decay with increasing the channel width w. This result is contradictory to the prediction of Washburn's equation, $\alpha \sim w$ as $l_s = 0$.

Following the relationship $l^2 = \alpha t$, one is able to calculate the imbibition velocity ($v_z = dl/dt$) and flow rate ($Q = wdv_z$) of ethanol transport at a specific penetration length $l = 1$ μm and depth $d = 130$ nm, which was used for the study of water transport in graphene nanoslits.[4] As illustrated in Figure 3-7(b) which were obtained based on the data presented in Figure 3-7(a), the imbibition velocity seems to decrease linearly, and the flow rate grows weakly as the channel width N is increased. Certainly, these results do not agree with Washburn's equation ($v_z \sim N$ and $Q \sim N^2$ ). This dependence of $v_z$ on the channel width ($N = 2 \sim 5$) of ethanol transport is qualitatively similar to that of water transport. However, the imbibition velocity of ethanol is significantly greater than that of water. For example, for $N = 3$, $v_z = 3.94$ m/s at $l = 75$ nm and 0.07 m/s at $l = 4$ μm for ethanol, but $v_z = 1.05$ m/s and 0.02 m/s respectively for water. From the resistance to the fluid flow, ethanol has a viscosity (simulation value $\mu = 0.95$ mPa·s) slightly higher than water ($\mu = 0.855$ mPa·s). On the contrary, from the viewpoint of the driving force, ethanol has much better surface wettability ($\theta_D \sim 0°$ or $\gamma_{sv} - \gamma_{sl} = 80.4$ mN/m) than water ($\theta_D \sim 90°$ or $\gamma_{sv} - \gamma_{sl} = 15.7$ mN/m). As a result, it is not surprising that ethanol has a higher imbibition rate than water in graphene nanoslits.

doi:10.6342/NTU202404382

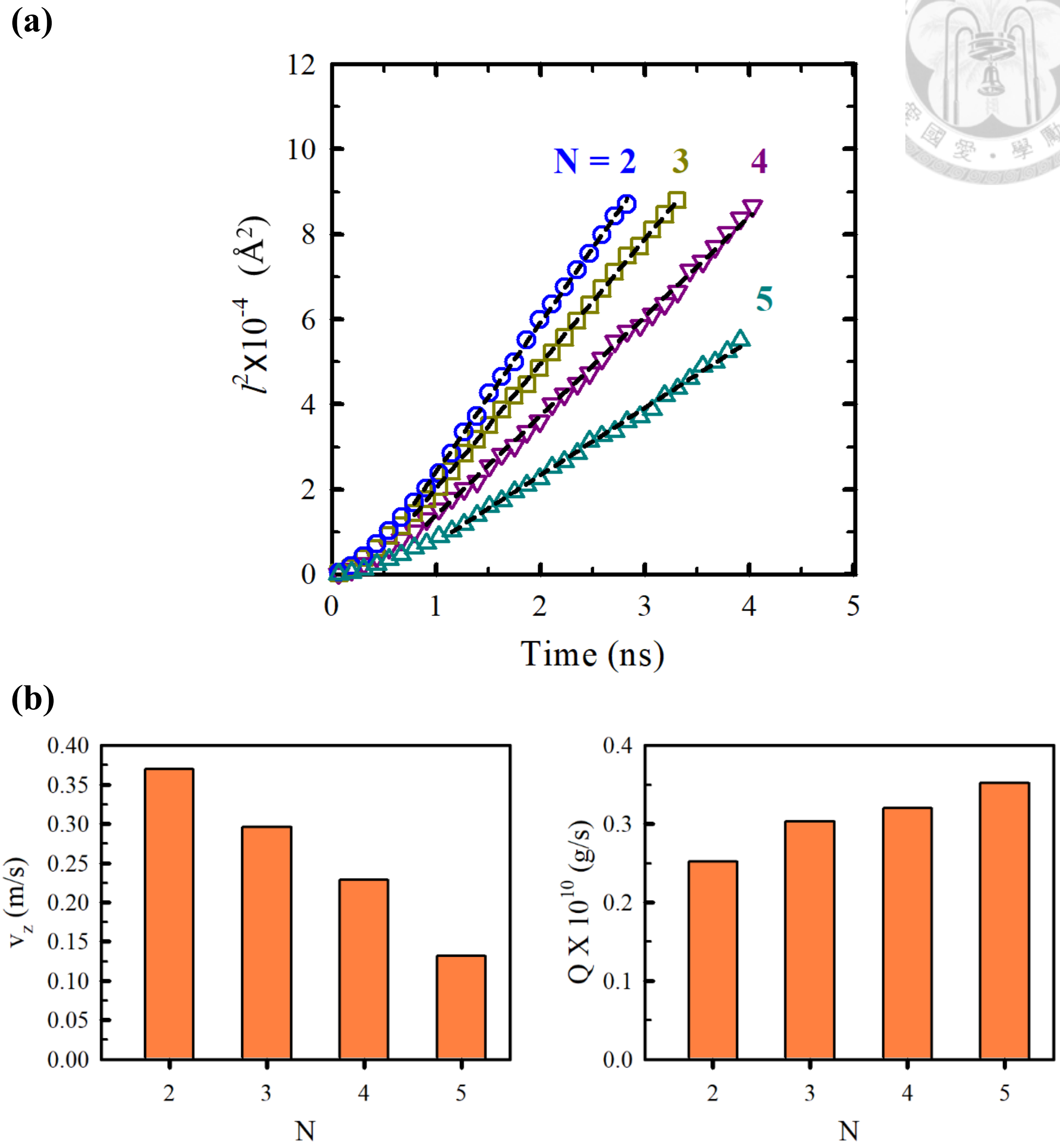

Figure 3-7. (a) The square of the penetration length $l^2$ versus time for different graphene channel widths. (b) Effects of the channel width on the imbibition velocity $v_z$ and flow rate Q of ethanol at the penetration length l = 1 μm and the depth of d = 130 nm.

Different from water (partial wetting) wicking, the imbibition dynamics of ethanol (total wetting) for N ≥ 5 involves the advances of both main capillary flow and precursor film, which are represented by l(t) and $l_p$(t), respectively. Figure 3-8(a) shows the variation of $l^2$ and $l_p^2$ with time in graphene nanoslits with N = 5 and 6. Similar to the behavior of the penetration length ($l^2 = \alpha t$), it is found that $l_p^2$ is also proportional to the wicking time ($l_p^2 = \beta t$). The deviation is observed because the front of the precursor film is near the entrance ($t < 0.5$ ns) and reaches the exit ($t > 4$ ns). The advancing rate of the precursor film is greater than that of the main flow ($\beta > \alpha$), and the distance between those two fronts grows with time. The comparison between N = 5 and 6 reveals that ($l_p^2$ - $l^2$) is affected by the channel width. In fact, the difference of the advancing rate ($\beta$ - $\alpha$) is found to rise with increasing the channel width.

According to Figure 3-7, the imbibition rate of the main capillary flow ($\alpha$) depends on the channel width, and $v_z$ decreases with increasing N. The effect of the channel width on the advancing rate of the precursor film is shown in Figure 3-8(b) for N = 6-10. Contrary to the main flow, all the curves of $l_p^2$ versus t are collapsed together, and they all reach the top of the nanocapillary at about 4 ns. This consequence indicates that the advancing rate of the precursor film is essentially independent of the channel width and $\beta$ is a constant. The growth of ($\beta$ - $\alpha$) with N is actually due to the decrement of $\alpha$ with the channel width for N = 5-10. It is worth emphasizing that for small channel widths (N = 2-4), the precursor film is difficult to be distinguished from the main capillary flow, as demonstrated in Figure 3-6(a). As a result, the curves of $l^2$ vs t for N = 2-4 in Figure 3-7(a) can be considered as $l_p^2$ vs t, i.e., $\beta = \alpha$. Evidently, one has $\beta(N = 2) > \beta(N = 3) > \beta(N = 4) \approx \beta(N = 5)$. The reason that $\beta$ is no longer a constant but grows with decreasing N is the overlap of the precursor films on the two walls for small channel widths. The synergetic effect leads to an advancing rate of the overlapped precursor film faster than that of the isolated precursor film. As N is increased, the contribution of the rapidly moving precursor film to the imbibition dynamic declines, resulting in a decrease in the imbibition velocity. This phenomenon may explain the decay of $v_z$ with N, which is contradictory to the prediction of Washburn’s equation.

doi:10.6342/NTU202404382

**(a)**

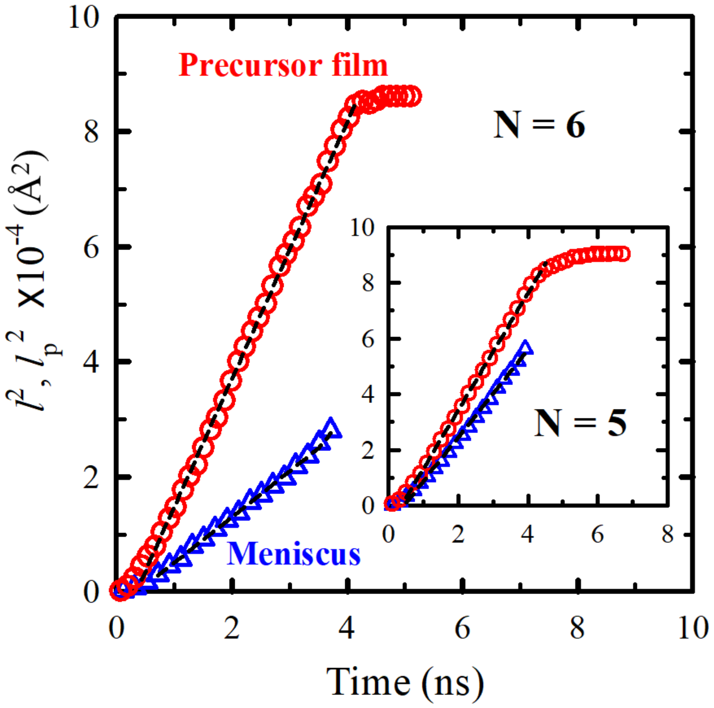

**(b)**

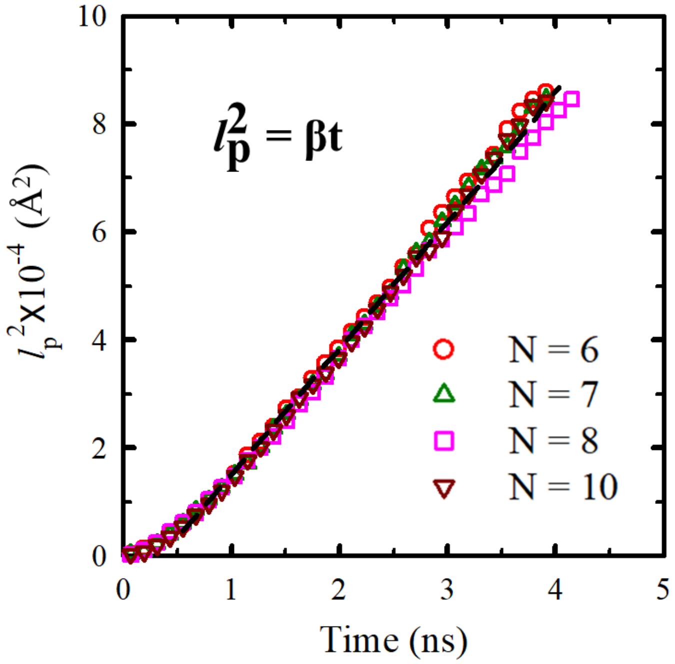

Figure 3-8. (a) The square of the advancing length of the precursor film ($l_p^2$) and of the penetration length of the main flow ($l^2$) are plotted against time for N = 5 and 6. (b) The square of the advancing length of the precursor film against time for N = 6 ~10.

doi:10.6342/NTU202404382

## 3-4 Conclusion

The spreading behavior on graphene sheets and the wicking process in graphene nanochannels are explored by MD for the total wetting ethanol. After the deposition of an ethanol nanodroplet, it spreads continuously and becomes an adsorbed monolayer eventually, indicating the total wetting behavior. This outcome is consistent with the positive spreading coefficient obtained from interfacial tensions, which are calculated by MD. For spreading dynamics, two regimes can be identified from the time evolution of the wetted area. A unit slope is acquired in the first regime, revealing an inertia-dominated initial spreading. However, the slope of the second regime is significantly larger than the exponent of Tanner's law because the precursor film is included in the wetted area.

The imbibition characteristics of the total wetting liquid (e.g., ethanol) are found to be quite different from those of the partial wetting liquid (e.g., water). For small channel widths ($N = 2\sim4$), the precursor film of the total wetting ethanol is difficult to be distinguished from the main capillary flow. In contrast, for large channel width ($N \geq 5$), the precursor film is clearly observed during the wicking process, and thus the dynamic contact angle associated with the advancing meniscus is zero. As a result, the diameter of the curvature of the meniscus is less than the width of the nanoslit. As the channel width rises, both the thickness of the precursor film and the radius of curvature of the advancing meniscus are increased.

The time dependence of the penetration length of the main capillary flow can be described by $l^2 = \alpha t$, similar to Washburn's equation, but the imbibition rate ($\alpha$) decreases with increasing the channel width, contrary to the prediction of Washburn's equation. The advancing of the precursor film can also be depicted by $l_p{}^2 = \beta t$ with $\beta > \alpha$, but its advancing rate ($\beta$) is essentially independent of the channel width. For small channel widths ($N \leq 3$), the overlap of the precursor films on the two walls yields a surprisingly rapid

doi:10.6342/NTU202404382

imbibition behavior.

## 3-5 Reference

[1] J. Cai, T. Jin, J. Kou, S. Zou, J. Xiao, Q. Meng, Lucas-Washburn equation-based modeling of capillary-driven flow in porous systems, Langmuir 37 (2021) 1623.

[2] P. Kolliopoulos, S. Kumar, Capillary flow of liquids in open microchannels: overview and recent advances, npj Microgravity 7 (2021) 51.

[3] H. Mehrabian, P. Gao, J. J. Feng, Wicking flow through microchannels, Phys. Fluids 23 (2011) 122108.

[4] T.-Y. Wang, H.-Y. Chang, G.-Y. He, H.-K. Tsao, Y.-J. Sheng, Anomalous spontaneous capillary flow of water through graphene nanoslits: Channel width-dependent density, J. Mol. Liq. 352 (2022) 118701.

[5] A.-A. Berthiaume, F. Schmid, S. Stamenkovic, V. Coelho-Santos, C. D. Nielson, B. Weber, M. W. Majesky, A. Y. Shih, Pericyte remodeling is deficient in the aged brain and contributes to impaired capillary flow and structure, Nat. Commun. 13 (2022) 5912.

[6] D. Shou, J. Fan, Design of nanofibrous and microfibrous channels for fast capillary flow, Langmuir 34 (2018) 1235.

[7] A. Olanrewaju, M. Beaugrand, M. Yafia, D. Juncker, Capillary microfluidics in microchannels: from microfluidic networks to capillaric circuits, Lab Chip 18 (2018) 2323.

[8] J. Park, D. H. Han, J.-K. Park, Towards practical sample preparation in point-of-care testing: user-friendly microfluidic devices, Lab Chip 20 (2020) 1191.

[9] M. Cao, K. Jochem, W. J. Hyun, L. F. Francis, C. D. Frisbie, Self-aligned inkjet printing of resistors and low-pass resistor-capacitor filters on roll-to-roll imprinted

doi:10.6342/NTU202404382

plastics with resistances ranging from 10 to 106 Ω, Flex. Print. Electron. 3 (2018) 045003.

[10] K. S. Jochem, W. J. Suszynski, C. D. Frisbie, L. F. Francis, High-resolution, high-aspect-ratio printed and plated metal conductors utilizing roll-to-roll microscale UV imprinting with prototype imprinting stamps, Ind. Eng. Chem. Res. 57 (2018) 16335.

[11] R. J. Mashl, S. Joseph, N. Aluru, E. Jakobsson, Anomalously immobilized water: a new water phase induced by confinement in nanotubes, Nano Lett. 3 (2003) 589.

[12] E. Dujardin, T. Ebbesen, H. Hiura, K. Tanigaki, Capillarity and wetting of carbon nanotubes, Science 265 (1994) 1850.

[13] K. Koga, G. Gao, H. Tanaka, X. C. Zeng, Formation of ordered ice nanotubes inside carbon nanotubes, Nature 412 (2001) 802.

[14] G. Hummer, J. Rasaiah, J. Noworyta, Nanoscale hydrodynamics: enhanced flow in carbon nanotubes, Nature 414 (2001) 188.

[15] Y.-T. Cheng, H.-Y. Chang, H.-K. Tsao, Y.-J. Sheng, Imbibition dynamics and steady flows in graphene nanochannels with sparse geometric and chemical defects, Phys. Fluids 34 (2022) 112003.

[16] C. D. Williams, Z. Wei, M. R. bin Shaharudin, P. Carbone, A molecular simulation study into the stability of hydrated graphene nanochannels used in nanofluidics devices, Nanoscale 14 (2022) 3467.

[17] G. Salussolia, C. Kamal, J. Stafford, N. Pugno, L. Botto, Simulation of interacting elastic sheets in shear flow: Insights into buckling, sliding, and reassembly of graphene nanosheets in sheared liquids, Phys. Fluids 34 (2022) 053311.

[18] Z. Zhao, C. Sun, R. Zhou, Thermal conductivity of confined-water in graphene nanochannels, Int. J. Heat Mass Transf. 152 (2020) 119502.

[19] K. Gopinadhan, S. Hu, A. Esfandiar, M. Lozada-Hidalgo, F. Wang, Q. Yang, A.

doi:10.6342/NTU202404382

Tyurnina, A. Keerthi, B. Radha, A. Geim, Complete steric exclusion of ions and proton transport through confined monolayer water, Science 363 (2019) 145.

[20] R. Nair, H. Wu, P. N. Jayaram, I. V. Grigorieva, A. Geim, Unimpeded permeation of water through helium-leak-tight graphene-based membranes, Science 335 (2012) 442.

[21] C. Sun, M. Liu, B. Bai, Molecular simulations on graphene-based membranes, Carbon 153 (2019) 481.

[22] B. Radha, A. Esfandiar, F. Wang, A. Rooney, K. Gopinadhan, A. Keerthi, A. Mishchenko, A. Janardanan, P. Blake, L. Fumagalli, Molecular transport through capillaries made with atomic-scale precision, Nature 538 (2016) 222.

[23] G. Hummer, J. C. Rasaiah, J. P. Noworyta, Water conduction through the hydrophobic channel of a carbon nanotube, Nature 414 (2001) 188.

[24] J. K. Holt, H. G. Park, Y. Wang, M. Stadermann, A. B. Artyukhin, C. P. Grigoropoulos, A. Noy, O. Bakajin, Fast mass transport through sub-2-nanometer carbon nanotubes, Science 312 (2006) 1034.

[25] J. Y. Lu, Q. Ge, H. Li, A. Raza, T. Zhang, Direct prediction of calcite surface wettability with first-principles quantum simulation, J. Phys. Chem. Lett. 8 (2017) 5309.

[26] A. Kozbial, C. Trouba, H. Liu, L. Li, Characterization of the intrinsic water wettability of graphite using contact angle measurements: Effect of defects on static and dynamic contact angles, Langmuir 33 (2017) 959.

[27] J. Włoch, A. P. Terzyk, P. Kowalczyk, New forcefield for water nanodroplet on a graphene surface, Chem. Phys. Lett. 674 (2017) 98.

[28] Y. Xu, C. J. Dibble, N. G. Petrik, R. S. Smith, B. D. Kay, G. A. Kimmel, Complete wetting of Pt (111) by nanoscale liquid water films, J. Phys. Chem. Lett. 7 (2016)

doi:10.6342/NTU202404382

541.

[29] M. F. Pucci, B. Duchemin, M. Gomina, J. Bréard, Dynamic wetting of molten polymers on cellulosic substrates: model prediction for total and partial wetting, Front. Mater. 7 (2020) 143.

[30] M. E. Diaz, M. D. Savage, R. L. Cerro, The effect of temperature on contact angles and wetting transitions for n-alkanes on PTFE, J. Colloid Interface Sci. 503 (2017) 159.

[31] V. Madhurima, J. Lalnunsiama, Concentration dependent wetting by aniline-ethanol binary system, Mediterr. J. Chem. 2 (2012) 365.

[32] C.-C. Chang, Y.-J. Sheng, H.-K. Tsao, Wetting hysteresis of nanodrops on nanorough surfaces, Phys. Rev. E 94 (2016) 042807.

[33] K.-C. Chu, H.-K. Tsao, Y.-J. Sheng, Spontaneous spreading of nanodroplets on partially wetting surfaces with continuous grooves: Synergy of imbibition and capillary condensation, J. Mol. Liq. 339 (2021) 117270.

[34] K.-C. Chu, H.-K. Tsao, Y.-J. Sheng, Penetration dynamics through nanometer-scale hydrophilic capillaries: Beyond Washburn’s equation and extended menisci, J. Colloid Interface Sci. 538 (2019) 340.

[35] W. Xiong, J. Z. Liu, M. Ma, Z. Xu, J. Sheridan, Q. Zheng, Strain engineering water transport in graphene nanochannels, Phys. Rev. E 84 (2011) 056329.

[36] J. Su, H. Guo, Effect of nanochannel dimension on the transport of water molecules, J. Phys. Chem. B 116 (2012) 5925.

[37] E. Wagemann, E. Oyarzua, J. H. Walther, H. A. Zambrano, Slip divergence of water flow in graphene nanochannels: the role of chirality, Phys. Chem. Chem. Phys. 19 (2017) 8646.

[38] A. T. Celebi, C. T. Nguyen, R. Hartkamp, A. Beskok, The role of water models on

doi:10.6342/NTU202404382

the prediction of slip length of water in graphene nanochannels, J. Chem. Phys. 151 (2019) 174705.

[39] M. Kargar, A. Lohrasebi, Water flow modeling through a graphene-based nanochannel: Theory and simulation, Phys. Chem. Chem. Phys. 21 (2019) 3304.

[40] L. Yang, Y. Guo, Dynamics of water confined in a graphene nanochannel: dependence of friction on graphene chirality, Nanotechnology 31 (2020) 235702.

[41] A. K. Metya, S. Khan, J. K. Singh, Wetting transition of the ethanol-water droplet on smooth and textured surfaces, J. Phys. Chem. C 118 (2014) 4113.

[42] W. Dilokekunakul, S. Chaemchuen, N. Klomkliang, Molecular Insights into the Effect of Temperature and Functional Groups on the Nonwetting, Prewetting, Partial Wetting, and Complete Wetting Transitions of Ethanol on Graphite, Ind. Eng. Chem. Res. 60 (2021) 13040.

[43] E. Bordes, L. Douce, E. L. Quitevis, A. A. Pádua, M. Costa Gomes, Ionic liquids at the surface of graphite: Wettability and structure, J. Chem. Phys. 148 (2018) 193840.

[44] J. C. Phillips, R. Braun, W. Wang, J. Gumbart, E. Tajkhorshid, E. Villa, C. Chipot, R. D. Skeel, L. Kale, K. Schulten, Scalable molecular dynamics with NAMD, J. Comput. Chem. 26 (2005) 1781.

[45] J. C. Phillips, D. J. Hardy, J. D. Maia, J. E. Stone, J. V. Ribeiro, R. C. Bernardi, R. Buch, G. Fiorin, J. Hénin, W. Jiang, Scalable molecular dynamics on CPU and GPU architectures with NAMD, J. Chem. Phys. 153 (2020) 044130.

[46] W. Humphrey, A. Dalke, K. Schulten, VMD: visual molecular dynamics, J. Mol. Graph. 14 (1996) 33.

[47] S. A. Deshmukh, G. Kamath, S. K. Sankaranarayanan, Comparison of the interfacial dynamics of water sandwiched between static and free-standing fully flexible graphene sheets, Soft Matter 10 (2014) 4067.

doi:10.6342/NTU202404382

[48] K. Vanommeslaeghe, E. Hatcher, C. Acharya, S. Kundu, S. Zhong, J. Shim, E. Darian, O. Guvench, P. Lopes, I. Vorobyov, CHARMM general force field: A force field for drug-like molecules compatible with the CHARMM all-atom additive biological force fields, J. Comput. Chem. 31 (2010) 671.

[49] D. Mohammad-Aghaie, M. M. Papari, J. Moghadasi, B. Haghighi, Assessment of the effect of mixing rules on transport properties of gas mixtures, Bull. Chem. Soc. Jpn. 81 (2008) 1219.

[50] Q. Guan, B. Shan, R. Wang, G. Feng, Z. Guo, Evaluation of different particle-actuation modes in molecular dynamics and their impact on nanoscale flow behaviors, Phys. Fluids 34 (2022) 072006.

[51] U. Essmann, L. Perera, M. L. Berkowitz, T. Darden, H. Lee, L. G. Pedersen, A smooth particle mesh Ewald method, J. Chem. Phys. 103 (1995) 8577.

[52] J. Irving, J. G. Kirkwood, The statistical mechanical theory of transport processes. IV. The equations of hydrodynamics, J. Chem. Phys. 18 (1950) 817.

[53] J. G. Kirkwood, F. P. Buff, The statistical mechanical theory of surface tension, J. Chem. Phys. 17 (1949) 338.

[54] M. T. Hossain, I. D. Gates, G. Natale, Dynamics of Brownian Janus rods at a liquid-liquid interface, Phys. Fluids 34 (2022) 012117.

[55] M. K. Gilson, J. A. Given, B. L. Bush, J. A. McCammon, The statistical-thermodynamic basis for computation of binding affinities: a critical review, Biophys. J. 72 (1997) 1047.

[56] J. Hénin, J. Gumbart, C. Chipot, In silico alchemy: A tutorial for alchemical free-energy perturbation calculations with NAMD, Centre National de la Recherche Scientifique, University of Illinois, Urbana-Champaign (2017).

[57] W. G. Hoover, Nonequilibrium molecular dynamics, Annu. Rev. Phys. Chem. 34

doi:10.6342/NTU202404382

(1983) 103.

[58] M. Martínez-Jiménez, M. Serrano-Ocaña, J. Alejandre, United atom model for ionic liquids: UAM-IL, J. Mol. Liq. 329 (2021) 115488.

[59] F. Gonçalves, A. Trindade, C. Costa, J. Bernardo, I. Johnson, I. Fonseca, A. Ferreira, PVT, viscosity, and surface tension of ethanol: New measurements and literature data evaluation, J. Chem. Thermodyn. 42 (2010) 1039.

[60] L. Chen, E. Bonaccurso, Effects of surface wettability and liquid viscosity on the dynamic wetting of individual drops, Phys. Rev. E 90 (2014) 022401.

[61] P. G. Bange, G. Upadhyay, N. D. Patil, R. Bhardwaj, Isothermal and non-isothermal spreading of a viscous droplet on a solid surface in total wetting condition, Phys. Fluids 34 (2022) 112115.

[62] L. Tanner, The spreading of silicone oil drops on horizontal surfaces, J. Phys. D Appl. Phys. 12 (1979) 1473.

[63] S.-W. Hu, C.-Y. Wang, Y.-J. Sheng, H.-K. Tsao, Peculiar Wetting of N, N-dimethylformamide: Expansion, contraction, and self-running, J. Phys. Chem. C 123 (2019) 24477.

[64] Y.-H. Weng, C.-J. Wu, H.-K. Tsao, Y.-J. Sheng, Spreading dynamics of a precursor film of nanodrops on total wetting surfaces, Phys. Chem. Chem. Phys. 19 (2017) 27786.

[65] Q. Xie, M. A. Alibakhshi, S. Jiao, Z. Xu, M. Hempel, J. Kong, H. G. Park, C. Duan, Fast water transport in graphene nanofluidic channels, Nat. Nanotechnol. 13 (2018) 238.

[66] G.-Y. He, H.-K. Tsao, Y.-J. Sheng, Wicking dynamics into two-rail open channel with periodical branches, Phys. Fluids 34 (2022) 102004.

[67] R. Zhou, Z. Qiu, C. Sun, B. Bai, Entrance loss of capillary flow in narrow slit

doi:10.6342/NTU202404382

nanochannels, Phys. Fluids 35 (2023) 042005.

## 3-6 Supporting Information

Table 3-S1. (a) Non-bonded and (b) bonded force field parameters for various interaction sites in graphene and ethanol molecule.

| (a) non-bonded parameters | atom | $R_{min}$ (Å) | ε (kcal/mol) | q (e) |
|---|---|---|---|---|
| Ethanol | C ($CH_3$) | 4.100 | 0.078 | -0.270 |
| | C ($CH_2$) | 4.020 | 0.056 | +0.048 |
| | O | 3.530 | 0.192 | -0.648 |
| | H ($H_3$-C) | 2.680 | 0.024 | +0.090 |
| | H ($H_2$-C) | 2.680 | 0.035 | +0.090 |
| | H (H-O) | 0.449 | 0.046 | +0.420 |
| Graphene | C | 3.980 | 0.070 | 0 |

| (b) bonded parameters | | | $K_b$ (kcal/mol) | $b_0$ (Å) | |
|---|---|---|---|---|---|
| Bond | Ethanol | C-C | 222.50 | 1.528 | |
| | | C-H ($CH_3$) | 322.00 | 1.111 | |
| | | C-H ($CH_2$) | 428.00 | 1.420 | |
| | | C-O | 309.00 | 1.111 | |
| | | O-H | 545.00 | 0.960 | |
| | Graphene | C-C | 322.55 | 1.420 | |
| | | | $K_\theta$ (kcal/mol) | $\theta_0$ (degrees) | |
| Angle | Ethanol | C-C-H (C-$CH_2$) | 34.60 | 110.10 | |
| | | C-C-H (C-$CH_3$) | 75.70 | 110.10 | |
| | | C-O-H | 50.00 | 106.00 | |
| | | C-C-O | 34.60 | 110.10 | |
| | | O-C-H | 45.90 | 108.89 | |
| | | H-C-H ($CH_3$) | 35.50 | 108.40 | |
| | | H-C-H ($CH_2$) | 35.50 | 109.00 | |
| | Graphene | C-C-C | 53.35 | 120.00 | |
| | | | $K_\chi$ (kcal/mol) | n (multiplicity) | δ (degrees) |
| Dihedral angle | Ethanol | C-C-O-H | 1.13 | 1 | 0 |
| | | | 0.14 | 2 | 0 |
| | | | 0.24 | 3 | 0 |
| | | H-C-C-H | 0.16 | 3 | 0 |
| | | H-C-O-H | 0.16 | 3 | 0 |
| | | H-C-C-O | 0.18 | 3 | 0 |
| | Graphene | C-C-C-C | 3.15 | 2 | 180.0 |
| | | | $K_\varphi$ (kcal/mol) | $\varphi_0$ (degrees) | |
| Improper angle | Graphene | C-C-C-C | 15.00 | 0 | |

# Chapter 4 Enhancement of capillary flow via precursor film thickening in graphene nanochannels

## Abstract

The wicking dynamics of total wetting liquids in a nanocapillary differ from those of partial wetting liquids due to the presence of the precursor film. In this work, the wetting behavior of total wetting liquids (isopropyl alcohol and dimethylformamide) on graphene sheets, as well as the imbibition dynamics in graphene-based nanoslits, are investigated using molecular dynamics. The spontaneous spreading dynamics can be described by two power laws, with the long-term behavior conforming to the viscosity-dominated Tanner's law. The imbibition behavior within nanoslits shows a deviation from Washburn's equation, displaying a unique two-stage pattern. This pattern is marked by a turning point that is related to the type of liquid and is independent of the channel width. Notably, the imbibition rate in the second stage exceeds that in the first. The advancing rate of the precursor film is insensitive to changes in channel width. After the precursor film reaches the end of the channel, the second stage commences, followed by the re-thickening of the film. This re-thickening reduces the curvature radius of the meniscus and increases the driving Laplace pressure, thereby enhancing the capillary flow in the second stage.

**Keywords:** nanocapillary flow, graphene nanochannels, total wetting, precursor film, imbibition dynamics, spreading dynamics.

doi:10.6342/NTU202404382

## 4-1 Introduction

Capillary flow involves the movement of a liquid through narrow spaces caused by capillary pressure, without the aid of external forces [1-3]. Capillary-driven transport of liquids in channels is ubiquitous in nature and technology, such as fluid flow in plants and microfluidic devices [4,5]. This phenomenon is controlled by a combination of physical factors, such as interfacial tension, viscous drag, and solid geometries, which work together in a synergistic manner [6-9]. In microchannels, flow is mainly driven by surface forces (interfacial tensions) rather than body forces like gravity due to the large surface-to-volume ratio [10,11]. Recently, graphene-based nanofluidic devices have been developed due to its exceptionally large specific surface area and superior electronic and mechanical properties [12-15]. Rectangular graphene nanochannels were fabricated through the van der Waals assembly of two-dimensional materials, allowing for precise control of the slit height down to the Angstrom scale [16]. These nanofluidic devices have novel applications including nanofiltration and water desalination [17,18].

Capillarity only occurs in channels with wettable walls. Wettability is a characteristic of a solid substrate, and it is determined by the intermolecular interactions between the solid surface and the fluid [19]. In general, the wetting behavior of a liquid droplet on a surface is described by the contact angle ($0° < \theta < 180°$) for the partial wetting state [20-22]. However, droplets of some liquids tend to spread spontaneously and continuously, resulting in the development of a liquid film with a contact angle of zero. This scenario is referred to as the total wetting state [23]. In this state, the static contact angle is no longer appropriate to describe the wetting behavior [24]. As a result, the spreading coefficient is introduced, and it is defined as $S = \gamma_{sv} - \gamma_{sl} - \gamma_{lv}$, where $\gamma_{sv}$, $\gamma_{sl}$, and $\gamma_{lv}$ represent solid-vapor, solid-liquid, and liquid-vapor tensions, respectively [25]. While the spreading coefficient is negative for partial wetting ($S < 0$), it becomes positive for total wetting

doi:10.6342/NTU202404382

($S \geq 0$) [26].

Until now, the wettability of liquid droplets on a graphene surface has been limited to the water/graphene system [20]. The partial wetting behavior was reported in experiments, with the water contact angle ranging from 82° to 90° [21,22,27]. The wetting behavior of water nanodroplets on a graphene surface was also investigated through simulations [20,28,29], revealing an equilibrium contact angle of $\theta = 76$ - $90°$, which is in agreement with the experimental data. Various suitable organic solvents, including ethanol (EOL), dimethylformamide (DMF), tetrahydrofuran (THF), and isopropyl alcohol (IPA), have been successfully applied to the liquid phase exfoliation of graphene sheets from bulk graphite [30-32]. During the exfoliation process, it is essential to achieve a well-dispersed state of graphene sheets within the solvent, which serves as the dispersion medium [33]. This result implies that the wetting behavior of those solvents on a graphene surface approaches a state of total wetting. However, there has been no experimental investigation conducted to determine the equilibrium contact angle and surface wettability between organic solvents and graphene. Recently, the wetting behavior of the ethanol/graphene system has been studied, revealing a spreading coefficient value of $S = 56.4$ mN/m $> 0$. This suggests a state of total wetting, where ethanol fully spreads on the graphene surface [34].

The imbibition dynamics of water into graphene nanoslits have been investigated both experimentally and theoretically [16,20,35]. Surprisingly, a remarkably rapid flow rate was observed, surpassing the velocities predicted by Washburn's equation under the assumption of a no-slip boundary condition. Furthermore, it was discovered that the penetration rate decreases as the channel width increases, which contrasts with the prediction of Washburn's equation where the penetration rate is expected to increase with larger channel widths [20]. The breakdown of Washburn's equation for graphene nanoslits can

doi:10.6342/NTU202404382

be addressed by incorporating the concept of slip length, which becomes significant in nanoscale channels [20]. However, for total wetting liquids characterized by S > 0 and a zero contact angle, the applicability of Washburn's equation to the imbibition in nanoslits remains unresolved. Recently, the wicking process of ethanol (total wetting) in graphene nanochannels was investigated through molecular dynamics (MD) simulations [34]. The progression of the precursor film in graphene nanoslits was observed, and the imbibition velocity of ethanol was found to be significantly higher compared to that of water.

The imbibition dynamics of total wetting liquids in graphene nanoslits have only been simulated for ethanol [34]. Currently, the impact of other total wetting liquids, specifically organic solvents with varying spreading coefficients, on the imbibition behavior remains unknown and requires further investigation. During the MD simulation, it was observed that the precursor film of ethanol moved notably faster than the meniscus. Generally, the simulation was terminated once the precursor film reached the end of the channel [34]. As a result, the impact of the precursor film on the main flow is not yet fully understood. In this study, organic solvents used for graphene exfoliation are considered, including DMF and IPA. Additionally, the imbibition behavior of the main flow after the precursor film reaches the channel end is investigated using MD simulations. First, the total wetting state of the liquids is examined by calculating their spreading coefficients. The dynamics of the spontaneous spreading behavior is studied as well. Secondly, the wicking characteristics before and after the precursor film reaching the channel end are analyzed based on the penetration length and internal energy. The effect of the nanochannel width on the imbibition dynamics is also investigated. Finally, the role of the precursor film in modifying the main flow associated with the meniscus is explained.

## 4-2 Method

doi:10.6342/NTU202404382

The Nanoscale Molecular Dynamics (NAMD) package was utilized to simulate the wetting behavior of nanodroplets and the spontaneous capillary flow in nanoslits. NAMD is an open-source, free MD simulation software [36] that employs the Charm++ parallel programming model to efficiently simulate thousands of molecules on parallel computer systems [37-39]. This program incorporates equations of motion, integration methods, classical MD force fields, electrostatics evaluation algorithms, and temperature and pressure controls for efficient simulations [40]. VMD, a molecular graphics program, was employed for the visualization and analysis of molecular velocities and positions [41]. It functions as a molecular visualization tool, facilitating simulation preparation, 3D graphics-based display, animation, and analysis of complex molecular systems. Additionally, it offers built-in scripting capabilities. When combined with NAMD, VMD can effectively extract thermodynamic and structural information [38].

The simulations were conducted in a canonical (NVT) ensemble using the Langevin thermostat to maintain a constant temperature of 300 K. The interatomic van der Waals interaction was modeled using the Lennard-Jones (L-J) 12-6 potential, with a cutoff distance of 12 Å and an extended pair list distance of 14 Å. The L-J parameters for different atom types were determined using the Lorentz-Berthelot mixing rule [42,43]. The Coulomb potentials were used to describe electrostatic interactions, and the particle-mesh Ewald summation method was adopted to account for long-range electrostatic interactions [44]. The L-J parameters for carbon atoms in graphene [45], as well as for DMF, IPA, and THF molecules [46], were obtained from the CHARMM force field. The distance between adjacent carbon atoms within a graphene layer is 0.142 nm, while the interlayer distance is fixed at b = 0.335 nm. The Supporting Information, specifically Table 4-S1, provides a comprehensive list of the non-bonded parameters (ε and $R_{min}$) and atomic charges (q) for all atoms in Table 4-S1**(a)**, while the bonded parameters can be found in

doi:10.6342/NTU202404382

Table 4-S1**(b)**.

This study encompassed three simulation systems: interfacial tensions, spreading dynamics, and imbibition dynamics. The calculation of surface tension, denoted as $\gamma_{lv}$, utilized the Irving-Kirkwood expression $\gamma_{lv} = [p_{zz}-(p_{xx}+p_{yy})/2](L_z/2)$, where $p_{xx}$, $p_{yy}$, and $p_{zz}$ represent the diagonal components of the pressure tensor [47-50]. The factor of 1/2 associated with $L_z$ (the box length along the z-direction) accounts for the presence of two surfaces along the x-y plane in the system. By placing the liquid layer in the middle of the simulation box and orienting the liquid-vapor interface perpendicular to the z-direction, the pressure tensor of the system was recorded after achieving equilibrium in a canonical ensemble simulation. The interfacial tension, $\gamma_{sv}$ - $\gamma_{sl}$, was determined using free energy perturbation theory, assessing the free energy difference ($\Delta$F) between two states via a coupling parameter $\lambda$, varying from 0 to 1 to connect reference and perturbed states [51,52]. By considering a sheet of graphene within the system containing total wetting liquid molecules, $\gamma_{sv}$ - $\gamma_{sl}$ was derived from $\Delta F/(2A)$, where 2A signifies the solid-liquid interfacial area. Internal energy was monitored throughout the simulation. The system of spreading dynamics was detailed in Sec. 3.1.

The imbibition system featured a graphene nanoslit positioned vertically above a reservoir, as illustrated in Fig. 4-1. The reservoir underwent a 4 ns equilibration at 300 K before the nanoslit placement. The nanocapillary wall comprised three layers of graphene sheets. To prevent capillary flow along the nanoslit's outer walls, a single graphene sheet acted as a baffle atop the reservoir. The width of the nanoslits (w) was defined as $w = N \times b$, with N representing the number of graphene sheets and b = 0.335nm denoting the interlayer distance. For simplicity, the channel width is denoted by N thereafter and it ranges from N = 3 to 8 in this work. The nanocapillary's total length in the z-direction was $L_c$ = 60 nm, and the simulation box sizes in the x- and y-direction were $L_x$ = 16.75

doi:10.6342/NTU202404382

nm and $L_y = 4.25$ nm, respectively, under periodic boundary conditions. Throughout the imbibition simulations, both the penetration length describing the main capillary flow associated with the moving meniscus, l(t), and the advancing front of the precursor film adhered to the graphene wall, $l_p(t)$, were monitored.

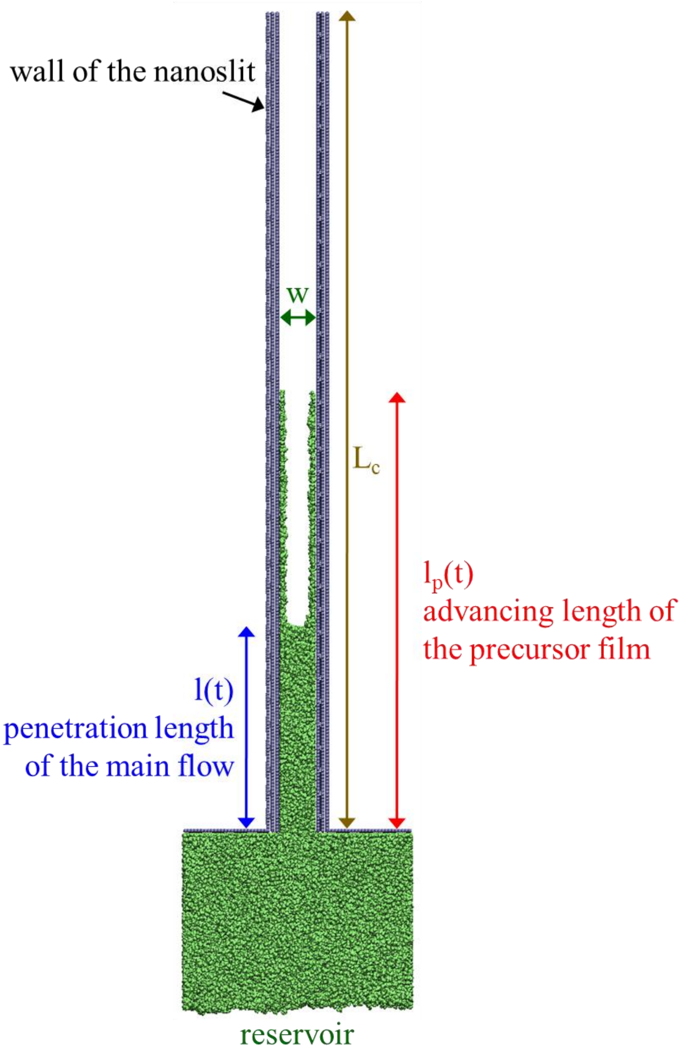

**Fig. 4-1.** Schematic diagram illustrating the spontaneous capillary flow of a total wetting liquid through a nanoslit. The reservoir is positioned directly beneath the entrance of the nanoslit.

## 4-3 Results

### 4-3-1 Spreading of total wetting liquids on graphene

The spontaneous capillary flow in graphene nanochannels is caused by the surface wettability of a liquid, which is directly related to interfacial tensions. By using MD, the interfacial tension ($\gamma_{sv}$ - $\gamma_{sl}$) can be estimated through the free energy perturbation method, while the surface tension $\gamma_{lv}$ can be calculated using the Irving-Kirkwood expression. The spreading coefficient is subsequently evaluated to determine whether the liquid on the graphene is in a state of total wetting or not. The simulation results of EOL, DMF, IPA, and THF at a temperature of 25°C are presented in Table 4-1. The agreement between the theoretical and experimental values of $\gamma_{lv}$ is reasonably good [53-56]. However, it is worth noting that ($\gamma_{sv}$ - $\gamma_{sl}$) cannot be directly measured through experimental methods. All four liquids demonstrate positive spreading coefficients, indicating a total wetting behavior on graphene. Nonetheless, THF exhibits the highest S, while DMF has the lowest S among the three liquids.

**Table 4-1.** The interfacial tensions and spreading coefficient (S) of organic liquids on graphene. The experimental data for $\gamma_{lv}$ are listed in parentheses.

| Liquid \ Tension | $\gamma_{lv}$ (mN/m) | $\gamma_{sv}$ - $\gamma_{sl}$ (mN/m) | S (mN/m) |
|---|---|---|---|
| EOL | 24.1 (22.3) | 80.4 | 56.4 |
| DMF | 40.3 (36.6) | 92.5 | 52.2 |
| IPA | 22.9 (21.2) | 81.0 | 58.2 |
| THF | 25.2 (27.0) | 90.3 | 65.0 |

Depositing a nanodroplet on the graphene surface enables the direct observation of its wetting behavior. The nanodroplet has been equilibrated at 300 K for 3 ns prior to

doi:10.6342/NTU202404382

deposition, after which it is placed on the graphene substrate comprising three layers of graphene sheets. Fig. 4-2 demonstrates the spreading process of DMF and IPA on graphene, presenting both side and top views with a series of snapshots captured at intervals from 0.005 to 1.7 ns. It was observed that the contact angles of the droplets gradually decreased as time progressed. By t = 1.7 ns, both two droplets had completely spread out on the graphene surface. The observed spontaneous spreading behavior implied the absence of a finite equilibrium contact angle, signifying a state of total wetting. These findings were consistent with the previously predicted positive spreading coefficients as shown in Table 4-1.

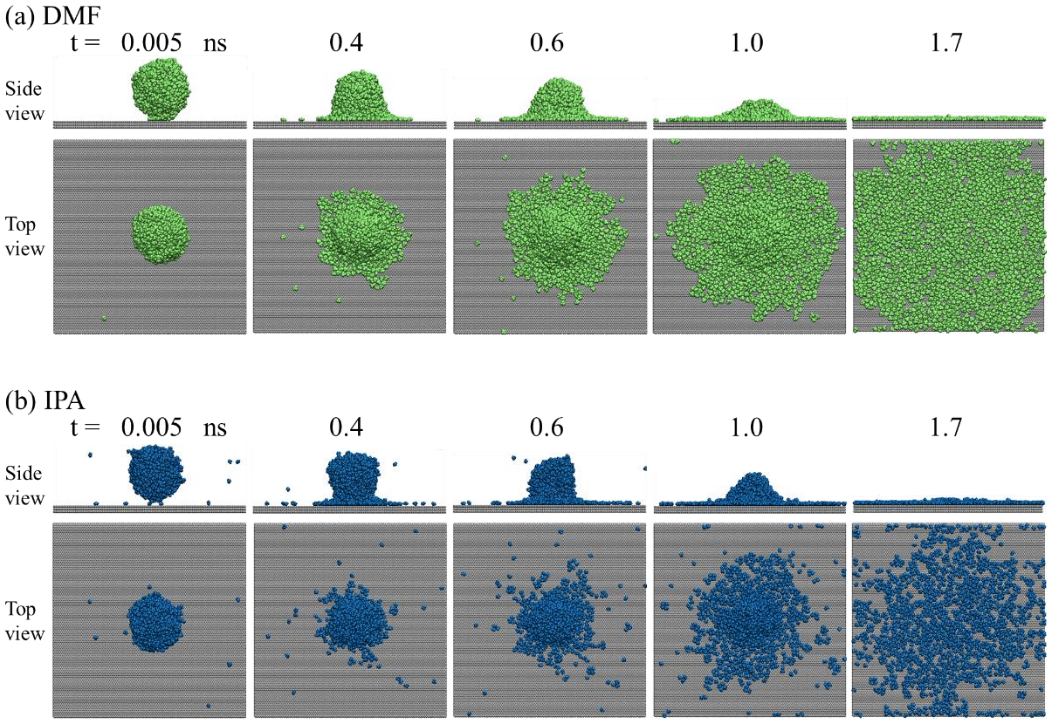

**Fig 4-2.** A series of snapshots at various time intervals, including side and top views, depict the spreading processes of nanodroplets of (a) DMF and (b) IPA on graphene.

In order to balance the interfacial tensions at the three-phase contact line, a liquid droplet placed on a solid substrate is driven to expand and attain an equilibrium shape.

Right after contact, the primary hindrance to capillary-driven spreading is the inertia of the droplet. During this period, the spreading radius (r) and the wetted area (A) increase with time (t), following a power law relationship ($r \sim t^{1/2}$ and $A \sim t$), regardless of the surface wettability. The inertio-capillary time scale, denoted as $\tau_i$, is given by $(\rho R^3/\gamma_{lv})^{1/2}$ [57,58], where ρ represents the density of the liquid and R is the initial radius of the droplet. As spreading continues, the resistance due to inertia decreases, while the dominant force becomes the viscous force. During this period, for small contact angle droplets, the spreading radius and the wetted area can also be described by power laws, $r \sim t^{1/10}$ and $A \sim t^{1/5}$, known as Tanner's law [57,59-61].

Since both DMF and IPA do not exhibit a finite equilibrium contact angle, monitoring the complete spreading processes of their nanodroplets can provide valuable insights into the dynamics of spreading. In these systems, there is a thin liquid film extending from the nominal contact line, and a notable change in curvature is observed. This change signifies the presence of a precursor film at the leading edge of the nanodroplet. By eliminating the influence of the precursor film on the wetted area of the spreading film, one can define an area ($A_b$) corresponding to the base area associated with the spherical cap shape. Fig. 4-3 depicts the spreading behavior of nanodroplets of DMF and IPA deposited on graphene, showcasing the changes in the base area ($A_b$) over time (t). Note that the base area ($A_b$) is different from the total wetted area (A) which includes both the precursor film and the droplet. It is found that the long-time spreading behavior of both DMF and IPA can be depicted by viscous spreading (Tanner's law). Furthermore, there is a noticeable difference in the spreading dynamics between DMF and IPA. For DMF and IPA nanodroplets with radii of 5.35 nm and 5.33 nm, respectively, the characteristic inertial times ($\tau_i$), as defined in the last paragraph, are approximately 0.06 ns and 0.07 ns, respectively [34]. The data points shown in Fig. 4-3 seem to be outside the range of the inertial

doi:10.6342/NTU202404382

spreading regime.

IPA exhibits an approximate power law relation, with $A_b \sim t^{0.5}$ in the short-time period, but transitions to $A_b \sim t^{0.2}$ in the long-time period. A crossover can be observed at $t \approx 0.45$ ns, which is approximately 7 times $\tau_i$. The exponent value of 0.5, which is significantly less than 1.0, also indicates that the spreading behavior in the short-time period already deviates from the inertia-dominated regime. In the transition regime, both inertia and viscosity are influential factors. Furthermore, the decrease in the exponent from 0.5 to 0.2 signifies a shift from the transition regime to the viscous spreading regime. DMF also exhibits two power-law relationships (inset of Fig. 4-3) similar to that of IPA. Throughout the spreading processes, the internal energy of the nanodroplet is observed to decrease continuously. Notably, the internal energy gain in DMF is significantly greater than in IPA, which aligns with the observation that the wetted area of DMF exceeds that of IPA at any given moment, as revealed in Figs. 4-2 and 4-3.

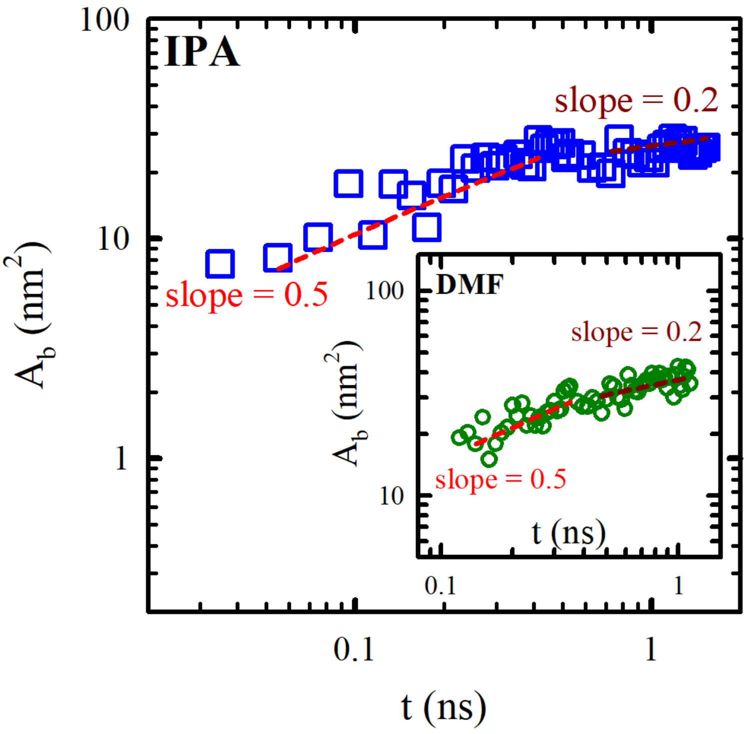

**Fig. 4-3.** Log-log plot of the base area ($A_b$) versus time (t) for IPA (main graph) and DMF

doi:10.6342/NTU202404382

(inset) nanodroplets.

### 4-3-2 Two characteristic regimes in capillary flow

Washburn's equation is commonly used to describe the imbibition dynamics, establishing a relationship between the penetration length (l) and time (t), expressed as $l^2 = S_m t$ [20,35,62]. In this equation, the slope $S_m$ is related to the channel width (w) through the expression $S_m = [\gamma_{lv}\cos(\theta_D) / (3\mu)](w + 6l_s)$ [57], where μ represents the viscosity, $\theta_D$ denotes the dynamic contact angle, and $l_s$ is the slip length. The no-slip boundary condition is associated with the condition $l_s = 0$. Typically, the penetration length is defined as the distance separating the advancing meniscus and the entrance. The time evolution of the lowest position of the advancing meniscus of DMF and IPA in graphene nanocapillaries is illustrated in Figs. 4-4(a) and 4-4(b) for different channel widths (N). It is somewhat surprising to discover that the imbibition dynamics of total wetting liquids cannot be adequately described by Washburn's equation. A turning point associated with two linear segments can be clearly identified in the plot of $l^2$ against t. This consequence indicates that the slope in Washburn's equation will change at a certain point/moment.

For channel widths N = 5, 6, and 8, it was observed that the square of the penetration length is linearly proportional to the imbibition time. However, the slope differs before and after reaching the turning point. The moment associated with the turning point ($t_T$) is independent of the channel width but varies with the liquid type. It was found that $t_T$ approximately equals 15 ns for DMF (refer to Fig. 4-4(a)) and $t_T$ approximately equals 17 ns for IPA (refer to Fig. 4-4(b)). For DMF, the slope is $S_{m1} = 1.15$ nm$^2$/ns for $t < t_T$, but it increases to $S_{m2} = 2.29$ nm$^2$/ns for $t > t_T$ at N = 6. Similarly, for IPA, the slope is $S_{m1} = 0.87$ nm$^2$/ns for $t < t_T$, and it grows to $S_{m2} = 2.51$ nm$^2$/ns for $t > t_T$ at N = 6. It is evident that $S_{m1}$ is always less than $S_{m2}$, regardless of the channel width. Additionally, both $S_{m1}(N)$

doi:10.6342/NTU202404382

and $S_{m2}(N)$ decrease with increasing the channel width. When the channel width is reduced to N = 3, $l^2(t)$ can be adequately described with a single linear line (no turning point), instead of two linear segments. Moreover, the penetration length reaches the end of the channel before $t = t_T$, indicating a faster imbibition rate compared to larger channel widths. In fact, the slopes at N = 3 are $S_m = 3.48$ nm$^2$/ns and $S_m = 3.35$ nm$^2$/ns for DMF and IPA, respectively, which are greater than $S_{m1}(N)$ or $S_{m2}(N)$ with $N \geq 5$.

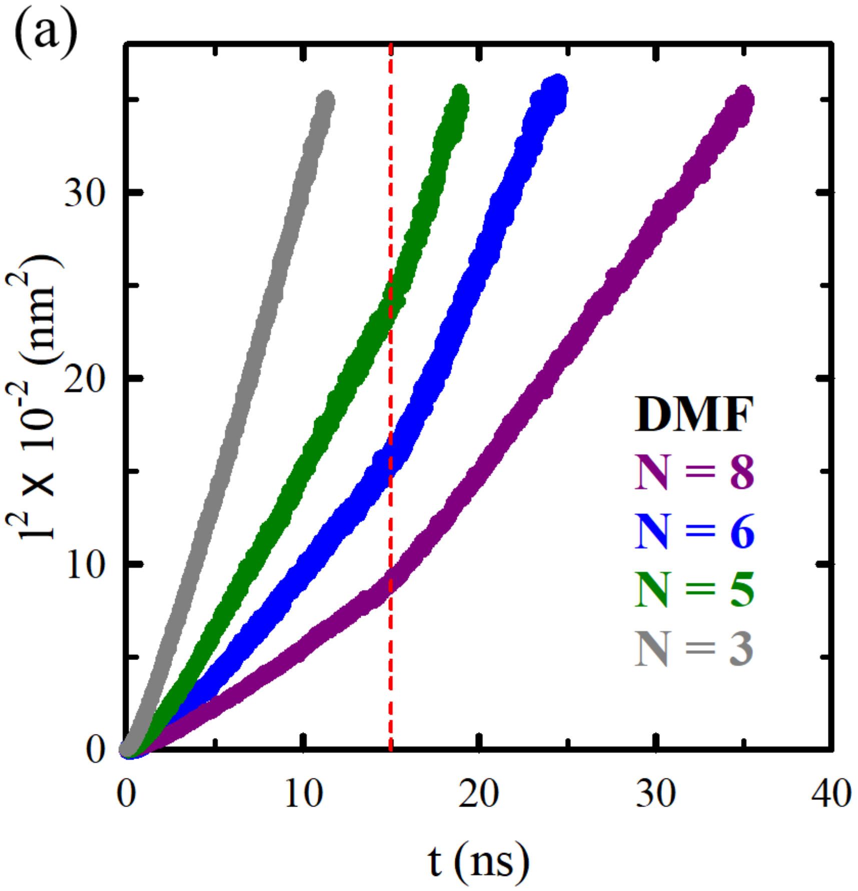

doi:10.6342/NTU202404382

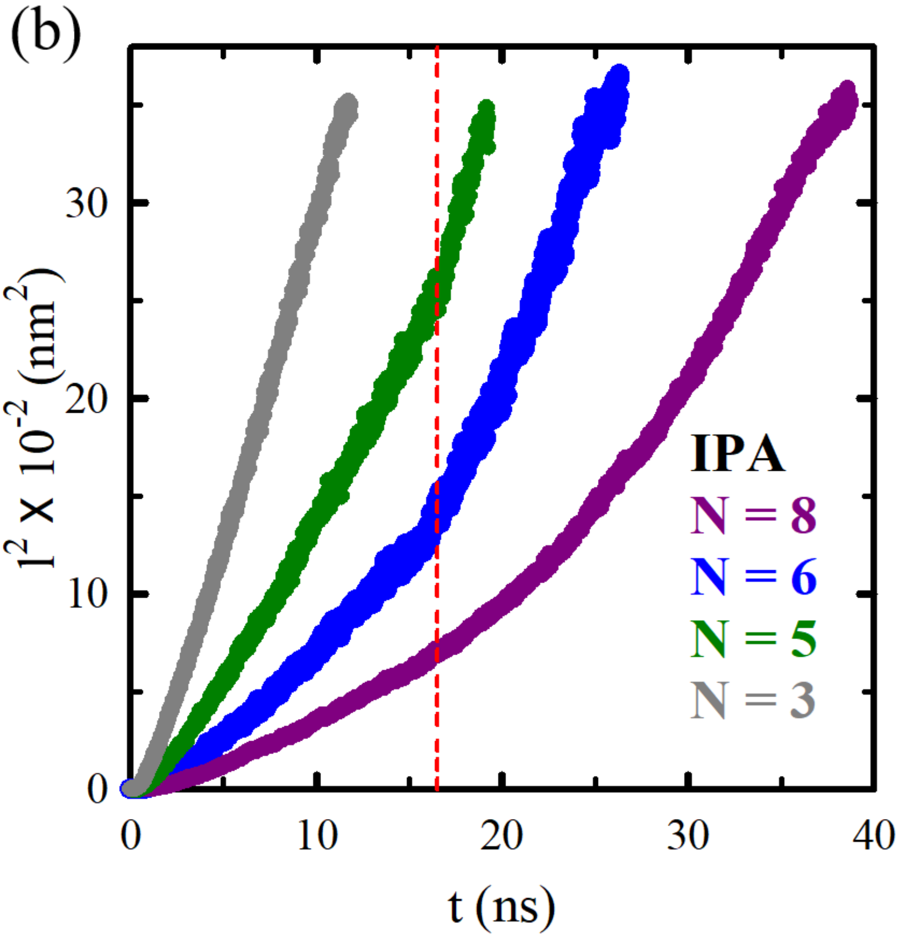

**Fig. 4-4.** The square of the penetration length ($l^2$) versus time is depicted for different graphene-based channel widths in the cases of (a) DMF and (b) IPA.

In the imbibition process, the primary factor expected to reduce the system's free energy ($\Delta F$) is the increasing contact area between the solid and liquid phases (A). In terms of interfacial tensions, the free energy is related to the contact area by $\Delta F(t) \sim (\gamma_{sl} - \gamma_{sv})A(t) < 0$. Since determining the surface free energy through simulations can be challenging, analyzing the change in internal energy ($\Delta U$) resulting from the wetting of a surface can provide valuable insights into the imbibition process. The change in internal energy is expected to be associated with the increase in contact area, which is proportional to the penetration length. As a result, it is anticipated that $\Delta U$ is proportional to $t^{1/2}$. Fig. 4-5 shows the plot of $\Delta U$ against $t^{1/2}$ for the imbibition of DMF with various channel widths. It is found that the internal energy always decreases linearly with time, $\Delta U(t) < 0$ with $\Delta U(0) = 0$, due to the increased wetting of solid surfaces. Consistent with the plot of $l^2$ against t, a turning point appears at $t = t_T$ for $N \geq 5$ but it vanishes for $N = 3$. Moreover, the rate of decrease of ΔU (slope) decreases as the channel width increases. These results indicate that the dynamics of imbibition are indeed governed by the changes in internal energy.

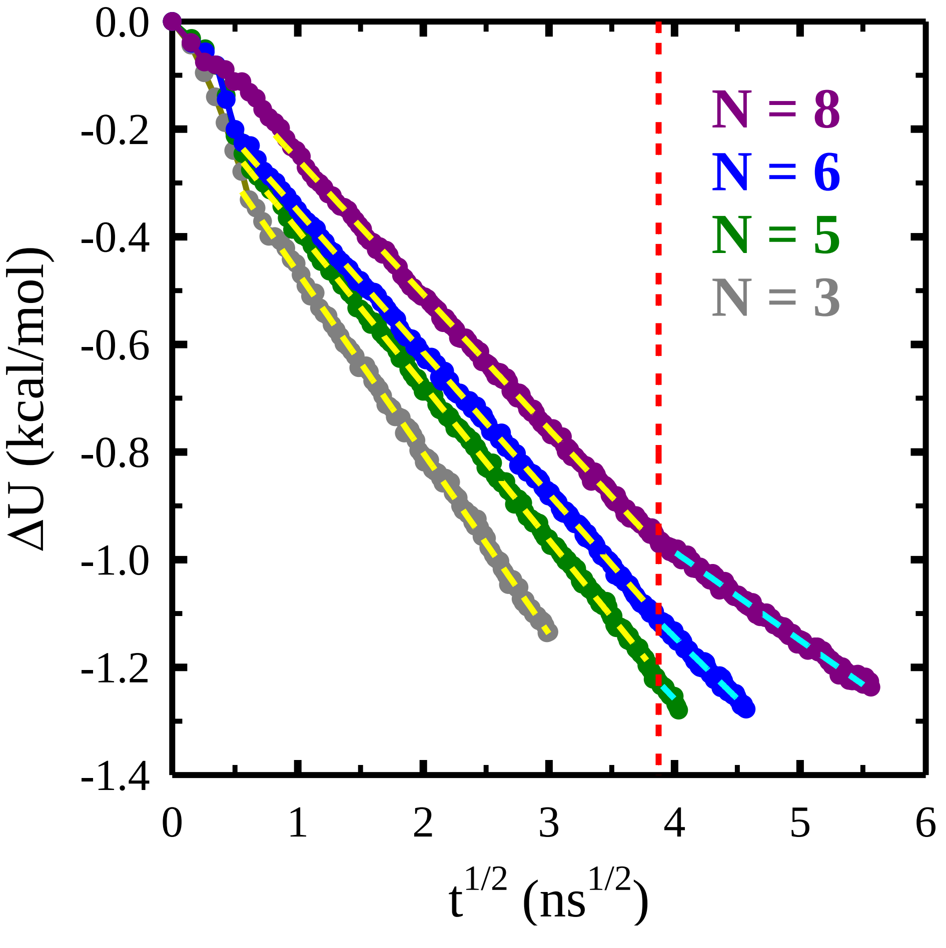

**Fig. 4-5.** The relationship between the change in internal energy (ΔU) and the square root of time ($t^{1/2}$) for the imbibition dynamics of DMF.

### 4-3-3 Advancing precursor film and the change of its thickness

The precursor film is known to emerge when a droplet of the total wetting liquid spreads spontaneously [61]. For the capillary flow of ethanol, which is total wetting in graphene

doi:10.6342/NTU202404382

nanochannel, the precursor film is also identified, and it moves faster than the main flow [34]. The advancements of both the main capillary flow and the precursor film are represented by l(t) and $l_p(t)$, respectively, and it holds that $l_p(t) > l(t)$. For the capillary flow of DMF and IPA (total wetting liquid), the precursor film is present, and similar imbibition phenomena are observed. Fig. 4-6 illustrates the influence of channel width on the advancing rate of the precursor film for DMF at N = 3, 5, 6, and 8. It is observed that $l_p^2$ is also linearly proportional to the wicking time, expressed as $l_p^2 = S_p t$. Contrary to the main flow, the curves of $l_p^2$ versus t for N = 5, 6, and 8 all collapse together. However, for N = 3, the curve of $l_p^2$ versus t does not overlap with those of other N, and its advancing rate of the precursor film is faster compared to other values of N. The inset of Fig. 4-6 shows the effect of the channel width on the advancing rate of the precursor film for IPA. The results are similar to DMF and consistent with the previous study on the imbibition dynamics of ethanol.

For N = 5~8, the advancing rate of the precursor film is insensitive to the channel width, indicating that $S_p$ is independent of N for both DMF and IPA, particularly for sufficiently large N. It is found that the precursor films of DMF and IPA reach the end of the nanocapillary at approximately T = 15 and 17 ns, respectively. This outcome is consistent with the turning point ($t_T$) identified in Fig. 4-4 for the main flows of DMF and IPA. Note that both time scales T and $t_T$ are independent of N. The above comparison suggests that the change in the imbibition rate of the turning point is related to the flow of the precursor film. The distance between the advancing front of the precursor film and the meniscus of the main flow grows with time because $\Delta l = l_p(t) - l(t) = (S_p^{1/2} - S_{m1}^{1/2})t^{1/2}$. Since $S_{m1}$ decreases with increasing N, the leading distance ($\Delta l$) is greater for a larger channel width. For the narrow nanochannel N = 3, the comparison between $l^2(t)$ in Fig. 4-4 and $l_p^2(t)$ in Fig. 4-6 shows that they overlap with each other, indicating that $S_p$ is equal to $S_m$ for both

doi:10.6342/NTU202404382

DMF and IPA. This consequence reveals that the main flow is actually constructed by the overlap of the precursor films on the two walls for small channel widths. This synergetic effect results in a faster-advancing rate of the overlapped precursor film compared to the isolated precursor film. These findings are in agreement with the imbibition dynamics of ethanol [34].

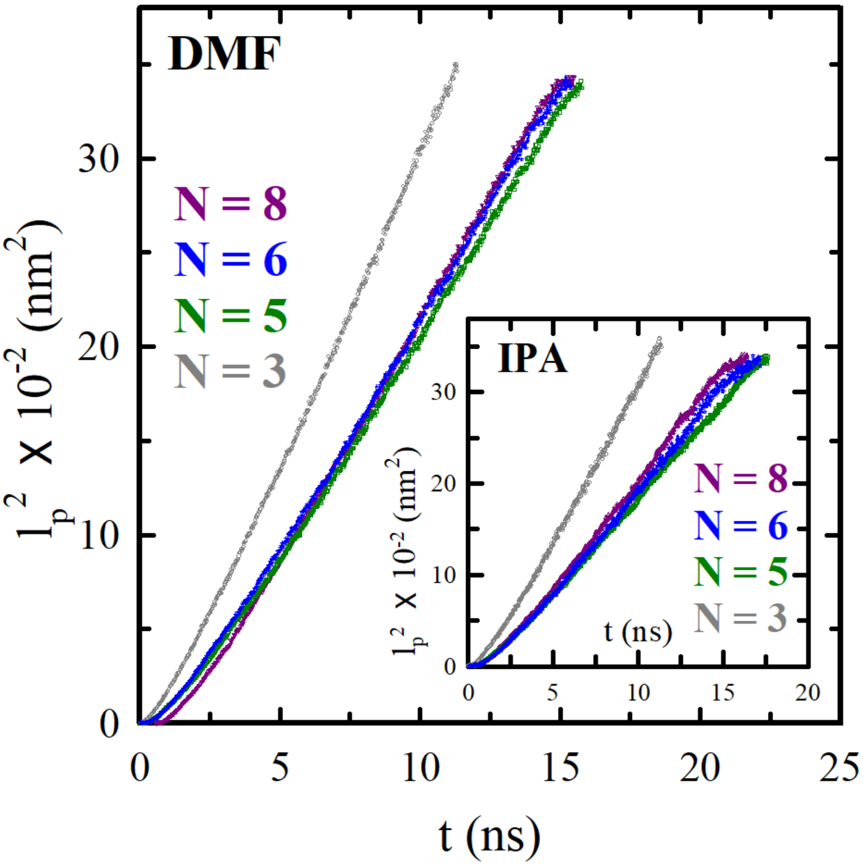

**Fig. 4-6.** The squared advancing length of the precursor film ($l_p^2$) is plotted against time (t) for N = 3, 5, 6, and 8 in the main graph for DMF, and in the inset for IPA.

To achieve a more profound comprehension of the two-stage climbing (imbibition) mechanism in the main flow, a more detailed analysis of changes in the precursor film is conducted during climbing. Fig. 4-7 illustrates the thickness change of the precursor film over time at two fixed height points ($z_1$ = 600 Å and $z_2$ = 650 Å) in the nanochannel with

$N = 8$ for DMF and IPA. Observations were limited to the precursor film on one side of the capillary during each instance, and the data represents the average of at least 10 observations. The qualitative imbibition behavior displayed by DMF's precursor film closely resembles that of IPA. A film thickness of zero indicates that the precursor film has not reached this height point. After reaching this height point at $t = T_1$, the precursor film maintains a thickness of $h_1$ for a certain period of $\Delta T$. Subsequently, the thickening of the precursor film was observed, coming to a halt at time $t = T_2$ and stabilizing at a thickness of $h_2$. When the main flow surpasses this height point, the thickness of the precursor film jumps to $w/2 = 14$ Å, corresponding to half of the capillary thickness. According to Fig. 4-7(a), the characteristic values for DMF at $z_1$ are as follows: $T_1 \approx 7.5$ ns, $\Delta T \approx 6.0$ ns, $h_1 \approx 3.8$ Å, $T_2 \approx 16$ ns, and $h_2 \approx 4.2$ Å. According to Fig. 4-7(b), the characteristic values for IPA at $z_1$ are as follows: $T_1 \approx 10$ ns, $\Delta T \approx 4.5$ ns, $h_1 \approx 5.0$ Å, $T_2 \approx 26$ ns, and $h_2 \approx 8.4$ Å.

After comparing Fig. 4-6 with Fig. 4-7, it is interesting to note that the moment when the precursor film reaches the end of the capillary ($t_T$) aligns closely with the moment when the precursor film at $z_1$ starts to thicken ($T_1 + \Delta T$). That is, the turning point ($t_T$) associated with the main flow $l(t)$, as illustrated in Fig. 4-4 for both DMF and IPA, is directly linked to the thickening point in the precursor film, $t_T \approx T_1 + \Delta T$. In the time period between $t = T_1 + \Delta T$ and $t = T_2$, the imbibition behavior can no longer be depicted by the slope $S_{m1}$ associated with Washburn's equation (see Fig. 4-4) due to the continuous thickening of the precursor film. When $t > T_2$, the precursor film thickness in front of the main flow stabilizes and remains unchanged. As a consequence, the imbibition behavior can once again be described by Washburn's equation, this time with the slope $S_{m2}$. In addition to DMF and IPA, a similar phenomenon has been observed in the imbibition dynamics of ethanol and THF.

doi:10.6342/NTU202404382

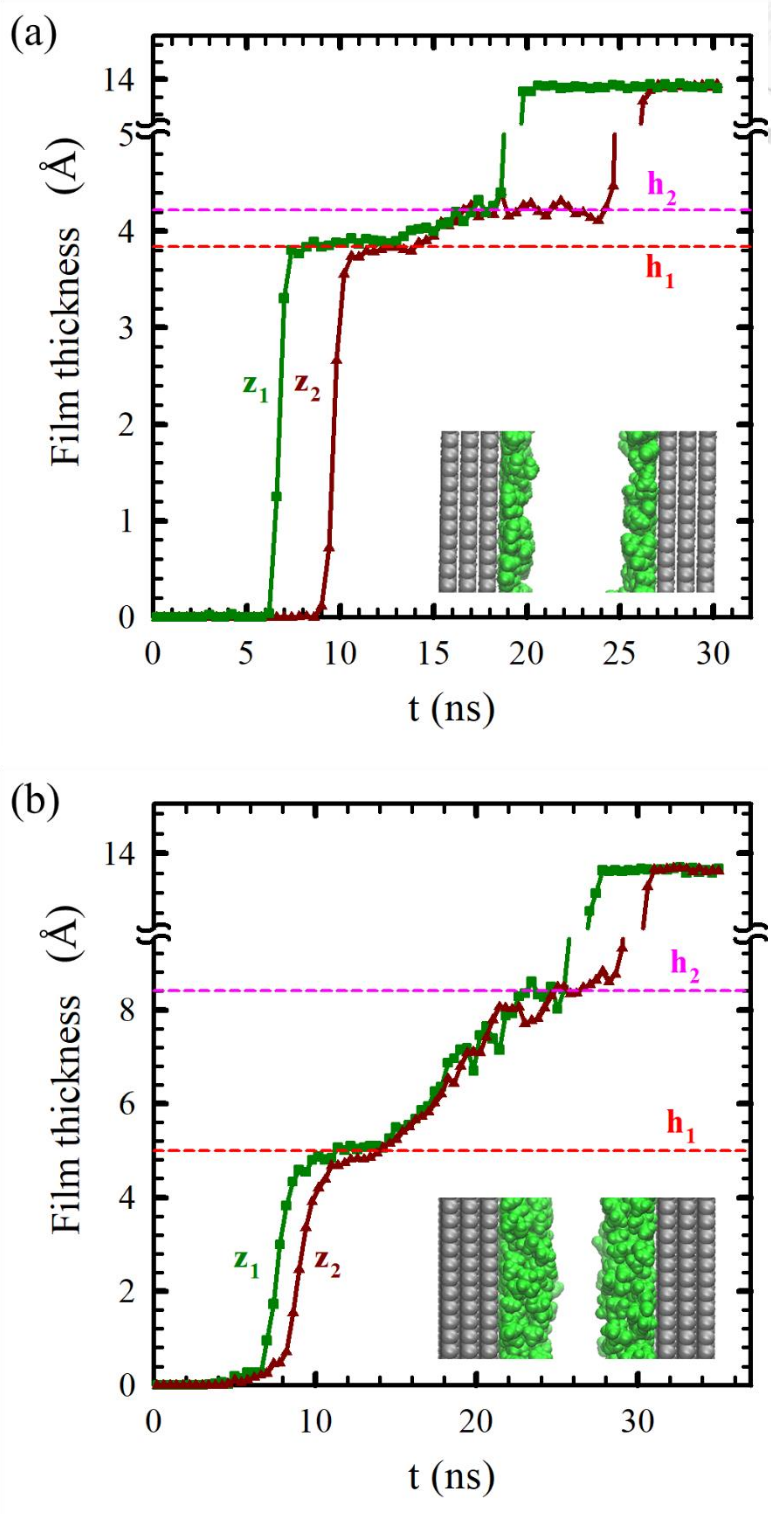

**Fig. 4-7.** The change in thickness of the precursor film over time at two specific height points ($z_1$ = 600 Å and $z_2$ = 650 Å) in the graphene-based nanochannel with N = 8 for (a) DMF and (b) IPA.

### 4-3-4 Precursor film-assisted capillary flow

The imbibition dynamics are intricately connected to the advancing meniscus, which can be delineated by its curvature radius. For partial wetting liquids, the curvature radius can be simply expressed in terms of the contact angle ($\theta_D$). However, for total wetting liquids, where the contact angle is essentially zero due to the precursor film, the curvature radius of the meniscus, which can be determined using ImageJ software, must be used. Fig. 4-8 illustrates the evolution of the meniscus shape (curvature radius) over time during DMF imbibition in nanochannels, with an inset for IPA. Observations indicate that when $t < t_T$, the curvature radius of DMF or IPA is approximately the value denoted by the red dashed line, with curvature radii of $R_1$ = 10.8 and 6.3 Å, respectively. When $t > T_2$ which depends on the position, the curvature radius of DMF or IPA decreases abruptly to approximately the value denoted by the pink dashed line, with curvature radii of $R_2$ = 9.2 and 5.0 Å, respectively. It is evident that the $R_1$ values for both DMF and IPA are larger than their respective $R_2$ values because the thickness of the precursor film is thickened from $h_1$ to $h_2$. After the precursor film reaches the end of the capillary, its re-thickening leads to a reduction in the curvature radius, which, in turn, results in an increase in the driving force (Laplace pressure). As a result, the imbibition rate is enhanced after $t > t_T$, yielding another slope in Washburn's equation. Certainly, this imbibition behavior is distinct from that associated with partial wetting liquids.

doi:10.6342/NTU202404382

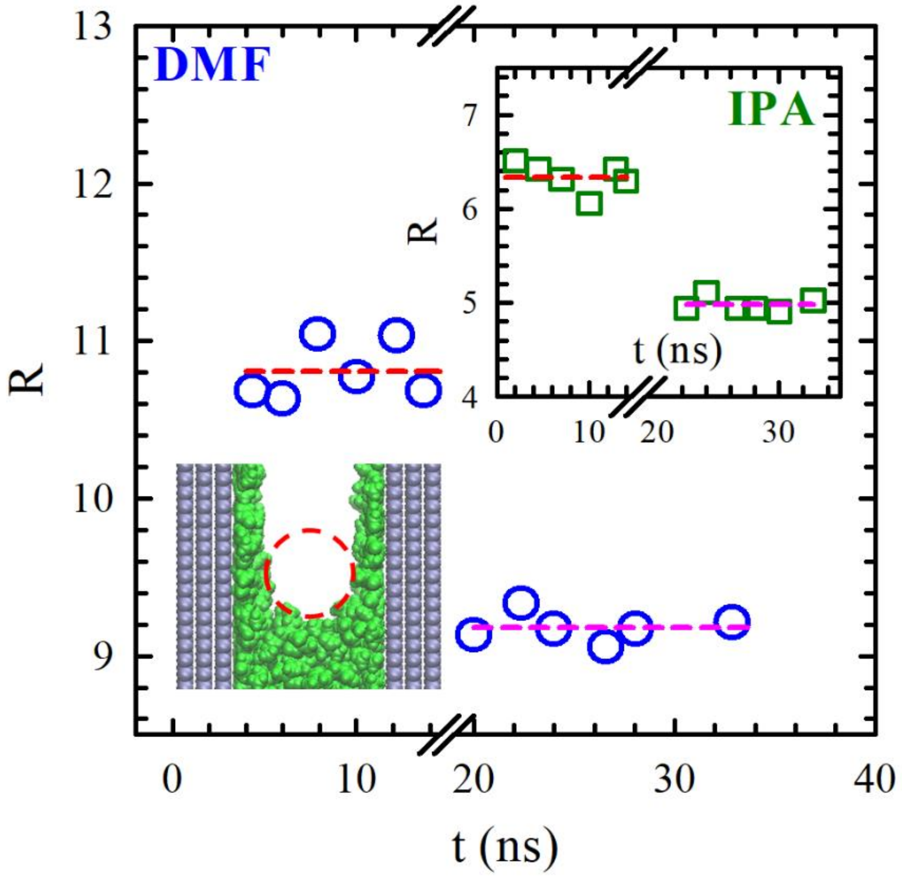

**Fig. 4-8.** The variation of the radius of curvature (R) of the advancing meniscus with time for DMF in a nanoslit with N = 8, with the result for IPA shown in the inset.

Besides the channel width N = 8, the two-stage climbing (imbibition) behavior is observed in the main flow for channel widths N = 5 –7 as well. The imbibition rates before and after the turning point in these channels are also represented by the slopes $S_{m1}$ and $S_{m2}$, respectively. Fig. 4-9 shows the variation of $S_{m1}$ and $S_{m2}$ with the channel width for both IPA and DMF. As the channel width increases from N = 5 to 8, both $S_{m1}$ and $S_{m2}$ decrease, but $S_{m1}$ is always less than $S_{m2}$. The observed decrease in imbibition rate with channel width agrees with the previous studies [20,28,34], yet it contradicts the prediction of Washburn's equation, where $S_m$ is proportional to w. In typical channels, while the

doi:10.6342/NTU202404382

driving Laplace pressure is proportional to $w^{-1}$, the viscous resistance to flow is proportional to $w^{-2}$ [20]. This leads to the imbibition rate being proportional to the channel width. However, in nanoslits, the decrease in viscous resistance caused by increasing the channel width (w) can be significantly mitigated by the slipping behavior at molecularly smooth walls, resulting in a deviation from Washburn's equation.

The influence of the channel width on the driving Laplace pressure can be revealed from the curvature radius of the advancing meniscus. It is important to note that this curvature radius is linked to both the thickness of the precursor film and the channel width, with $R_1 = w/2 - h_1$ and $R_2 = w/2 - h_2$. Fig. 4-10 illustrates the variation in thickness of precursor films for IPA and DMF at various channel widths. The thickness of the precursor film in front of the meniscus is determined, represented by $h_1$ for $t < t_T$ and $h_2$ for $t > t_T$. The thickness $h_1$ is consistently smaller than $h_2$ for both IPA and DMF, irrespective of the channel width. It is interesting to observe that both $h_1$ and $h_2$ increase with the channel width, while the advancing rate of the precursor film is insensitive to N. The rapid increase in $h_2$ compared to $h_1$ results in the growth of the thickness difference ($h_2 - h_1$). The channel width may influence $h_1$ and $h_2$ through changes in the meniscus shape of the main flow. An increase in the curvature radius with the channel width reduces Laplace pressure, elevating the liquid pressure beneath the meniscus. This effect pushes more liquid from the main flow into the precursor film, thereby increasing the film thickness within the nanoslit.

The comparison of IPA and DMF in Fig. 4-9 yields an interesting result: while $S_{m1}$ for DMF is greater than $S_{m1}$ for IPA, $S_{m2}$ for DMF is less than $S_{m2}$ for IPA. This means that before the precursor film reaches the end of the nanocapillary, the main flow of DMF advances faster than that of IPA. However, once the precursor film reaches the channel

doi:10.6342/NTU202404382

end, the main flow of DMF advances more slowly compared to IPA. For a specific channel width w, the imbibition rate in the first stage, as estimated by Washburn's equation, is $(\gamma_{sv} - \gamma_{sl})/\mu$. The experimental viscosities of DMF and IPA are 0.85 and 2.0 g/(cm·s), respectively. The higher viscosity of IPA combined with its smaller value of $(\gamma_{sv} - \gamma_{sl})$ results in a lower $S_{m1}$ for IPA compared to DMF. In the second stage, the Washburn's concept is no longer valid due to the pre-existing precursor film. The imbibition driving force, namely Laplace pressure, is inversely proportional to the curvature radius, given by $(w/2 - h_2)^{-1}$. According to Fig. 4-10, the curvature radius of IPA is significantly smaller than that of DMF in the second stage, although they are comparable in the first stage. The significant increase in the driving force of IPA in the second stage may be responsible for its surpassing imbibition rate compared to DMF.

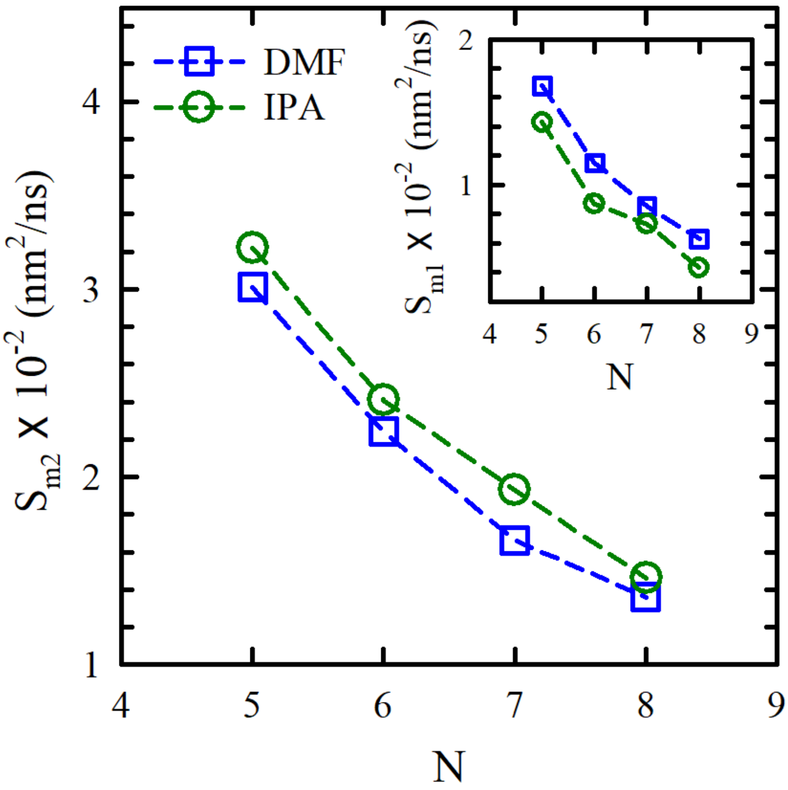

**Fig. 4-9.** The variation in the imbibition rates of the first and second stages ($S_{m1}$ and $S_{m2}$) with the channel width for both DMF and IPA.

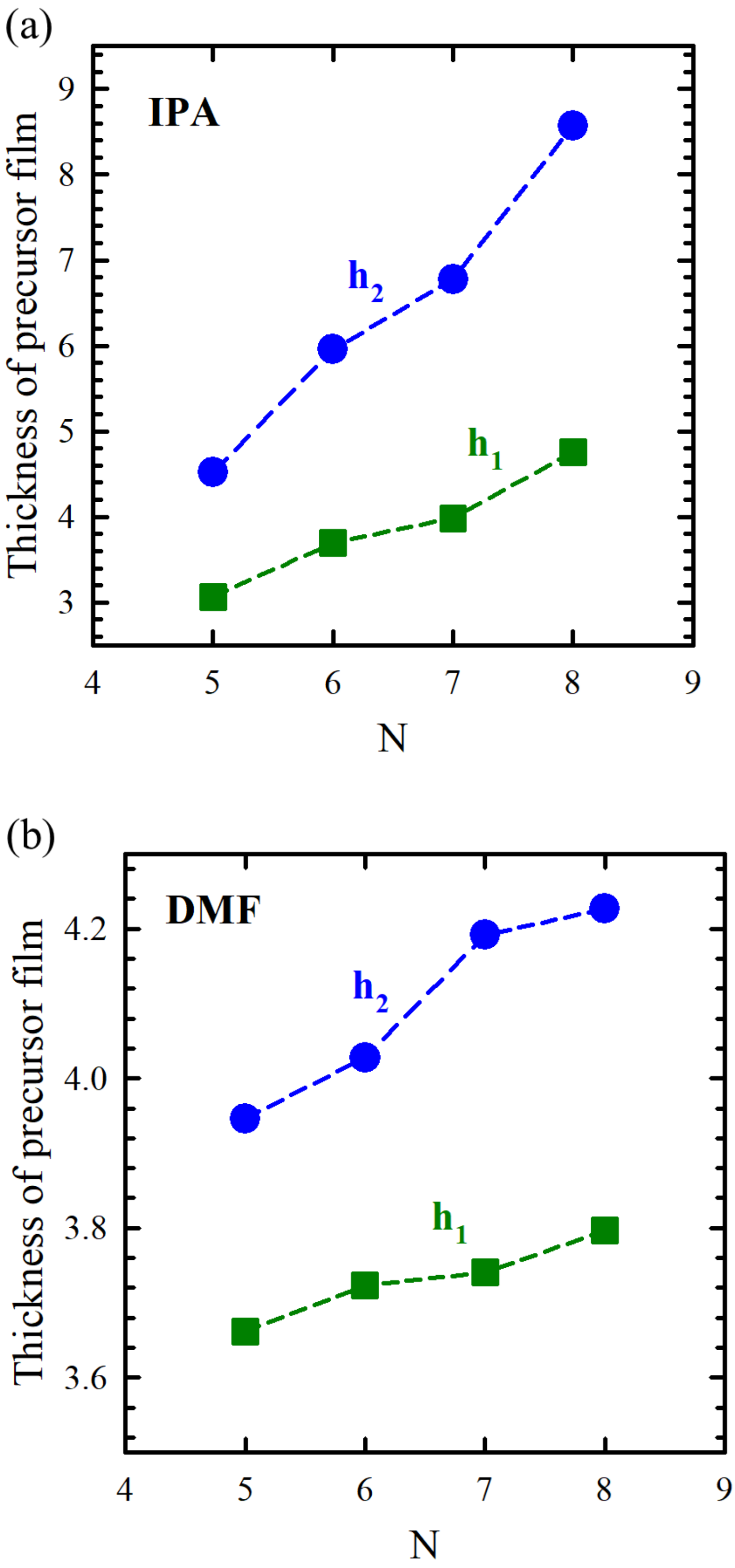

**Fig. 4-10.** The variation in the thickness of the precursor film with the channel width (N) for (a) DMF and (b) IPA. $h_1$ and $h_2$ represent the thickness before and after the turning

point ($t_T$), respectively.

## 4-4 Conclusion

In conclusion, our study provides a detailed exploration of the wetting behavior and imbibition dynamics of isopropyl alcohol (IPA) and dimethylformamide (DMF) in graphene-based nanochannels using molecular dynamics simulations. We have identified IPA and DMF as total wetting liquids on graphene surfaces based on their spontaneous spreading behavior and positive spreading coefficient. Their spreading dynamics can be described by two power laws ($A_b \sim t^n$), from the regime with $n = 0.5$, indicative of a transition from inertia- to viscosity-control, to the regime with $n = 0.2$, characteristic of Tanner's law.

Furthermore, our results show that the imbibition behavior in nanoslits deviates from Washburn's equation, with the imbibition rate decreasing with increasing channel width. Interestingly, for smaller channel widths, the square of the penetration length remains proportional to time, consistent with Washburn's expression. However, for larger channel widths, we observe the presence of two distinct stages in the imbibition process, with a specific crossover time. The turning point in the imbibition behavior is related to the liquid type but independent of the channel width. As the channel width increases, both the imbibition rates before and after the crossover time decrease, with the rate after the crossover time consistently greater than the rate before. This unique imbibition behavior is also reflected in the time evolution of internal energy.

Additionally, we found that the precursor film associated with total wetting liquids advances faster than the meniscus and undergoes re-thickening after reaching the channel end. This re-thickening reduces the curvature radius and increases the driving Laplace pressure, contributing to the acceleration of imbibition in the second stage. Overall, our findings shed light on the complex dynamics of total wetting liquids in nanochannels and provide insights that can inform the design and optimization of nanofluidic devices and membranes.

## 4-5 Reference

[1] J. Zhong, M. A. Alibakhshi, Q. Xie, J. Riordon, Y. Xu, C. Duan, D. Sinton, Exploring anomalous fluid behavior at the nanoscale: Direct visualization and quantification via nanofluidic devices, Acc. Chem. Res. 53 (2020) 347.

[2] P. Kolliopoulos, K. S. Jochem, D. Johnson, W. J. Suszynski, L. F. Francis, S. Kumar, Capillary-flow dynamics in open rectangular microchannels, J. Fluid Mech. 911 (2021) A32.

[3] P. Kolliopoulos, S. Kumar, Capillary flow of liquids in open microchannels: overview and recent advances, npj Microgravity 7 (2021) 51.

[4] M. Nazari, A. Davoodabadi, D. Huang, T. Luo, H. Ghasemi, On interfacial viscosity in nanochannels, Nanoscale 12 (2020) 14626.

[5] A. Kamitani, S. Morishita, H. Kotaki, S. Arscott, Microfabricated microfluidic fuel cells, Sens. Actuators B Chem. 154 (2011) 174.

[6] J. Cai, Y. Chen, Y. Liu, S. Li, C. Sun, Capillary imbibition and flow of wetting liquid in irregular capillaries: A 100-year review, Adv. Colloid Interface Sci. 304 (2022) 102654.

[7] C. J. Ridgway, P. A. Gane, J. Schoelkopf, Effect of capillary element aspect ratio on the dynamic imbibition within porous networks, J. Colloid Interface Sci. 252 (2002) 373.

[8] G. Martic, T. Blake, J. De Coninck, Dynamics of imbibition into a pore with a heterogeneous surface, Langmuir 21 (2005) 11201.

doi:10.6342/NTU202404382

[9] K. Schmid, S. Geiger, Universal scaling of spontaneous imbibition for water-wet systems, Water Resour. Res. 48 (2012) W03507.

[10] R. Zhou, Z. Qiu, C. Sun, B. Bai, Entrance loss of capillary flow in narrow slit nanochannels, Phys. Fluids 35 (2023) 042005.

[11] N. Kavokine, R. R. Netz, L. Bocquet, Fluids at the nanoscale: From continuum to subcontinuum transport, Annu. Rev. Fluid Mech. 53 (2021) 377.

[12] W. Xiong, J. Z. Liu, M. Ma, Z. Xu, J. Sheridan, Q. Zheng, Strain engineering water transport in graphene nanochannels, Phys. Rev. E 84 (2011) 056329.

[13] M. D. Stoller, S. Park, Y. Zhu, J. An, R. S. Ruoff, Graphene-based ultracapacitors, Nano Lett. 8 (2008) 3498.

[14] H. Li, L. Zou, L. Pan, Z. Sun, Novel graphene-like electrodes for capacitive deionization, Environ. Sci. Technol. 44 (2010) 8692.

[15] H. Zhang, X. Lv, Y. Li, Y. Wang, J. Li, P25-graphene composite as a high performance photocatalyst, ACS nano 4 (2010) 380.

[16] B. Radha, A. Esfandiar, F. Wang, A. Rooney, K. Gopinadhan, A. Keerthi, A. Mishchenko, A. Janardanan, P. Blake, L. Fumagalli, Molecular transport through capillaries made with atomic-scale precision, Nature 538 (2016) 222.

[17] J. R. Werber, C. O. Osuji, M. Elimelech, Materials for next-generation desalination and water purification membranes, Nat. Rev. Mater. 1 (2016) 1.

[18] G. Wei, L. Du, H. Zhang, J. Xing, S. Chen, X. Quan, Electrochemical Opening of Impermeable Nanochannels in Laminar Graphene Membranes for Ultrafast Nanofiltration, Environ. Sci. Technol. 57 (2023) 3843.

[19] E. Sadeghinezhad, M. A. Q. Siddiqui, H. Roshan, K. Regenauer-Lieb, On the interpretation of contact angle for geomaterial wettability: Contact area versus three-phase contact line, J. Pet. Sci. Eng. 195 (2020) 107579.

doi:10.6342/NTU202404382

[20] T.-Y. Wang, H.-Y. Chang, G.-Y. He, H.-K. Tsao, Y.-J. Sheng, Anomalous spontaneous capillary flow of water through graphene nanoslits: Channel width-dependent density, J. Mol. Liq. 352 (2022) 118701.

[21] A. Kozbial, C. Trouba, H. Liu, L. Li, Characterization of the intrinsic water wettability of graphite using contact angle measurements: Effect of defects on static and dynamic contact angles, Langmuir 33 (2017) 959.

[22] J. Włoch, A. P. Terzyk, P. Kowalczyk, New forcefield for water nanodroplet on a graphene surface, Chem. Phys. Lett. 674 (2017) 98.

[23] Y. Xu, C. J. Dibble, N. G. Petrik, R. S. Smith, B. D. Kay, G. A. Kimmel, Complete wetting of Pt (111) by nanoscale liquid water films, J. Phys. Chem. Lett. 7 (2016) 541.

[24] K. Nuthalapati, Y.-J. Sheng, H.-K. Tsao, Atypical wetting behavior of binary mixtures of partial and total wetting liquids: leak-out phenomena, Colloids Surf. A Physicochem. Eng. Asp. 666 (2023) 131299.

[25] K.-C. Chu, H.-K. Tsao, Y.-J. Sheng, Spontaneous spreading of nanodroplets on partially wetting surfaces with continuous grooves: Synergy of imbibition and capillary condensation, J. Mol. Liq. 339 (2021) 117270.

[26] K.-C. Chu, H.-K. Tsao, Y.-J. Sheng, Penetration dynamics through nanometer-scale hydrophilic capillaries: Beyond Washburn's equation and extended menisci, J. Colloid Interface Sci. 538 (2019) 340.

[27] A. I. Aria, P. R. Kidambi, R. S. Weatherup, L. Xiao, J. A. Williams, S. Hofmann, Time evolution of the wettability of supported graphene under ambient air exposure, J. Phys. Chem. C 120 (2016) 2215.

[28] Y.-T. Cheng, H.-Y. Chang, H.-K. Tsao, Y.-J. Sheng, Imbibition dynamics and steady flows in graphene nanochannels with sparse geometric and chemical defects, Phys.

doi:10.6342/NTU202404382

Fluids 34 (2022) 112003.

[29] R. Raj, S. C. Maroo, E. N. Wang, Wettability of graphene, Nano Lett. 13 (2013) 1509.

[30] Y. Arao, F. Mori, M. Kubouchi, Efficient solvent systems for improving production of few-layer graphene in liquid phase exfoliation, Carbon 118 (2017) 18.

[31] A. Moosa, M. Abed, Graphene preparation and graphite exfoliation, Turk. J. Chem. 45 (2021) 493.

[32] T. Purkait, R. Ahammed, A. De Sarkar, R. S. Dey, The role of exfoliating solvents for control synthesis of few-layer graphene-like nanosheets in energy storage applications: Theoretical and experimental investigation, Appl. Surf. Sci. 509 (2020) 145375.

[33] Y. Xu, H. Cao, Y. Xue, B. Li, W. Cai, Liquid-phase exfoliation of graphene: an overview on exfoliation media, techniques, and challenges, Nanomaterials 8 (2018) 942.

[34] H.-Y. Chang, H.-K. Tsao, Y.-J. Sheng, Abnormal wicking dynamics of total wetting ethanol in graphene nanochannels, Phys. Fluids 35 (2023) 052017.

[35] Q. Xie, M. A. Alibakhshi, S. Jiao, Z. Xu, M. Hempel, J. Kong, H. G. Park, C. Duan, Fast water transport in graphene nanofluidic channels, Nat. Nanotechnol. 13 (2018) 238.

[36] X. Hu, Z. Zeng, J. Zhang, D. Wu, H. Li, F. Geng, Molecular dynamics simulation of the interaction of food proteins with small molecules, Food Chem. 405 (2023) 134824.

[37] J. C. Phillips, D. J. Hardy, J. D. Maia, J. E. Stone, J. V. Ribeiro, R. C. Bernardi, R. Buch, G. Fiorin, J. Hénin, W. Jiang, Scalable molecular dynamics on CPU and GPU architectures with NAMD, J. Chem. Phys. 153 (2020) 044130.

[38] J. C. Phillips, R. Braun, W. Wang, J. Gumbart, E. Tajkhorshid, E. Villa, C. Chipot,

doi:10.6342/NTU202404382

R. D. Skeel, L. Kale, K. Schulten, Scalable molecular dynamics with NAMD, J. Comput. Chem. 26 (2005) 1781.

[39] A. K. Wong, A. M. Goscinski, A VMD plugin for NAMD simulations on Amazon EC2, Procedia Comput. Sci. 9 (2012) 136.

[40] E. Lilkova, G. Nacheva, P. Petkov, P. Petkov, S. Markov, N. Ilieva, L. Litov, Metadynamics study of mutant human interferon-gamma forms, Comput. Math. Appl. 64 (2012) 272.

[41] W. Humphrey, A. Dalke, K. Schulten, VMD: visual molecular dynamics, J. Mol. Graph. 14 (1996) 33.

[42] D. Mohammad-Aghaie, M. M. Papari, J. Moghadasi, B. Haghighi, Assessment of the effect of mixing rules on transport properties of gas mixtures, Bull. Chem. Soc. Jpn. 81 (2008) 1219.

[43] Q. Guan, B. Shan, R. Wang, G. Feng, Z. Guo, Evaluation of different particle-actuation modes in molecular dynamics and their impact on nanoscale flow behaviors, Phys. Fluids 34 (2022) 072006.

[44] U. Essmann, L. Perera, M. L. Berkowitz, T. Darden, H. Lee, L. G. Pedersen, A smooth particle mesh Ewald method, J. Chem. Phys. 103 (1995) 8577.

[45] S. A. Deshmukh, G. Kamath, S. K. Sankaranarayanan, Comparison of the interfacial dynamics of water sandwiched between static and free-standing fully flexible graphene sheets, Soft Matter 10 (2014) 4067.

[46] K. Vanommeslaeghe, E. Hatcher, C. Acharya, S. Kundu, S. Zhong, J. Shim, E. Darian, O. Guvench, P. Lopes, I. Vorobyov, CHARMM general force field: A force field for drug-like molecules compatible with the CHARMM all-atom additive biological force fields, J. Comput. Chem. 31 (2010) 671.

[47] J. Irving, J. G. Kirkwood, The statistical mechanical theory of transport processes.

doi:10.6342/NTU202404382

IV. The equations of hydrodynamics, J. Chem. Phys. 18 (1950) 817.

[48] J. G. Kirkwood, F. P. Buff, The statistical mechanical theory of surface tension, J. Chem. Phys. 17 (1949) 338.

[49] M. T. Hossain, I. D. Gates, G. Natale, Dynamics of Brownian Janus rods at a liquid-liquid interface, Phys. Fluids 34 (2022) 012117.

[50] Y.-T. Cheng, K.-C. Chu, H.-K. Tsao, Y.-J. Sheng, Size-dependent behavior and failure of young’s equation for wetting of two-component nanodroplets, J. Colloid Interface Sci. 578 (2020) 69.

[51] M. K. Gilson, J. A. Given, B. L. Bush, J. A. McCammon, The statistical-thermodynamic basis for computation of binding affinities: a critical review, Biophys. J. 72 (1997) 1047.

[52] J. Hénin, J. Gumbart, C. Chipot, In silico alchemy: A tutorial for alchemical free-energy perturbation calculations with NAMD, Centre National de la Recherche Scientifique, University of Illinois, Urbana-Champaign (2017).

[53] F. Gonçalves, A. Trindade, C. Costa, J. Bernardo, I. Johnson, I. Fonseca, A. Ferreira, PVT, viscosity, and surface tension of ethanol: New measurements and literature data evaluation, J. Chem. Thermodyn. 42 (2010) 1039.

[54] S. Zhang, L. Zhao, X. Yue, B. Li, J. Zhang, Density, viscosity, surface tension and spectroscopic studies for the liquid mixture of tetraethylene glycol+ N, N-dimethylformamide at six temperatures, J. Mol. Liq. 264 (2018) 451.

[55] M. Bala, V. Singh, Surface tension gradient driven autonomous fatty acid-tetrahydrofuran liquid moving drops: Spreading to pinning, J. Mol. Liq. **375** (2023) 121361.

[56] G. Vazquez, E. Alvarez, J. M. Navaza, Surface tension of alcohol water+ water from 20 to 50. degree. C, J. Chem. Eng. Data 40 (1995) 611.

doi:10.6342/NTU202404382

[57] L. Chen, E. Bonaccurso, Effects of surface wettability and liquid viscosity on the dynamic wetting of individual drops, Phys. Rev. E 90 (2014) 022401.

[58] P. G. Bange, G. Upadhyay, N. D. Patil, R. Bhardwaj, Isothermal and non-isothermal spreading of a viscous droplet on a solid surface in total wetting condition, Phys. Fluids 34 (2022) 112115.

[59] L. Tanner, “The spreading of silicone oil drops on horizontal surfaces,” J. Phys. D: Appl. Phys. 12 (1979) 1473.

[60] S.-W. Hu, C.-Y. Wang, Y.-J. Sheng, H.-K. Tsao, Peculiar wetting of N, N-dimethylformamide: Expansion, contraction, and self-running, J. Phys. Chem. C 123 (2019) 24477.

[61] Y.-H. Weng, C.-J. Wu, H.-K. Tsao, Y.-J. Sheng, Spreading dynamics of a precursor film of nanodrops on total wetting surfaces, Phys. Chem. Chem. Phys. 19 (2017) 27786.

[62] G.-Y. He, H.-K. Tsao, Y.-J. Sheng, Wicking dynamics into two-rail open channel with periodical branches, Phys. Fluids 34 (2022) 102004.

## 4-6 Supporting Information

Table 4-S1. (a) Non-bonded and (b) bonded force field parameters for different interaction sites in IPA, DMF, and graphene.

| (a) non-bonded parameters | atom | $R_{min}$ (Å) | ε (kcal/mol) | q (e) |
|---|---|---|---|---|
| IPA | C (C-$H_3$) | 4.100 | 0.078 | -0.268 |
| | C | 4.000 | 0.032 | +0.139 |
| | O | 3.530 | 0.192 | -0.641 |
| | H ($H_3$-C) | 2.680 | 0.024 | +0.090 |
| | H ($H_2$-C) | 2.680 | 0.035 | +0.090 |
| | H (H-O) | 0.449 | 0.046 | +0.408 |
| DMF | C (C-$H_3$) | 4.100 | 0.078 | -0.093 |
| | C | 4.000 | 0.110 | +0.423 |
| | N | 3.700 | 0.200 | -0.333 |
| | O | 3.400 | 0.120 | -0.523 |
| | H ($H_3$-C) | 2.68 | 0.024 | +0.090 |
| | H (H-C) | 1.8 | 0.046 | +0.079 |
| Graphene | C | 3.980 | 0.070 | 0 |

| (b) bonded parameters | | | $K_b$ (kcal/mol) | $b_0$ (Å) | |
|---|---|---|---|---|---|
| Bond | IPA | C-C | 222.50 | 1.538 | |
| | | C-H (C-$H_3$) | 322.00 | 1.111 | |
| | | C-H (C-$HC_2O$) | 309.00 | 1.111 | |
| | | C-O | 428.00 | 1.420 | |
| | | O-H | 545.00 | 0.960 | |
| | DMF | C-N (C-NOH) | 430.00 | 1.350 | |
| | | C-N (C-$NH_3$) | 315.00 | 1.434 | |
| | | C-O | 620.00 | 1.230 | |
| | | C-H (C-HON) | 317.13 | 1.100 | |
| | | C-H (C-$H_3$) | 322.00 | 1.111 | |
| | Graphene | C-C | 322.55 | 1.420 | |
| | | | $K_\theta$ (kcal/mol) | $\theta_0$ (degrees) | |
| Angle | IPA | C-C-C | 53.35 | 114.00 | |
| | | C-C-O | 75.70 | 110.10 | |
| | | C-C-H ($H_3$C-C-H) | 34.50 | 110.10 | |
| | | C-C-H ($H_3$C-C-$H_3$) | 33.43 | 110.10 | |
| | | C-O-H | 50.00 | 106.00 | |
| | | O-C-H | 45.90 | 108.89 | |
| | | H-C-H ($CH_3$) | 35.50 | 108.40 | |
| | DMF | C-N-C ($H_3$C-N-CH) | 42.00 | 119.50 | |
| | | C-N-C ($H_3$C-N-$CH_3$) | 45.00 | 121.00 | |
| | | N-C-H (N-C-$H_3$) | 50.00 | 105.00 | |
| | | N-C-H (N-C-H) | 43.00 | 115.00 | |
| | | N-C-O | 80.00 | 124.00 | |
| | | O-C-H | 44.00 | 122.00 | |
| | | H-C-H | 35.50 | 108.40 | |
| | Graphene | C-C-C | 53.35 | 120.00 | |
| | | | $K_\chi$ (kcal/mol) | n (multiplicity) | δ (degrees) |
| Dihedral angle | IPA | C-C-O-H | 1.130 | 1 | 0.0 |
| | | | 0.180 | 2 | 0.0 |
| | | | 0.460 | 3 | 0.0 |
| | | C-C-C-H | 0.195 | 3 | 0.0 |
| | | O-C-C-H | 0.200 | 3 | 0.0 |
| | | H-C-C-H | 0.195 | 3 | 0.0 |
| | | H-C-O-H | 0.000 | 3 | 0.0 |
| | DMF | C-N-C-H (HC-N-C-$H_3$) | 0.000 | 3 | 0.0 |
| | | C-N-C-H ($H_3$C-N-C-$H_3$) | 0.420 | 3 | 0.0 |
| | | C-N-C-H ($H_3$C-N-C-H) | 2.600 | 2 | 180.0 |
| | | O-C-N-C | 2.600 | 2 | 180.0 |
| | Graphene | C-C-C-C | 3.150 | 2 | 180.0 |
| | | | $K_\varphi$ (kcal/mol) | $\varphi_0$ (degrees) | |
| Improper angle | DMF | C-N-O-H | 50.0 | 0 | |
| | Graphene | C-C-C-C | 15.0 | 0 | |

# Chapter 5 Conclusion

The emulsion is thermodynamically metastable, with droplets stabilized by adsorbed surfactants that tend to coalesce over time. This makes studying monodisperse compressed emulsions challenging, whether experimentally or via simulations. Concentrated emulsions with volume fractions exceeding the critical value ($\varphi_c$) display an elastic solid-like behavior due to their jammed structures. Despite specifying a volume fraction, the influence of droplet size remains significant yet unclear. Therefore, in the first two parts, the microstructural, thermodynamic, and mechanical characteristics of nanosized concentrated emulsions are explored.

In the first part, we use DPD simulations to study compressed emulsions where monodisperse droplets are jammed, preventing coalescence. Examining the microstructures at various volume fractions ($\phi$), we identify a critical volume fraction ($\phi_c \approx 0.65$) where a structural turning point occurs. The mean coordination number ($\underline{Z}$) increases with $\varphi$, following the scaling relation ($\underline{Z} - Z_c$) ~ $(\phi - \phi_c)^{0.82}$ with $Z_c \approx 6.3$. We also evaluate the internal energy per bead ($\underline{U}$) and heat capacity ($\underline{C}_v$), examining the effects of volume fraction, droplet diameter (D), and interfacial tension ($\sigma$). $\underline{U}$ is separated into contributions from the continuous phase ($\underline{U}_c$), dispersed phase ($\underline{U}_d$), and interface ($\underline{U}_i$). Increasing $\phi$ or decreasing D leads to a rise in $\underline{U}$ due to increases in $\underline{U}_d$ and $\underline{U}_i$. The growth of $\underline{U}_d$ is associated with Laplace pressure buildup, while the growth of $\underline{U}_i$ is linked to interfacial area expansion. Surprisingly, as $\sigma$ increases, $\underline{U}$ ascends while $\underline{U}_i$ decreases. The change in $\underline{U}$ is attributed to increases in both $\underline{U}_d$ and $\underline{U}_c$ due to Laplace pressure increment. The heat capacity and $\underline{U}$ show similar dependencies. All data points can be represented by scaling relations $(\underline{C}_v - \underline{C}_{v,c}) \sim \phi(\phi-\phi_c)^{1/3}(\sigma/D)$ and $(\underline{U} - \underline{U}_c) \sim \phi(\phi-\phi_c)^{1/3}(\sigma/D)$. This simulation approach can also be used to explore the mechanical and viscoelastic properties of compressed emulsions, which are currently being studied.

In the second part, we explore the mechanical properties, including Young's modulus (E) and bulk modulus (K), of monodisperse concentrated emulsions using DPD simulations. The influences of volume fraction ($\phi$), droplet size (D), and interfacial tension ($\sigma$) are systematically examined. Below $\phi_c$ ($\approx 0.65$), the emulsion behaves like a liquid, with Young's modulus vanishing. However, the bulk modulus exists and increases with $\phi$. For $\phi > \phi_c$, a non-zero Young's modulus emerges, increasing with $\phi$. Similarly, K increases with $\phi$, especially near $\phi_c$, indicating a liquid-solid transition.

Droplet size and interfacial tension significantly affect the behavior of concentrated emulsions. Both Young's and bulk moduli increase as D decreases or $\sigma$ increases. This is due to the larger elastic work stored in the interfacial free energy required for a larger Young's modulus. Thus, E is proportional to the interfacial energy per unit volume ($\sigma D^2/D^3 = \sigma/D$). Dimensional analysis shows that the simulation data agree well with the scaling relations $E(\phi) - E(\phi_c) \sim \phi^{0.13}(\phi - \phi_c)^{1.55}(\sigma / D)$ and $K(\phi) - K(\phi_c) \sim \phi^{1.06}(\phi - \phi_c)^{0.15} (\sigma / D)$. The $\phi$-dependent Young's and bulk moduli satisfy the relation $E = 3K(1 - 2\nu)$ valid for isotropic and homogeneous solids. The Poisson's ratio $\nu$ of concentrated emulsions is close to 0.5, consistent with soft materials, but it slightly decreases with increasing $\phi$. Further study should be performed to understand the solid-like properties of concentrated emulsions, including shear modulus and yield stress.

Although the unexpectedly fast capillary flow of water (partial wetting) in graphene nanoslits has been reported, the wicking dynamics of total wetting liquid in a nanocapillary have not been studied. Moreover, the wicking dynamics of total wetting liquids in a nanocapillary differ from those of partial wetting liquids due to the presence of the precursor film. Therefore, in the last two parts, the abnormal Wicking Dynamics in Graphene Nanochannels are investigated.

In the third part, the spreading behavior on graphene sheets and the wicking process in graphene nanochannels are investigated using MD for total wetting ethanol. Upon deposition, the ethanol nanodroplet continuously spreads and eventually forms an adsorbed monolayer, indicating total wetting. This aligns with the positive spreading coefficient calculated from MD-derived interfacial tensions. Two spreading regimes are identified based on the time evolution of the wetted area: an inertia-dominated initial spreading regime with a unit slope, and a second regime with a significantly larger slope due to the inclusion of the precursor film in the wetted area, deviating from Tanner's law exponent.

Compared to partial wetting liquids like water, the imbibition characteristics of total wetting liquids like ethanol are distinct. In small channels ($N = 2 \sim 4$), distinguishing the precursor film from the main capillary flow of ethanol is challenging. However, in larger channels ($N \geq 5$), the precursor film is clearly observed, leading to a zero dynamic contact angle and a meniscus curvature diameter smaller than the nanoslit width. Both the precursor film thickness and the meniscus curvature radius increase with channel width. The time dependence of the main capillary flow penetration length follows $l^2 = \alpha t$, similar to Washburn's equation, but with a decreasing imbibition rate ($\alpha$) as channel width increases, contrary to Washburn's prediction. The precursor film advancement is described by $l_p^2 = \beta t$ with $\beta > \alpha$, and its advancement rate ($\beta$) is largely independent of channel width. Notably, for small channel widths ($N \leq 3$), the overlap of precursor films on the two walls results in a surprisingly rapid imbibition behavior.

In the fourth part, our study extensively explores the wetting behavior and imbibition

doi:10.6342/NTU202404382

dynamics of isopropyl alcohol (IPA) and dimethylformamide (DMF) in graphene-based nanochannels through molecular dynamics simulations. Based on their spontaneous spreading and positive spreading coefficient, we identify IPA and DMF as total wetting liquids on graphene surfaces. The spreading dynamics follow two power laws ($A_b \sim t^n$): from a regime with $n = 0.5$, indicating a transition from inertia- to viscosity-control, to a regime with $n = 0.2$, characteristic of Tanner's law.

Our findings show that imbibition in nanoslits deviates from Washburn's equation, with the imbibition rate decreasing as channel width increases. For smaller channel widths, the penetration length remains proportional to time, consistent with Washburn's expression. Larger channel widths exhibit two distinct imbibition stages with a specific crossover time, independent of channel width. Both imbibition rates decrease as channel width increases, with the rate after the crossover time consistently greater than before. This unique behavior is reflected in the time evolution of internal energy. Additionally, the precursor film associated with total wetting liquids advances faster than the meniscus and re-thickens, reducing curvature radius and increasing Laplace pressure, accelerating imbibition in the second stage. These insights into total wetting liquid dynamics in nanochannels have implications for nanofluidic devices and membrane design optimization.

doi:10.6342/NTU202404382